8-23-2024 10:00 AM

Prostate Tissue Motion Tracking and Ultrasound Elastography Using Tissue Mechanics Derived Constraints

Tristan S. Curry,

Supervisor: Samani, Abbas, *The University of Western Ontario*
A thesis submitted in partial fulfillment of the requirements for the Master of Engineering Science degree in Electrical and Computer Engineering

Recommended Citation

Curry, Tristan S., "Prostate Tissue Motion Tracking and Ultrasound Elastography Using Tissue Mechanics Derived Constraints" (2024). *Electronic Thesis and Dissertation Repository*. 10413.
https://ir.lib.uwo.ca/etd/10413

Abstract

Current prostate cancer detection methods can be costly to obtain, such as magnetic resonance imaging, or lack necessary sensitivity or specificity, such as a digital rectal exam. Ultrasound elastography, a method that can be developed to output stiffness images that are reconstructed using displacement data estimated through ultrasound radio frequency readings, offering a potential solution to these challenges. Towards developing an effective prostate ultrasound elastography method, an algorithm utilizing dynamic programming and analytic minimization estimates the radial and angular displacements from a pre- and post-compression data set to determine the required material properties. This estimate of displacements is then refined through an algorithm where incompressibility, Laplacian smoothing, and strain compatibility are enforced. The refined displacement field was used to generate a strain image of the prostate. Material properties such as Young's modulus, Poisson's ratio, and shear modulus were then iteratively reconstructed using finite element analysis based algorithm to enhance the diagnostic value of output images. The material property calculation process, known for its accuracy, yields informative results to clinicians when diagnosing prostate malignancies.

Keywords

Prostate Cancer, Ultrasound Elastography, Tissue Mimicking Phantom, Finite Element Modelling, Oncology, Trans Rectal Ultrasound

Summary for Lay Audience

Detecting prostate cancer early is one of the best ways of ensuring an individual's survival, and current detection methods, such as an antigen test or MRI, may be non-conclusive or too costly to undergo. To avoid these issues, medical imaging techniques with an ultrasound system can be used to determine the material properties of human prostate tissue by collecting a pre- and post-compression image of the prostate. The initial estimate algorithm is responsible for collecting and analyzing data, while the second algorithm refines the estimates by enforcing material physics onto them. Enforcing these known properties in this process allows researchers to capture accurate and quantifiable stiffness measurements of the human prostate in real-time. This allows for rapid analysis of the prostate tissue for multiple regions of the prostate. Simulation and tissue-mimicking materials can be used as data sources to analyze the algorithms used to compute the stiffness and measure a ground truth. The simulated data can be obtained and modified using MATLAB software packages to fit the needs of the research goal and provide data sets that are both accurate and moderately realistic.

Tissue-mimicking material, created using gelatin and foam, provides a cheap alternative to human tissue. This material can be scanned with an ultrasound system to simulate real clinical cases, where the collected data may not be of good quality or contain image regions where artifacts exist. In addition, the calculated stiffness can be used to further enhance the imaging capabilities of ultrasound data by additional algorithm processes, allowing for additional information to be learned from the output images. Overall, this thesis outlines the steps taken to develop, quantify, and evaluate the effectiveness of three different algorithms in processing ultrasound data to quantify the material properties better. This will provide clinicians with a tool that is specific and easily accessible when screening for prostate cancer, offering a promising avenue for future research and application.

Co - Authorship Statement

The major contributors are Tristan Curry and Dr. Abbas Samani where Tristan Curry was the first author who wrote the initial draft of the manuscript and developed code. Dr. Samani was responsible for conceiving ideas and consultation for algorithms development, supervision, and editing the manuscripts. Matthew Caius is also a developer of some of the code used to generate results seen in Chapter 4.

Acknowledgements

I would like to acknowledge my supervisor, Dr. Abbas Samani for his guidance and advice throughout the development and editing of this thesis, along with my advisory committee members, Dr. Aron Fenster, and Dr. Daniel Goldman for their invaluable advice and feedback. A special thanks to Dr. Hassan Rivaz and his research group for providing the source code for the collaborative effort on AM2D Polar and answering numerous questions. Moreover, I would like to thank Dr. Niusha Kheirkhah and Matthew Caius as my work expands on their dissertations. Finally, I would like to thank my lab members for their feedback and the numerous individuals who provided invaluable support throughout my masters.

Table of Contents

List of Tables

List of Figures

List of Appendices

List of Mathematic Symbols

E – Young's Modulus

G – Shear Modulus

ν – Poisson's ratio of incompressibility

σ – Stress

ε – Strain

k – compressibility factor for Boussinesq equations

α, β – Regularization parameters

r – radial direction displacement data

θ – angular direction displacement data

U – Displacement (General)

List of Abbreviations

FEA – Finite Element Analysis

FEM – Finite Element Model

TRUS – Transrectal Ultrasound

USE – Ultrasound Elastography

MSE – Mean Square Error

CC – Cross Correlation

SNR – Signal to Noise Ratio

CNR – Contrast to Noise Ratio

RF – Radio Frequency

MLA – Multi-Line Acquisition

MLT – Multi-Line Transmission

TMP – Tissue Mimicking Phantom

Chapter 1

1 Introduction

Prostate cancer is a prevalent and devastating disease that affects a large portion of the population. Current detection methods, including imaging, tissue sampling, and blood measurements, are both advantageous and flawed. Increasing the accuracy of minimally invasive detection methods may increase the rate of early detection, one of leading contributors to beating malignancy. Tissue mechanics of prostate cancer lend Ultrasound (US) elastography being a viable and leading candidate for detection. An accurate reconstruction of the prostate and its stiffness is developed by leveraging image processing and refinement through imposing tissue mechanics. Studies on *in silico* data and phantom studies are used to validate proposed algorithms, as the data can both be validated and tested against known ground truths.

1.1 Prostate Cancer and Detection Methods

The Canadian Cancer Society estimates the occurrence of prostate cancer among Canadian men in 2024 to be 27,900, accounting for 22% of new cancer cases and 5,000 fatalities, approximately 11% of all cancer-related deaths in men for the year [1]. The prostate has three distinct zones that comprise its tissue anatomy, with two zones, the peripheral and transition zones, making up 95% of all cancer cases and the Peripheral zone making up 70% of all cases [2].

The Mayo Clinic reports that several factors increase the risk of developing prostate cancer, including advanced age, obesity, and having a family history of prostate cancer. While most prostate cancers are slow-growing and do not metastasize quickly, some forms of prostate cancer will develop and spread rapidly to nearby organs such as the bladder or colon. Additionally, prostate cancer can cause incontinence and erectile dysfunction. Early cancer detection dramatically increases men's chance of survival [3]. Currently, several methods are available to clinicians to detect abnormal growths within the prostate tissue. One of the most common methods employed to screen individuals for prostate tumors is the Digital Rectal Exam (DRE). During the DRE exam, a healthcare provider inserts a lubricated, gloved finger into the patient's rectum to feel abnormalities or changes in the tissues in that area. The DRE is low-cost and relatively fast, taking only minutes to complete [4]. However, the DRE suffers from specificity and often leads to false negatives [5].

To combat the lack of specificity related to the DRE, a second test is often conducted, a prostate-specific antigen (PSA) test. Blood is taken and analyzed to determine the quantity of PSA. An average value of PSA is 4.0 nanograms of PSA per milliliter of blood or lower, and levels above this threshold may be indicative of prostate issues, such as cancer or abnormal masses [6]. However, a PSA test is not definitive proof of cancer being present in the prostate. Blood PSA levels and prostate gland size increase with age [5]. Vigorous exercise, such as biking, can lead to elevated PSA levels and conversely, taking medication for benign prostate hyperplasia can result in lowered PSA [5].

If the DRE and PSA tests conclude that there is an enlarged region of the prostate or that the PSA levels are higher than average, a biopsy is scheduled to confirm the presence of cancerous tissue in the body. A guided needle is inserted into the prostate either through the wall of the rectum or through an incision made in the perineum [7]. A biopsy is a definitive way of determining if the abnormal mass detected is cancerous and cells can be analyzed directly after collection. This method is invasive, can result in bleeding at the collection site and, in rare cases, infection [7].

In contrast to PSA and biopsy, less invasive detection methods are available. Such methods focus on imaging the tissue in high quality and can allow for quick, non-invasive diagnosis of any present abnormalities. Magnetic Resonance Imaging (MRI) techniques offer a high-resolution, volumetric image. MRI imaging uses powerful magnetic fields to align protons in the body. Radio Frequency (RF) signals pull Protons out of an equilibrium state when passed through the body. The speed of realignment with the magnetic field is detected when the RF signal is turned off. The time and speed of realignment shows differences in tissues including healthy and cancerous tissues. MRI is considered safe and effective in imaging the human body, but the imaging modality is time-consuming, taking up to 1 hour for a single prostate scan [8]. Additionally, the use of potent magnets, disallows the use of MRI for patients with metal implants, pacemakers, or other medical devices containing magnetic components as such use would harm the implants, patient, and MR device [9].

Finally, ultrasound systems can diagnose prostate cancer using a Trans Rectal Ultrasound (TRUS) scan. The TRUS probe emits a pressure wave into the tissue at high frequencies. The signal travels through tissue and reflects to the transducer when the tissue medium changes. This reflection is measured and processed to create an image of the tissue. Combining the raw information from the ultrasound system, tissue mechanics, and image processing, the received data is transformed into accurate tissue property images which can be used to localize cancer within the tissue. Ultrasound has a rapid acquisition time, allowing for real-time imaging; and dramatically improves viewing tissues or organs that change rapidly or repeatedly. TRUS scans are about as invasive as the DRE and are much faster than an MRI scan time. [10].

1.2 Elastography

The fundamentals of Elastography consist of measuring deformation, which is induced by mechanical stimuli, within the tissue to quantify the change in stiffness that may be present in the tissue. The stiffening of tissue is often the result of malignancies or the presence of cancerous cells. A distortion must be made to the tissue, such as pressing the tissue with a transducer or external object, using acoustic radiation force, or using internal changes, such as arteries expanding due to blood pressure, to quantify the stiffness of the tissue [11]. Governing equations of materials can be applied to determine the tissue's strains, stresses, or displacements. Hooke's law, shown in Equation 1.1, requires that the strain and stresses in the tissue be known to calculate the stiffness of the tissue effectively. Hooke's law assumes that the material is under linear elastic loading and does not exceed the yielding point. Using Hooke's law to directly calculate the stiffness in the tissue would be advantageous, however, determining the stresses in a live tissue sample is not currently possible [12].

$$\sigma = E\varepsilon \tag{1.1}$$

where σ and ε are the stress and strain while E is the tissue Young's modulus. Several iterative-based methods can be used to estimate Young's modulus. One method involves using calculated displacements, strains, and an initial guess of Young's modulus to converge to a solution that satisfies the known strains in the tissue [13] [14].

Shear Wave Elastography (SWE) is a method of elastography in which an initial image of the tissue is taken. Then, a high-intensity shear wave is transmitted through the tissue and tracked by lower-intensity waves. The velocity of the shear wave can be directly related to the material stiffness of the tissue [15]. Figure 1 shows a graphic of how the shear wave can be used to track the stiffness of the tissue it is propagated in.

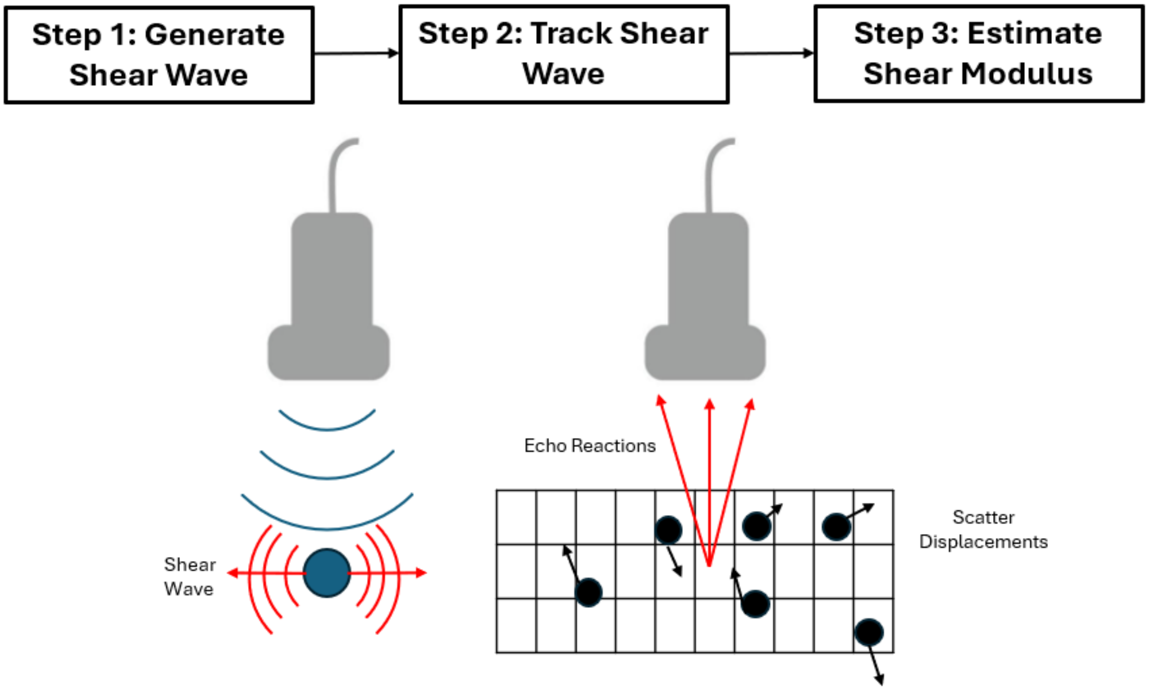

Figure 1: SWE wave tracking schema showing the propigation of the shear wave and the displacement tracking. The Shear modulus is then calculated according to the calculated speed of the shear wave.

The Shear wave is generated using acoustic radiation forces generated within the tissue. The tissue is then displaced, and the echo reactions are measured. Using the displacements, the shear modulus (G) of the tissue, using the tissue density, ρ, and shear wave speed (C_s) in the tissue, as seen in Equation 1.2 [16].

$$G = \rho C_s^2 \tag{1.2}$$

SWE has distinct advantages in imaging organ tissue, such as being highly repeatable, directly assessing the tissue's elastic properties, and collecting data without compressing the tissue [15]. However, several issues exist with using SWE in diagnostic scans. Image artifacts can lead to over or under-estimating tissue stiffness. Shear waves produced are also susceptible to waves generated within the body by pulsating vessels near the imaged tissue. If calculated using linear assumptions, tissue stiffness non-linearity can lead to erroneous results. And finally, the patient moving during the data collection can produce motion artifacts [17].

Unlike SWE, Quasi-Static Elastography offers a unique approach. It involves a meticulous manual deformation of the tissue or organ, either by the transducer or an external object, capturing a pre-compression and post-compression image. These images are then meticulously processed to determine the tissue's displacements, strains, and stiffness. This method, despite requiring additional processing of the image data, allows for the precise determination of displacements in two- and three-dimensional directions [18]. However, a limitation of quasi-static elastography is its ability to detect abnormalities only in the vicinity where the deformation is introduced [12]. Yet, for most cases, this limitation is not a concern, as cancers primarily occur in the Peripheral Zone. The Peripheral Zone is the volume of prostate tissue close to the contact point between the US transducer and the prostate allowing for minimal amounts of tissue to be between the prostate and transducer, allowing for reduced depth in scan being used which creates US images that are high resolution in comparison to US images generated using deeper scans. Another item hindering the use of Quasi-Static Elastography, are challenges in calculating the results, as the tissue's boundary conditions must be known to solve for the stresses or strains in the tissue [18].

To overcome the challenge of unknown boundary conditions, the known properties of materials while undergoing deformation are utilized. The Boussinesq equation, allows for the assumption that the displacement and stresses tend towards zero in a semi-infinite medium under a point load [19]. This assumption holds true when the material is semi-infinite, homogeneous, and isotropic, the stress-strain relationship is linear, and a point load is applied. Applying this theory to tissue mechanics and considering the indentation of the tissue as a point load, if the displacement at the contact point is small enough, the organ and tissue can be considered semi-infinite. As the displacement and strains will be small, the stress-strain relationship of the tissue remains linear. As shown in Figure 2, the point load P is applied to the semi-infinite medium, causing displacement and stress. The vertical stress at point O can be estimated using Equation 1.3, and as the value of r approaches the fixed points, the vertical stress tends towards 0.

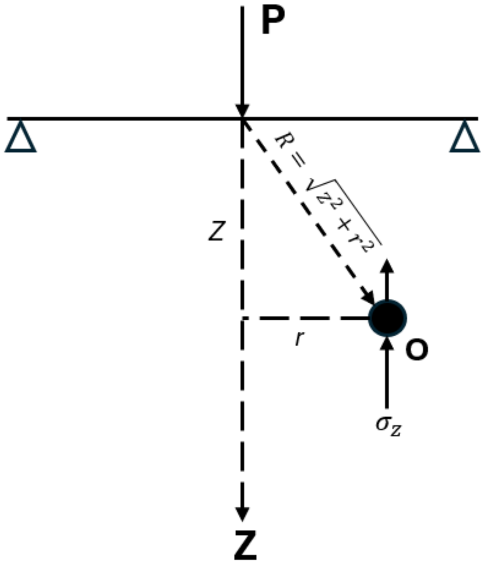

Figure 2: Measuring vertical stress using Boussinesq assumption where the semi-infinite hemi-sphere is indented and the resulting stress calculated based on the location of the point of interest. This result can be used to enforce boundary conditions for the system.

This equation can be utilized to estimate the out-of-plane strain which is often assumed to be negligible to simplify the tissue volume into a 2D model. With the vertical stress being calculated by Equation 1.3,

$$\sigma_z = \frac{3P}{2\pi z^2} \frac{1}{[1 + (r/z)^2]^{\frac{5}{2}}} \tag{1.3}$$

where P is the pressure, z, is the vertical distance away from the pressure, r is the hypotenuse distance, and σ_z the vertical direction stress. The boundary conditions can now be enforced on the calculations, Quasi-Static Elastography is a viable, and powerful tool that can be used to calculate stiffness in data collected from prostate tissue.

Another important aspect of elastography is the concept of strain compatibility, which states that when a material is subject to a single continuous displacement, there exist conditions which guarantee the field to be continuous [20]. In addition, there exists a relationship between strains in perpendicular directions, and can be related through Equation 1.4, the 2D compatibility equation,

$$\frac{\partial^2 \varepsilon_{xx}}{\partial y^2} + \frac{\partial^2 \varepsilon_{yy}}{\partial \mathrm{x}^2} = 2\frac{\partial^2 \varepsilon_{xy}}{\partial \mathrm{x}\,\partial \mathrm{y}} \tag{1.4}$$

where ε_{xx} is the strain in the *x* direction, ε_{yy} is the strain in the *y* direction, and ε_{xy} is the shear strain. This equation enforces that the sum of the second partial derivative of the strains must be equal to twice the shear strains partial derivative, which can be geometrically interpreted with Figure 3.

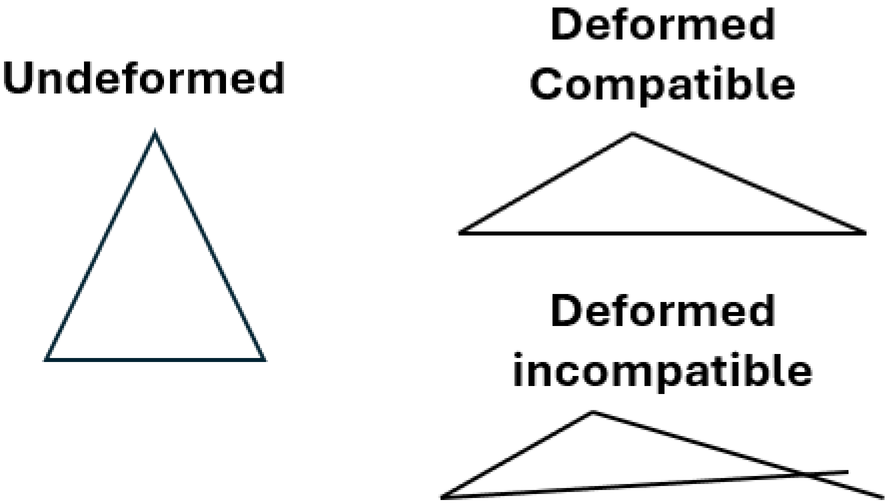

Figure 3: Illustration of how compatibility is enforced through material properties. The Left most image shows the original undeformed image. The upper right shows a compatible deformation where the loading results in a continuous deformation. The bottom right shows a deformation that is not compatible and results in a non-continuous deformation.

Figure 3 shows an undeformed triangle on the left and two possibilities after being deformed on the right. If it is assumed that the material does not experience a force resulting in any plastic deformation, then there should be no change in the connections between the vertices. The deformation maintains all initially connected points, making the top deformed image compatible. In contrast, the incompatible deformation shows that a self-intersection has occurred and would no longer satisfy the compatibility equation. This compatibility can be extended to human prostate tissues as a TRUS probe deforms them. The measured displacements and strains should adhere to the compatibility equation and, when enforced on the collected data, can be used to calculate a refined strain field and better stiffness calculation of the internal tissues.

Finally, it is essential to understand the characterize the ability of tissue to change volume while undergoing deformation. This is defined by the material compressibility property which is characterized by the Poisson's ratio (υ). Under 1D loading, it is defined using Equation 1.5,

$$\nu = -\frac{\varepsilon_{trans}}{\varepsilon_{axial}} \tag{1.5}$$

where ε_{trans} is the transverse strain, and ε_{axial} is the axial strain when a material is stretched or compressed along only one axis. The range of values for Poisson's ratio for most materials are between 0.0 and 0.50, where 0.0 is perfectly compressible, while 0.5 represents a completely incompressible material. As most organs are composed of water, they tend to have values of ν close to 0.50, the Poisson's ratio of water [21]. Additionally, Poisson's Ratio, ν, can be calculated for compressibility in specific directions in 2D, Equations 1.6 and 1.7, which are obtained from the 2D Hooke's law, are used to calculate the value of ν along each axis using the stresses, σ, strains, ε, and Stiffness, E.

$$\nu_x = \frac{\sigma_y - \varepsilon_y * E}{\sigma_x} \tag{1.6}$$

$$\nu_y = \frac{\sigma_x - \varepsilon_x * E}{y} \tag{1.7}$$

Both equations 1.6 and 1.7 require the material's Young's Modulus, internal stresses, and strains to be known to calculate the Poisson's Ratio. As we assume that the tissue is isotropic υ_x and υ_y, the average value can be considered as a more accurate estimate. To calculate the stresses and Young's Modulus for prostate tissue, a Finite Element Analysis (FEA) must be conducted to converge to an acceptable solution for both the stress and stiffness of the material. The specifics of this iterative approach will be discussed in further detail in Chapter 4.

1.3 Ultrasound Imaging

The first recorded use of US imaging was in 1956 by Ian Donald and Tom Brown, who used emerging technology to measure the diameter of a human fetus's head. Since then, many advancements in US technology have been developed, including real-time processing and visualization, strain mapping, and 3D ultrasound capabilities. These advancements have made diagnostic imaging in US a reliable and common practice in the medical field.

1.3.1 Governing Principles of Ultrasound Operation

Piezoelectric crystals generate ultrasound waves by expanding and contracting when an electric current is applied. These waves create a pressure wave in tissue samples, allowing the ultrasonic wave to propagate through the tissue [22]. These generated waves propagate through the tissues and can interact through reflection and attenuation.

Reflection, as the term suggests, is the process where a part of the propagating wave bounces back off tissue or bone. This can occur in two ways: specular reflection, when the wave reflects due to a large surface interaction; and scattering reflection, when the wave reflects due to smaller surface interactions [23]. While the transducer will receive some of the reflected pressure waves, the rest will transmit through the material. This interaction is significantly amplified when the tissue medium changes, such as a change in tissue type, for instance, transitioning from muscle to fat. The acoustic impedance, which is measured in Rayls, can be determined by Equation 1.8,

$$Z = \rho c = \sqrt{\rho / k} \tag{1.8}$$

where Z is the acoustic impedance, ρ is the density of the material, c is the speed of sound in the material, and *k* is the compressibility of the material. Additionally, the reflection and transmission of the wave can be characterized by the reflection and transmission coefficients, which can be obtained through Equations 1.9 and 1.10, respectively.

$$R = \frac{P_r}{P_i} = \frac{Z_2 - Z_1}{Z_2 + Z_1} \tag{1.9}$$

$$T = \frac{P_t}{P_i} = \frac{2Z_2}{Z_2 + Z_1} = 1 + R \tag{1.10}$$

where P_r is the reflected pressure wave, P_i is the incident wave pressure, P_t is the transmitted pressure wave, and Z_1, Z_2 represent the acoustic impedance in the first and second mediums. A selection of relevant biological materials and their acoustic impedance are provided in Table 1.

Table 1: Biological Materials and their Acoustic Impedance [23].

Material	Z[MRayl]
Air	0.0004
Fat	1.34
Water	1.48
Liver	1.65

The acoustic impedance of soft tissues ranges from 1.34 to 1.71, while bone in the skull has an impedance of 7.8. As US systems measure the reflected pressure waves, the measured reflections can show areas where tissue type changes within the body, and as the acoustic impedance is dependent on the tissue density and compressibility, the collected reflections are based in material properties.

In contrast to the reflection of the acoustic wave, attenuation is the reduction of the wave intensity as it travels through the tissue [23]. The intensity can be calculated using Equation 1.11 and transformed into a logarithmic scale to show the data in a linearly scaled grid using Equation 1.12.

$$I = P^2/(2\rho c) \tag{1.11}$$

$$I_{dB} = 10\log_{10}(I/I_{ref}) \tag{1.12}$$

The intensity, I, is dependent on the applied pressure P, the material density ρ and the speed of sound in the material c and has units mW/cm^2. The log transform requires a known reference intensity, I_{ref}, for the log transform basis. In practice this value is $10^{-12}W/m^2$, which is the threshold of human hearing [23]. As the wave propagates through a material, its intensity diminishes, a phenomenon that can be described as a materials attenuation coefficient, α. For soft tissues the attenuation coefficient is of the range 0.5 to 1 $dB/(cm \times MHz)$. With a material's attenuation coefficient, the intensity can be calculated for any given depth using Equation 1.13, or if using the log transformed intensity Equation 1.14.

$$I(r) = I_0 \exp\left(-\alpha f\, r/4.343\right) \tag{1.13}$$

$$I_{dB}(r) = -\alpha f r \tag{1.14}$$

The intensity of the acoustic wave is dependent on the initial wave intensity I_0, the frequency in MHz, f, and the depth the wave has traveled to in centimeters, r. The wave intensity can also be used to find the intensity of the reflected and transmitted waves in a similar way to the pressure wave reflection or transmission. Equation 1.15 can be used to calculate the reflection intensity, R_I, and Equation 1.16 can be used to calculate the transmitted intensity, T_I [23],

$$R_I = \frac{I_r}{I_i} = \frac{P_r^2/(2\rho_1 c_1)}{P_i^2/(2\rho_1 c_1)} = \left(\frac{P_r}{P_i}\right)^2 = \left(\frac{Z_2 - Z_1}{Z_2 + Z_1}\right)^2 \tag{1.15}$$

$$T_I = \frac{I_t}{I_i} = \frac{P_t^2/(2\rho_2 c_2)}{P_i^2/(2\rho_1 c_1)} = \frac{Z_1}{Z_2}\left(\frac{P_t}{P_i}\right)^2 = \frac{4Z_1 Z_2}{(Z_1 + Z_2)^2} = 1 - R_I \tag{1.16}$$

where, P is the pressure, ρ, the density of the medium of transmission, c is the speed of sound in the medium, and Z, the medium's acoustic impedance. From Equations 1.15 and 1.16, it can be demonstrated that the reflected and transmitted intensity can be calculated from the pressure, material density, and medium speed of sound, or through knowing the acoustic impedance of each material. As the signal travels deeper into the tissue, more of the returning wave intensity is lost. To overcome this issue a time gain compensation maybe applied to increase the signal intensity based on the elapsed travel time of the signal [23]. Combining information from both the wave reflection and intensity, it is possible to gain information about the tissue's material properties.

1.3.2 Beam Forming and Acquisition

Once the signal is received from the tissue reflections, it must be processed to maximize data quality. One such way of achieving this is by using envelope detection, which takes the original RF signal, rectifies the data, and applies a low-pass filter to smooth the data. This has the advantage of being low cost and creates an improved image. However, using this approach removes many data features that may be beneficial in determining tissue mechanics. It's worth noting that modern methods have moved beyond this technique, opting to transform the raw RF data into a usable form through advanced digital computational methods. These methods represent a significant advancement in medical imaging, providing a more comprehensive understanding of tissue mechanics. Another concept that enhances data generation is beamforming. This technique allows for several modifications to the way a US beam is generated, thereby improving the quality of the data. Each alteration made to the beam is designed to enhance one or more image metrics, as detailed in Table 2.

Table 2: Image Metrics for US Imaging and a Brief Description of Each

Image Metric	Description
Spatial Resolution	Smallest spatial difference two scatterers that can be distinguished.
Temporal Resolution	Time interval between two consecutive frames (Frame Rate).
Contrast	Capability to visually distinguish between 2 different objects.
Penetration Depth	Increase to depth while maintaining adequate SNR value.
Array Aperture	Physical size of the transducer plane.
Field of View	Size of area represented by the captured objects.

Altering how the device forms and calculates the US beam can impact each of these metrics. Some critical techniques for altering the beam are linear and phased array beam forming, multi-line acquisition (MLA) and multi-line transmission (MLT) beam forming, plane and diverging wave beam forming, and synthetic aperture beamforming [24].

Linear array beam forming utilizes a subset of the transducer elements for transmitting and receiving signals. The A-line signal is shifted across the image utilizing the entire array and different phased signals to focus the beam at a region or point in the material volume. This ability to focus allows the emission of higher-pressure and smaller beams. These attributes contribute to improved SNR, resolution, and penetration depth but impede the field of view as more beams are required to image a region, affecting the temporal resolution. Phased array imaging also generates images line by line but uses all elements simultaneously with varying phases to steer the beam in the desired direction [24]. One downside to this method is that increasing the pitch reduces the array aperture, leaving less room for elements on the transducer. Lastly, an apodization mask can be used with these two methods. Apodization allows for amplitude weighting of the average velocity across the transducer aperture. Apodization can lessen the impact of the low-intensity beams in the scan, known commonly as side lobes, and their associated artifacts [25].

Multi-line Acquisition is possible as it can be transmitted wide into the tissue. Several receiver elements can be used simultaneously creating a narrow reception beam and several scan lines. This method improves the frame rate by acquiring more simultaneous lines and requiring fewer transmit and receive actions than single scan line methods. Additionally, averaging consecutive images acquired during the higher frame rate improves the SNR and contrast. This method though reduces the lateral spatial resolution [24].

In the two previous methods, the transmission and reception alterations focused on increasing some imaging metrics while trading off for degradation in others. For in-plane and diverging wave beam forming, the primary focus is maximizing the frame rate which is necessary for imaging high-frequency changes in tissue displacement or strains, as in SWE. Plane and diverging wave beam forming seek to reduce the required transmission and reception events to the bare minimum to create an image of the tissue. The idea is to create a single homogeneous transmission event that the elements receive and process using different phase sets, producing multiple lines simultaneously. This approach cannot achieve lower SNR values and suffers from low penetration depth due to the generated decrease in overall pressure. Plane beam forming also has poor contrast and spatial resolution [24]. Methods exist to improve the SNR, contrast, spatial resolution, and penetration depth such as image compounding, which applies an angle to the beam, effectively steering it toward the desired region [26]. Improving the metrics degraded under the high temporal resolution will heavily impact the method's frame rate, thereby preventing the viewing of shear wave effects. The most considerable difference in methodology for plane and diverging wave beam forming lies in the beam's focus: where plane beam forming requires a focus; the diverging wave does not. Synthetic aperture beamforming utilizes one element excitation which is listened for by all remaining elements. The distance between transmitting and receptive elements creates a phase set. This method combines the received signals over the entire transmission array to create the image. These images suffer from penetration depth reduction and worsening SNR values. Using sub-aperture transmission can improve these metrics by segmenting the transducer into groups and utilizing them. However, this approach reduces spatial resolution because the method's effectiveness depends on receiving signals from all receiver elements and decreasing the array aperture decreases spatial resolution [27]. Figure 4 shows a visual representation of the different kinds of beamforming.

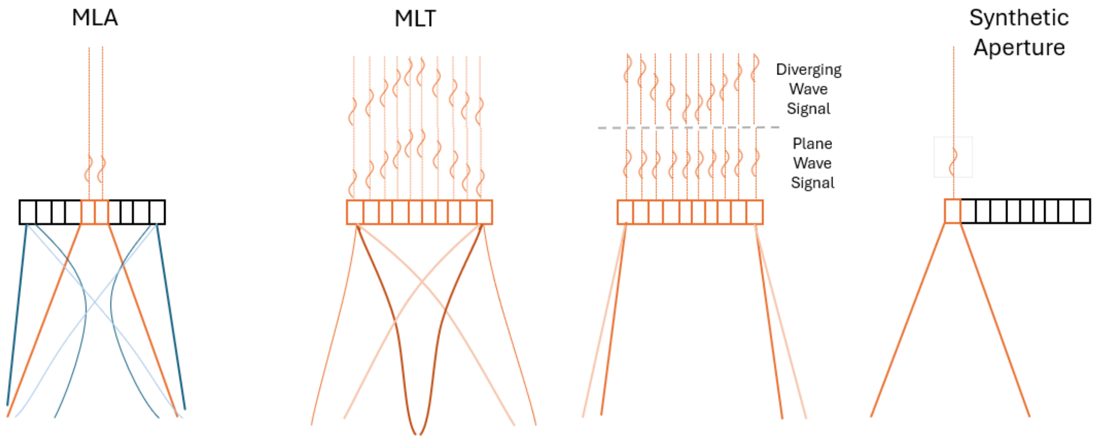

Figure 4: A Visual representation of the major beamforming techniques. The left most image shows the multi-line acquisition, and multi-line transmission. While the second from the right shows a plane wave or diverging wave beam forming. Finally, the right most image shows the synthetic aperture beamforming method.

1.4 Image Processing and Optimization

All US data collection requires some amount of post processing to transform the raw radio frequency data into desirable forms such as strain maps or stiffness reconstructions. To accomplish this, image and data processing techniques are used to transform the data.

One method of data processing is dynamic programming which is the process of taking a complex problem or task and breaking the problem into simpler sub-problems [28]. This method of computation in tasks has several advantages when dealing with complex or large-scale solutions, that are common in image processing and data set calculations. Figure 5 shows an example of dynamic programming.

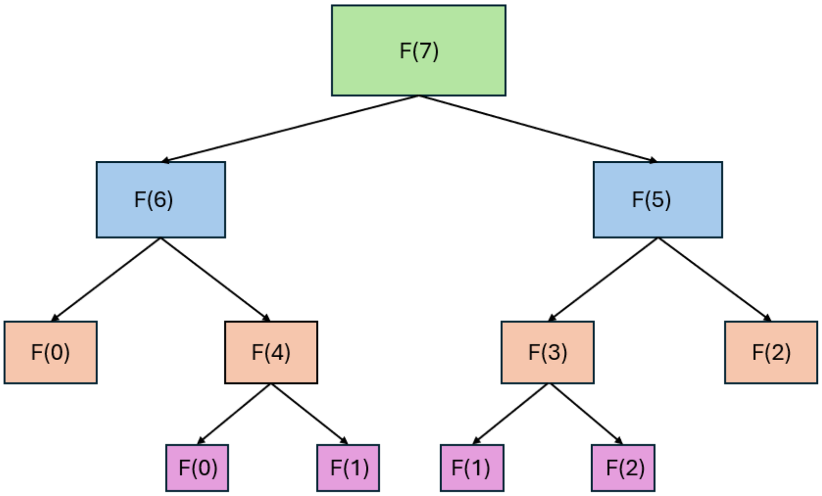

Figure 5:Dynamic Programming breaking a complex problem into sub problems. The smallest problems located at the bottom of the image are propagated upwards to solve the larger problems above. The DP approach stores previous solutions and can increase the speed of calculation by using the stored solution from the smaller problems.

In Figure 5, we solve the problem represented by the uppermost block labeled F (7), then create two smaller sub-problems, continuing this process until reaching the smallest possible sub-problems. In this case, F (0), F (1), and F (2) are the smallest possible sub-problems in the set and appear at the bottom of the image. When the smallest known problems are solved, the solution is propagated upwards in the algorithm to compute more significant unknown problems. In this example, F (5) and F (6) rely on more minor problems already solved. Instead of recomputing the answer for F (0) and F (2) to solve these problems, the known answer is propagated, thereby reducing the need for recalculations in previously solved problems [28].

Analytical minimization minimizes a known cost function to allow the system's solution to be known. Several optimization methods, such as gradient descent involve using an iterative algorithm to calculate the gradient over a dataset domain and determine the minimum value of a function [29]. This can be visualized in Figure 6.

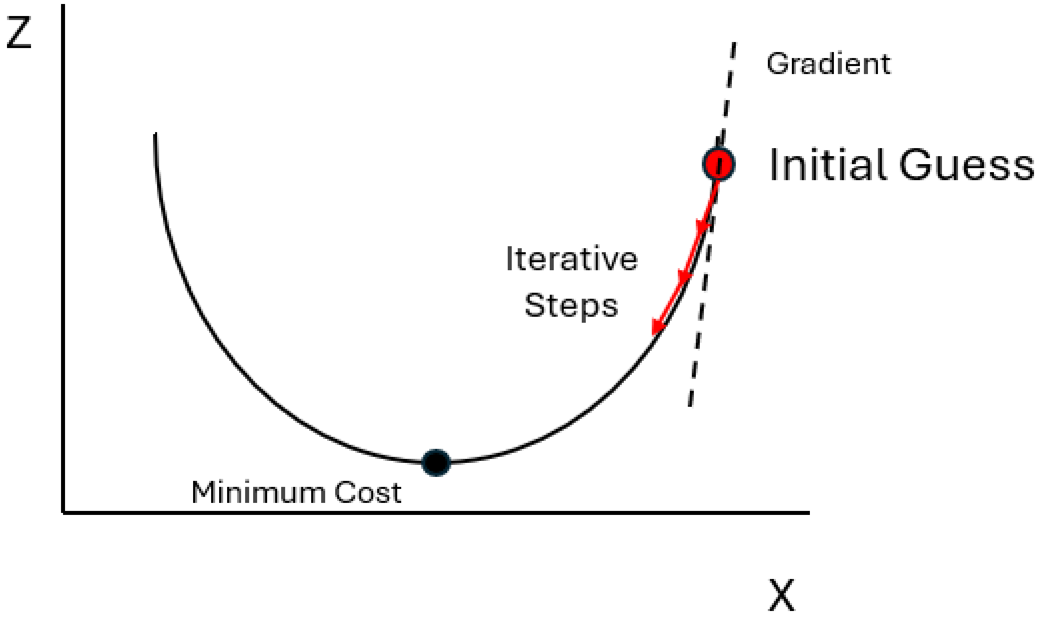

Figure 6: Gradient Descent Analytic Minimization on a parabolic function. The calculated gradient is used to update the next iteration of the cost function. This calculated change, the error and present value are used to determine if a minimum cost has been achieved.

In Figure 6 a known function is to be minimized using gradient descent minimization. This method requires an initial guess as to where the minimum might be found, the number of iterations to compute, and the size in step to take after each iteration. At each new iteration location, the gradient of the function is calculated to determine the change in cost, thus allowing the algorithm to determine if the current step direction is decreasing. This method, while simple to implement, suffers from the vanishing gradient problem, which can be overcome using an adaptive optimizer to help prevent the algorithm from using small or non-existent gradient values.

Additionally, computations in image processing can be efficiently performed using convolution. Convolution is a mathematical function that takes as an input, two functions and computes a third function which is based in the values of the two original functions and can be defined by Equation 1.17,

$$f * g = \int_{-\infty}^{\infty} f(\tau) g(t - \tau) d\tau \tag{1.17}$$

where f , the input function and g, the weighting function being convolved, and t is the shifting amount and is not necessarily a time domain shift [30]. This can be extended into the image processing realm using discrete convolution using Equation 1.18,

$$(f * g)[i,j] = \sum_{k=0}^{m}\sum_{l=0}^{n} f[i-k,j-l]g[k,l] \tag{1.18}$$

where the image is m x n data points. In this case the weighting function in is commonly referred to as the convolution kernel or filter. Kernels are specially designed matrices that weigh the base function in such a way to impose a required output. For instance, a blur filter may be used on a dataset to help smooth an image an example of this can be seen in Figure 7.

Figure 7: An example of image convolution, where the input image was smoothed used a convolutional filter. The gaussian blur filter is used implemented as a 3x3 matrix of values. During the numerical convolution this results in the right blurred image.

Finally, it is important to talk about known metrics used to judge the similarities between two images. As when developing algorithms for ultrasound elastography (USE) ground truth images are often used to judge the accuracy of the output from the algorithm [31]. Common metrics are the mean square error (MSE) and image correlation. MSE between images compares pixel values of two images, to determine how different they are, thus producing a metric that compares a computed value to a known true value as can be seen in Equation 1.19 [32],

$$MSE = \frac{1}{n}\sum_{i=1}^{n}\left(Y_i - \hat{Y}_i\right)^2 \tag{1.19}$$

where n, is the total number of points, Y_i is the true value and $\hat{Y}_i$ is the predicted value. This metric is useful when a true value for a data set is known, and a predictive algorithm has been used to estimate the values.

In addition to the MSE, image correlation, also known as discrete cross correlation, can be used to determine if two images are similar, even if the images are rotated, translated or warped. This is especially useful for USE datasets as often captured image datasets are not perfectly in line with known ground truths [33]. Image correlation was developed initially to compute the correlation score using Equation 1.20,

$$r_{i,j} = \frac{\sum_m \sum_n \left[f(m+i, n+j) - \bar{f}\right]\left[g(m,n) - \bar{g}\right]}{\sqrt{\sum_m \sum_n [f(m,n) - \bar{f}]^2 \sum_m \sum_n [g(m,n) - \bar{g}]^2}} \tag{1.20}$$

where $f(m,n)$ is the pixel intensity at the point (m,n) in the original image, and $g(m,n)$ is the gray scale value at a point in the translated image where $\bar{f}, \bar{g}$ are the mean pixel intensity values. This method can also be implemented more quickly using Fourier Transform and matrix multiplication [34].

To calculate image correlation effectively, the two images must first be registered to one another. This means that it must be determined if the two images being compared have been warped and/or translated, taken from different viewpoints, or if two different sensors have been used to capture the image. To determine this, automatic image registration algorithms can be used. These algorithms iteratively alter one image in a set of two, to determine the applied transformations to the image. Several transformation options are available, but typically the rotation, translation, and warping of an image are considered [35]. With image correlation and MSE it is possible to use *In Silico* data to generate results in USE algorithm development and verification.

To determine the clarity of the signal, the signal to noise ratio (SNR) and contrast to noise ratio (CNR) provide valuable information on the ratio between the desired signal and the noise power. The SNR value is the measure of the signal's intensity with that of background noise. The higher the value, the clearer the signal [36]. The SNR can be calculated with Equation 1.21,

$$SNR = \frac{\bar{S}}{\sigma} \tag{1.21}$$

where $\bar{S}$ is the spatial signal average, and σ is the standard deviation in the noise level [36]. While the CNR can be calculated using Equation 1.22, where S_A and S_B are the signal intensities for the producing structures, and σ_0 is the standard deviation of the image noise [37]. The SNR and CNR both provide a measure of clarity on the image and how easily distinguishable it is to background noise. The CNR is useful when there is a bias in an image, such as when features of the image are easily distinguishable but may appear to be washed out due to noise [37].

$$CNR = \frac{|S_A - S_B|}{\sigma_0} \tag{1.22}$$

1.5 Current USE Techniques and Algorithms

Examining the most significant USE techniques and their efficacy in identifying abnormalities in organ tissues allows for a view of the current implementations and the strengths that USE has when detecting tissue abnormalities. A study by G. Saloman *et al.* demonstrates that USE could ascertain the presence of an abnormality in the tissue. The researchers utilized a Hitachi Medical EUB-6500HV US system with a V53W end-fired transrectal probe. The data set comprised of 109 patients with confirmed prostate carcinoma from a single institution, after the data was collected and analyzed with the elastography function of the US system. The study revealed that the sensitivity and specificity of the method are 75.4% and 76.7% respectively for the 451 image cases. One of the drawbacks of the current method is that it depends on the Strain Index given by the Hitachi system which cause false positives for cases of Benign Prostate Hyperplasia as this condition increases the value of the Strain Index for the Hitachi system. The study also concludes that the image quality is crucial for the system's accuracy in calculating the strain found in the prostate tissue [38].

Several algorithms can estimate the tissue displacement and strains based on obtained RF data sets. H. Rivaz has proposed a software approach to calculating the displacements in tissue based on Dynamic Programming and 2D Analytic Minimization, called AM2D [39] [40]. The proposed method involves collecting two RF data sets for the algorithm, one pre-compression, and one post-compression. The algorithm tracks pixel displacements and calculates the strain from the proposed displacements using an iterative minimization technique for each line in the image. This algorithm was used on a data set produced *In Silico*, using Field-ii and Abaqus to simulate the RF data and displacements expected to occur due to a displacement from a TRUS probe contact with the prostate tissue. The results from this simulated study show that the CNR used to evaluate the strain displacements is 14.3 in the axial direction and 1.13 in the lateral. After confirming the algorithm's viability through the simulated study, researchers conducted a clinical study on seven patients with liver cancer. This study generated displacement and strain maps for each patient using the proposed AM2D method. These studies showed the stiffened tissue present in the liver for each patient. They reported that the axial displacement and further refinement of the strains using a Kalman filter clearly showed the ablation in the liver. In contrast, the lateral strain calculated from the displacement field had no advantage in image clarity, thus making it a currently under-utilized tool for detecting malignancy [39] [40].

Building on the AM2D method, Rivaz proposed a further enhancement to estimate tissue displacements using a Global Time Delay Estimation (GLUE) algorithm [41]. This method incorporates the analytic minimization technique used in AM2D, with the addition of GLUE algorithm computations, with significant improvement. To estimate the time delay between frames, a displacement continuity enforcement and the amplitude similarity term are included in a non-linear cost function. A key distinction is that GLUE's cost function is applied to the entire image, not just a single scan line. The algorithm was tested against three data sets, including a simulated data set, a phantom study, and clinical data. The simulated and phantom study data were evaluated using the SNR and CNR values, summarized in Table 3. Just as in the AM2D paper, ground truth data was generated using a FEA tool to determine the realistic displacements and strains in the tissue material. The phantom study was conducted using a CIRS elastography phantom with the RF data being captured on an Antares Siemens system with a VF10-5 linear array.

Table 3: Summarized results from data sets used to evaluate the GLUE algorithm [41]

	SNR		**CNR**	
Simulated 1	Axial	Lateral	Axial	Lateral
NCC	2.14	0.52	4.94	7.69
AM2D	5.29	4.50	14.62	10.87
GLUE	44.63	4.61	26.31	11.03
Simulated 2				
NCC	Fails	Fails	Fails	Fails
AM2D	Fails	Fails	Fails	Fails
GLUE	43.70	4.41	17.45	6.72
Phantom				
NCC	2.20	3.60	1.07	0.39
AM2D	26.21	4.77	16.01	3.25
GLUE	29.85	7.22	18.21	4.09

The results from the first simulated data set show that GLUE profoundly enhances the SNR and CNR for the axial direction when compared to the NCC and AM2D values. The improvement in the lateral direction is minor when comparing the AM2D SNR and CNR values to those of the GLUE outputs. This same trend can be seen in the phantom study when comparing AM2D to GLUE. The second study enforced a slipping condition between the imaged organ and the background material. This may occur in some instances, such as between the prostate and the rectal wall [42]. The failure metric is utilized when the SNR and CNR values cannot be calculated because the NCC and AM2D methods do not provide sufficient information. However, GLUE can calculate the SNR and CNR values even with large-scale discontinuities. Four patients underwent US scans for primary or secondary liver cancers for a clinical study. Ablation negatively impacted the data quality by introducing high-temperature gradients, microbubbles, and pulsations from the hepatic vessel, which disturbed the displacements. These results show that GLUE can generate results that can help clinicians visualize an accurate representation of the tissue and any abnormalities that may be present in the patient, even under poor conditions such as post-ablation or when large out-of-plane displacement occurs. However, while GLUE can produce strong results in the axial direction, higher quality lateral results are required. This demonstrates that despite significant improvements in displacement estimation under non-ideal conditions, high-quality lateral displacements are still necessary.

Researchers propose a tissue mechanics-based method to improve the quality of the lateral results. Created by Kheirkhah *et al.* [43], this method seeks to improve the lateral displacement and strain calculation through the enforcement of tissue mechanics onto the initial estimates of the displacements and strains found from GLUE. The method seeks to regularize the displacements using tissue incompressibility with the 3D Boussinesq model, deformation compatibility using the compatibility differential equation and finally refine the strains produced from this algorithm, known as STREAL [43]. Using the Second Order Ultrasound Elastography (SOUL) and GLUE methods as initial estimations for the displacement field, STREAL processes the initial displacements using a second-order derivative-based regularization approach, where the 2D Laplacian of the displacement components is minimized [43]. The advantage of using the Laplacian over other regularization methods is its low cost in computation time and its high effectiveness in tissue tracking applications [44]. Afterwards, tissue incompressibility is enforced by setting the divergence of the displacement field in a 3-dimensional space to zero. Additionally, the out-of-plane is estimated using the Boussinesq equation rather than assuming plane strain or plane stress, as other displacement algorithms assume. Finally, strain compatibility is enforced on the data using Equation 1.22,

$$\frac{\partial^2 \varepsilon_{xx}}{\partial y^2} + \frac{\partial^2 \varepsilon_{yy}}{\partial x^2} - 2\frac{\partial^2 \varepsilon_{xy}}{\partial x \partial y} = 0 \tag{1.22}$$

where ε_{xx} and ε_{yy} are the lateral and axial strain respectively, and ε_{xy} is the shear strain. A numerical approximation was derived using the finite difference method to implement this equation for image processing. To determine the algorithm's effectiveness, an *In Silico* breast phantom was created with segmentation with 3D Slicer and 3D US images of a typical breast geometry. A finite element mesh was created from this geometry using IA-FEMESH software, enabling the addition of a spherical inclusion to the model. Finally, Abaqus, a FEA software, was utilized to apply loading to the mesh to mimic contact with a transducer. Gaussian noise was added as another step to add realism to the collected displacement data from the FEA. After collecting the data, SOUL and GLUE were used to generate an initial estimate of the displacements before applying the STREAL algorithm. By using the NCC as a similarity metric, the output displacement field is compared to the with the noise-free ground truth, summarized in Table 4.

Table 4: Summarized NCC values for In Silico data from the GLUE Displacement estimation algorithm [43].

NCC Measure against ground Truth		
Axial Displacement	Noisy	0.93
	Refined 1	0.99
	Refined 2	1.00
Lateral Displacement	Noisy	0.87
	Refined 1	0.96
	Refined 2	0.99
Axial Strain	Noisy	0.076
	Refined 1	0.59
	Refined 2	0.59
	Refined 3	0.69
Lateral Strain	Noisy	0.016
	Refined 1	-0.13
	Refined 2	0.20
	Refined 3	0.22

The NCC value can be improved through refinement imposed by the STREAL algorithm, and the lateral direction displacement and strain NCC values can be significantly enhanced through this refinement. A tissue-mimicking phantom study was conducted to validate the algorithm further, and the Breast Elastography Phantom Model 059 from CIRS was utilized. This phantom mimic’s human breast tissue and contains several inclusions ranging in size; all data collected from the phantom was analyzed using SNR and CNR values. Additionally, the phantoms were simulated using the Abaqus FE solver, and quasi-static stimulations were applied in the FEA solver. The SNR and CNR results from the phantom case and the NCC result from the ground truth simulation can be seen organized in Table 5 and Table 6. For the SNR and CNR values generated from GLUE, SOUL, and STREAL, a consistent improvement is made when STREAL is used to refine any displacement estimates made for both the axial and lateral directions, with significant improvements being observed in the lateral direction when comparing the STREAL results to GLUE. It is also evident from Table 6 that the NCC value between the output data from GLUE and SOUL is consistently lower than STREAL, especially when looking at the results in the lateral direction displacements. A considerable improvement is seen for the lateral direction, which shows that it is possible to improve the lateral direction results beyond what is capable in GLUE and SOUL by enforcing known tissue mechanics onto the collected datasets, such as the strain compatibility and the Boussinesq model.

Table 5: SNR and CNR values for STREAL phantom Study [43].

		SNR			**CNR**		
Phantom	Image	GLUE	SOUL	STREAL	GLUE	SOUL	STREAL
A	Axial Strain	8.7	15.9	18.8	5	5.2	10.4
	Lateral Strain	2.7	2.5	13.2	0.8	0.8	12.3
B	Axial Strain	3.9	4.2	7.1	1.1	1	2.1
	Lateral Strain	1.7	2.1	3.2	1.4	1.2	1.9
C	Axial Strain	9.1	8.9	9.1	4.5	3.2	4.6
	Lateral Strain	2.2	1.6	2.6	1	0.8	3.3
D	Axial Strain	8.5	9.3	11.6	3.6	2.4	3.6
	Lateral Strain	3.3	4.2	3.7	0.8	1.2	0.8

Table 6: NCC values for Phantom Study and In Silico ground Truths [43].

		NCC		
Phantom	Image	GLUE	SOUL	STREAL
A	Axial Displacements	0.99	0.99	0.99
	Lateral Displacements	0.59	0.36	0.88
B	Axial Displacements	0.92	0.92	0.92
	Lateral Displacements	0.43	0.51	0.79
C	Axial Displacements	0.88	0.83	0.88
	Lateral Displacements	0.49	0.37	0.66
D	Axial Displacements	0.95	0.89	0.96
	Lateral Displacements	0.49	0.41	0.52
Improvements	Axial Displacements	0.3 ± 0.5%	4 ± 3%	
	Lateral Displacements	44 ± 28%	73 ± 42%	

It is important to note that this study was conducted on breast tissue and inclusions and collected using a linear probe. While the enforced tissue mechanics still apply to prostate and prostate cancer the data type and formatting do not. Changes are required for the same study to be replicated on the prostate using a TRUS probe.

In addition to determining strain and displacement values using the earlier methods, researchers can reconstruct additional material properties using the known strains. For instance, Samani *et al.* proposed an FEA-driven algorithm to reconstruct the elastic modulus for breast tissue [45]. The method proposes treating tissue as a continuum undergoing static loading. This method also assumes that the strains applied as part of the elastography imaging are less than 0.05 to maintain linear elasticity. Using Equation 1.23, a stress-strain relationship can be used to determine the stiffness for each point in the tissue. A forward solution is determined by establishing displacements and calculating subsequent strains and stress using Equation 1.23,

$$\sigma_{i,j} = \frac{E}{1+\nu}\left(\varepsilon_{i,j} + \frac{\nu}{(1-2\nu)}\delta_{i,j}\varepsilon_{i,j}\right) \tag{1.23}$$

where, E is the Youngs modulus, ν is the Poisson's ratio, ε is the strain, and δ is the Kronecker delta**.** Given the inherent complexity of the 3D case, an analytical solution remains elusive. In this context, this paper introduces a novel approach proposing the use of Equation 1.23 to update the modulus through an iterative numerical process, a departure from the costly least-squares method advocated by other researchers [46]. This innovative method requires an initial image segmentation and modulus guess to compute the stiffness through the iterative FEA method. These initial estimates are then used to calculate the stress using the FEA solver. The measured strain is used to update the modulus along with the calculated stress, and an averaging is applied to the sample. If the model has converged, then the system terminates. If it does not converge, the stress calculation is performed again with the new stiffness modulus. This method was rigorously tested on 2D data sets, demonstrating its effectiveness even in scenarios where the inclusion has a uniform modulus, a Gaussian relative modulus with a mean value of 3, or an inclusion where no modulus smoothing was performed. The first two data sets where smoothing was performed converged to a final value, showcasing the potential of the approach.

Further, the 2D plane strain case was contaminated with noise consistent with two different levels of SNR magnitude to test its robustness further. Through this experiment, it was found that there was no significant change in the noise throughout the FEA's iterations, indicating robustness of the method in handling the noise. Finally, a 3D breast elastography was simulated through a Finite Element contact problem model, where a 5mm compression was induced. The slice containing the tumor was the target of the FEA's solution to provide the necessary values for the algorithm's initial values. When the reconstruction algorithm was run, the results converged after 11 iterations, indicating a 12% error. This reconstruction algorithm can determine the stiffness of the tissue in both the background and inclusion with reasonable error but makes assumptions about plane strain, which, as mentioned before, are not consistently enforced in contact scenarios such as between the prostate and rectal wall. Therefore, it is recommended that a more advanced approach be used in determining tissue stiffness, underscoring the need for caution and further research.

Mousavi *et al.* introduced an approach to reconstruct prostate stiffness after imaging, which has significant implications for prostate cancer diagnosis and treatment. The method utilizes pre- and post-compression images to determine tissue strains, which are then used iteratively to calculate tissue stiffness. The method for calculating tissue stiffness is based on an inverse relationship derived from Hooke's law of linear elasticity, as shown in Equation 1.24. The researchers employed an FEA method to determine whether the iteration converged to the strain image. This study involved a clinical study of 5 patients who underwent radical prostatectomy due to the presence of adenocarcinoma of the prostate gland. The samples were fixed and a Sonix RP US system with a BPC8-4/10128 element curvilinear probe was used to capture the strain data [47]. Once the samples were obtained, a pathologist examined, localized, and contoured the cancerous regions of the prostate gland. Statistical analysis was performed on the tissue stiffness values to determine the top 5% stiffest region, which was considered the tumorous region. The highest stiffness region was determined by normalizing the stiffness and using a Z-score to determine relative stiffness. A Dice similarity coefficient evaluates the overlap between the histopathology region and the iterative FEA calculated region.

$$\frac{1}{E} = \frac{\varepsilon_{yy}}{\sigma_{yy} - \nu\sigma_{xx}} \tag{1.24}$$

The proposed algorithm, while showing promising results, concludes that a larger study be conducted. The findings from the study show that the Dice coefficient for the datasets are 0.74, 0.38, 0.26, 0.63 and 0.34 for the 5 samples. The stiffness reconstruction was able to accurately identify the regions for 4 of the 5 samples, with a radius range from 2-7mm for the sample tumors. Additionally, 76% ± 28% of the tumor region detected with the iterative reconstruction method was inside the area identified with histopathology [47]. The reconstruction led to some artifacts close to the rectum and probe contact location; as this region is outside of the prostate capsule, it can largely be ignored and does not impact the overall effectiveness of the reconstruction [47]. The need for a larger study is crucial to conduct statistical analysis and conclude on the effectiveness of the method.

More information about the tissue is needed to create a higher-accuracy reconstruction algorithm. Required data includes other tissue parameters, such as Poisson's ratio for tissue incompressibility and the shear modulus—a paper by Islam *et al.* proposed a way to image Young's modulus and Poisson's ratio *in vivo* [48]. They used 40 simulated 3D datasets with varying contrasts and homogeneity. The boundary conditions were also varied to determine the effects on the Poisson's Ratio reconstruction. It was found that even in complex boundary conditions, they could reconstruct Young's Modulus with 90% accuracy. To test the proposed reconstruction method further, the group conducted a phantom study on a tofu phantom. Selected results are shown in Figure 8.

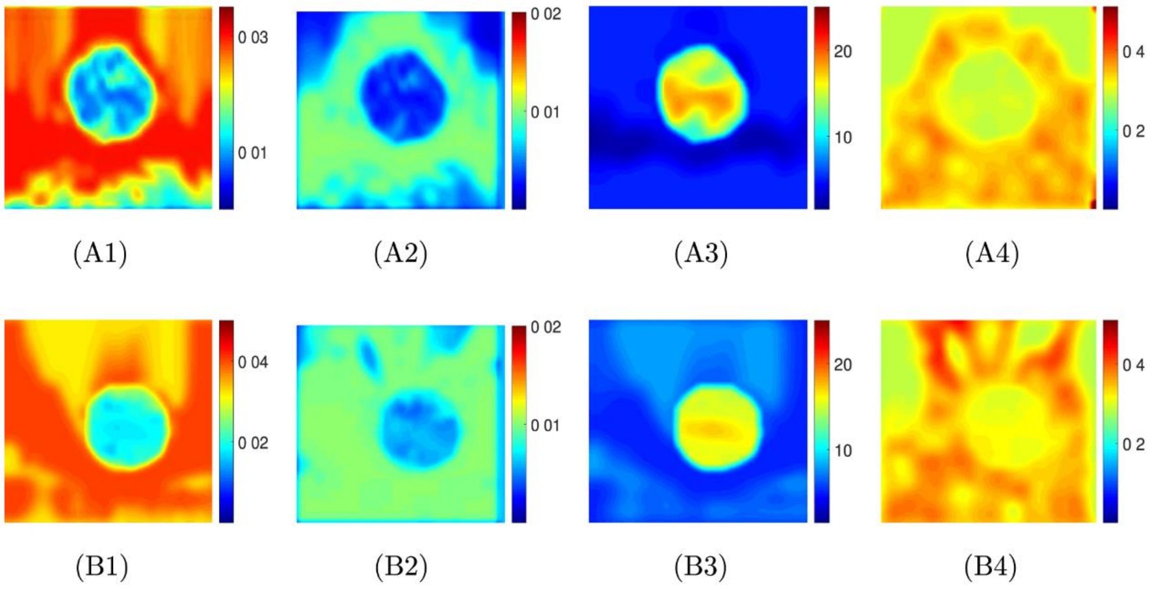

Figure 8: Reconstruction results from the Tofu Phantom Study [48]. A1 and B1 are the axial strain values, A2 and B2 the lateral strain values, A3 and B3 are the Young's modulus and A4 and B4 the Poisson's ratio of the tofu phantom.

In Figure 8, A1 and B1 represent the axial strain, A2 and B2 the lateral strain, A3 and B3 represent the Young's Modulus in kPa, and A4 and B4 are the Poisson's ratio images. This reconstruction method utilizes an iterative cost function minimization approach to calculate Young's Modulus and Poisson's ratio. It is crucial to note that this method requires the integration of an additional force sensor [48] to measure the applied stress accurately with any probe that utilizes it. While accurate, this method is not readily available to all clinical settings, as more advanced US systems with integrated force sensors must be available. This paper does not attempt to fuse the Poisson's ratio with other data to generate a shear modulus image, which can lead to improved imaging results [49].

1.6 Research Objectives

The research conducted aims at enabling clinicians to have an accurate and fast imaging modality capable of detecting prostate cancer. To allow for this several objectives must be met and are outlined below.

1. Alterations to current tissue displacement tracking estimation and refinement software algorithms (AM2D and STREAL) must be made and validated. This alteration primarily involves redevelopment of these methods in the polar system to make them adaptable to data generated with endorectal probes. To validate results, *in silico* data and a known ground truth are used to determine the accuracy of the displacements and strains. The additional use of tissue mimicking phantom data to study a more realistic acquisition and tissue sample further aids in validating the proposed changes.

2. A novel approach to image reconstruction, known as Poisson's ratio image reconstruction, can allow for better segmentation of results and enables data fusion as calculating the shear modulus is viable with known compressibility and stiffness. Thus, allowing for stiffened tissue to be easily identified and quantified by clinicians. This algorithm is validated against known *in silico* data results and against data collected from a tissue-mimicking phantom.

1.7 Overview of Current Issues

As outlined in Section 1.6, research in elastography is extensive for linear transducer acquisitions, however the field is lacking in research in areas related to non-linear transducers, such as the ones used in TRUS procedures for prostate cancer detection. Displacement tracking algorithms such as AM2D and STREAL can produce high quality displacement estimations and strain images but have only been developed for use with linear US transducers. To further extend the usefulness of elastography to prostate cancer detection, new alterations to the existing methodology must be conducted and tested. These alterations will include changes to the fundamental way in which AM2D performs grid interpolation and estimation, while STREAL requires alterations to the convolutional method of calculating the Laplacian, Boussinesq, and compatibility equations. The alterations made to these algorithms need to maintain USE's real-time processing and display accuracy to help ensure clinicians can continue to utilize US for its largest advantage.

In addition, the current research around Poisson's ratio reconstruction for tissue mechanics seeks to validate the iterative method and show that it is a viable method of determining if a tissue's mechanical properties have changed due to cancer related biological processes. It stops short, however, of proposing a use for the acquired data. To help highlight tissue stiffening, Poisson's ratio can be used with the stiffness that is calculated simultaneously, to display the shear stiffness of the tissue. This would provide an accurate view of the tissues current properties that accounts for the incompressibility of the tissue and the stiffness. Combining the information found in the FEA based image reconstruction, while taking longer to produce, can provide increased accuracy and clarity when observing changes in the tissue mechanics of the prostate leading to better overall understanding of the current health of the imaged prostate tissue.

1.8 Thesis Outline

This thesis consists of five chapters, with the first being the introduction chapter. The remaining chapters will discuss the production of *in silico* and tissue mimicking phantom data sets, the alterations made to AM2D and STREAL, and the results from the test data sets. The fourth chapter will consist of the results of the Poisson's ratio reconstruction and discussion around the impact of this algorithm. The final chapter will consist of conclusions and recommendations for future work in this area.

1.8.1 Chapter 2: Data Generation and Acquisition

Before any displacement tracking algorithm can be developed, a suitable data set for testing must be acquired to validate and benchmark the algorithms results. A common way of testing algorithms initially is through the creation of completely simulated data sets. This way the material properties and geometry are known and controlled for. Additionally, displacement fields can be generated and applied to the material such that the outcome of the displacements and strains are known prior to evaluation by AM2D or STREAL. After validation against known ground truth data, an element of realism can be added by creating a tissue mimicking phantom, which aims at mimicking real tissue with the acquisition of data being done by an ultrasound transducer in the same manner that would be conducted in a clinical study.

1.8.2 Chapter 3: AM2D alterations and STREAL Refinement

The created data sets are useful tools to test the alterations made to AM2D and STREAL. Alterations to AM2D aim at converting the underlying mathematical formulations, such that a polar grid is used for minimization calculations and dynamic programming. These alterations would allow for initial estimates of the displacement field from TRUS probes used in prostate cancer biopsy and screenings. The outcome of the initial guess is then refined using STREAL's tissue mechanic enforcement. The data from both the *in silico* and tissue-mimicking phantom (TMP) studies are used to determine the performance of AM2D's initial guess, and the improvements that STREAL can create through its refinement algorithm.

1.8.3 Chapter 4: Poisson's Ratio Reconstruction Algorithm

Once the displacement and strain data from AM2D and STREAL is collected, it can be used in an iterative FEA based reconstruction algorithm aiming at calculating the material's Poisson's ratio and Stiffness. These two material properties can lead to better understandings of the imaged tissue and any potential current malignancies within the tissue. By calculating the Stiffness and Poisson's ratio, the shear modulus of the tissue can also be calculated for the entire data set, allowing for a combined view of the materials properties and detection of any areas in the tissue that may be stiffening in the shear direction. This will provide clinicians with a tool that can combine the advantages of a stiffness reconstruction and a incompressibility construction of the targeted tissue.

1.8.4 Chapter 5: Conclusions and Future Work

The final chapter concludes the work that has been completed and reiterates the competency of each aspect of the project in its ability to contribute to the completion of this project. It also contains several recommendations on future work that will build upon this project, such as completing a clinical trial of the algorithms to further learn the capabilities of AM2D, STREAL and the final reconstruction algorithms.

Chapter 2

2 In Silico and Phantom Data Generation

In the development of USE algorithms, known input and output data are essential for validation. One of the main ways to develop data sets for validation is through manual generation. This involves selecting ideal data that will create perfect input conditions. This method is particularly advantageous for novel or untested algorithms as it allows for the creation of an ideal output and the assessment of accuracy. Alternatively, there are methods of producing more realistic data using advanced software simulations, such as Finite Element Analysis (FEA), or *In Silico* RF data generation software, such as Field-ii or MATLAB Ultrasound Toolbox. Additionally, tissue mimicking phantoms are a faster and more controlled alternative to clinical studies, as the mimicking material can be created to user specifications and will not require ethical clearance, allowing for a rapid way of testing algorithms using data collected from a real US system.

2.1 Field-ii *In Silico* Data Generation

Initially developed in 1992 and released in 1996 for general use, Field-ii is a software package that seeks to generate high-quality and accurate *Silico* data sets for US systems. Developed and maintained by Jørgen Arendt Jensen [50], Field-ii employs methods to allow users to mimic commercial transducers. Any researcher has access to a range of parameters and may use available bitmap or DICOM data to generate US RF datasets. Field-ii utilizes the spatial impulse response of a system to generate its result; this concept was first described by Tupholme and Stepanishen in their papers [50] [51]. These papers outline the mathematical foundations of determining the pulsed and continuous wave cases, which enable simulating excitation by convolving the spatial impulse response with the excitation function used to generate the wave. Dividing the transducer into square sub-sections, researchers sum the response from these squares to use as a received signal, simplifying the application of apodization with a transducer geometry treated as a piston [52]. Since the sub-sectioned squares are small, researchers can use a far-field approximation, simplifying the simulation and reducing the time cost. With the spatial impulse response, the sampling frequency is often in the range of Gigahertz to overcome discontinuities. To allow for Megahertz frequencies typically found in US systems, Field-ii utilizes precise tracking of the time positions of the response and employs the integrated spatial response as an intermediate calculation step [53]. This software allows for a practical and straightforward way of generating RF data for realistic results. The MATLAB implementation allows users to interact with the software to set parameters for the transducer, the desired apodization, focus depth, and the number of scatterers in the image. These parameters allow for generating realistic RF data from images of *in Vivo* organs or tissue mimicking phantoms.

A practical implementation of this can be seen in generating realistic US RF data for a kidney scan. The process, which is not only precise but also practical, starts with using a scatterer generation algorithm that creates scatterer positions based on the image size and desired image dimensions after the scan. This algorithm, designed with practicality in mind, ensures that the scatterer positions are generated efficiently. Additionally, the amplitude of each scatterer sample is scaled to the pixel's intensity in the bitmap image. For instance, a higher pixel intensity value in the original image produces a scaled variance in scatterer amplitude. For example, a 1,000,000-scatterer image may be generated with final dimensions of 100mm by 100mm by 15mm using the code found in Appendix A1. The transducer parameters can be generated once the scatterer positions and amplitudes are made. These include the number and size of elements for the transducer, the focal depth, the excitation function, and the apodization. An example of a linear transducer with 128 elements and the code used to generate the transducer can be seen in Appendix A2. From this example, a bitmap image of a kidney slice can generate an accurate RF data set that is visualized using a brightness mode (B-Mode) image in Figure 9.

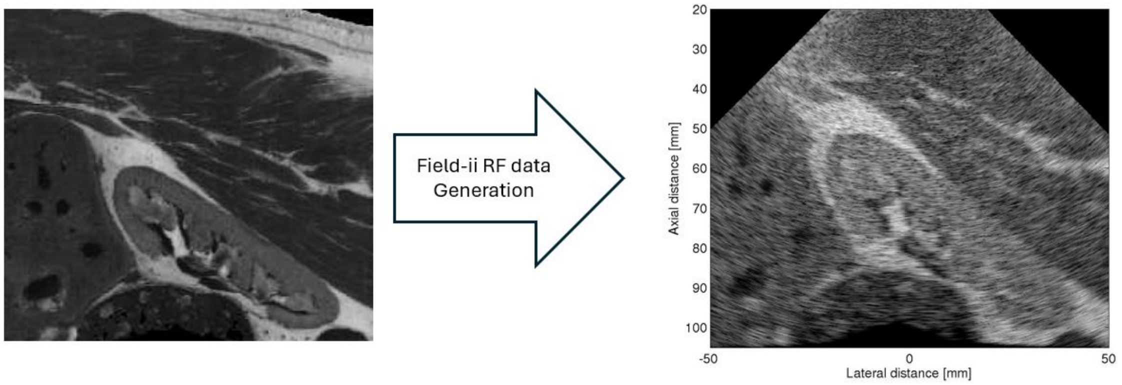

Figure 9: Original Bitmap image processed by Field-ii to compute a simulated RF dataset [54]. This B-Mode image is generated from the simulated RF data collected by the Field-ii software scanner.

While this example produces a high-quality scan of the kidney, it is computationally expensive as the software utilizes single line acquisition techniques to acquire the image line by line. The computation time can be decreased by utilizing parallel computing or reducing the number of scatterer points.

2.2 FEA Modelling with Human Anatomy

In addition to In Silico RF data, realistic displacement and strain measures in deformed tissues are often required to determine ground truths to validate USE techniques, as seen in numerous papers mentioned in Chapter 1.6. To compute these values, FEM can be used to create life-like 2D and 3D models of human anatomy and apply contact simulations with geometry-mimicking imaging tools. Abaqus is a well-known and widely used FE software that can be programmed to iteratively apply loading conditions to a model while calculating desired parameters such as stress, strain, or displacements. Abaqus can help generate datasets with Field-2 or as a ground truth to compute metrics from the outputs of displacement tracking algorithms such as AM2D or STREAL.

An example of using FEA of human tissue can be seen in modeling the human breast during contact loading. Samani *et al.* propose a method of simplifying the complex meshes required to accurately model the geometry of the breast using a voxel-based meshing algorithm. The mesh used is an 8-node hexahedral element with a smoothing technique that corrects irregular boundaries. The size of the elements is also considered, as a smaller mesh will yield a more accurate geometry and result but at the cost of computation time. The research group decided to increase the mesh size to allow for computational times to remain acceptable while still leveraging accurate results from the mesh. In enforcing the method described in detail in [55], a finite, multi-tissue model can be created, as seen in Figure 10.

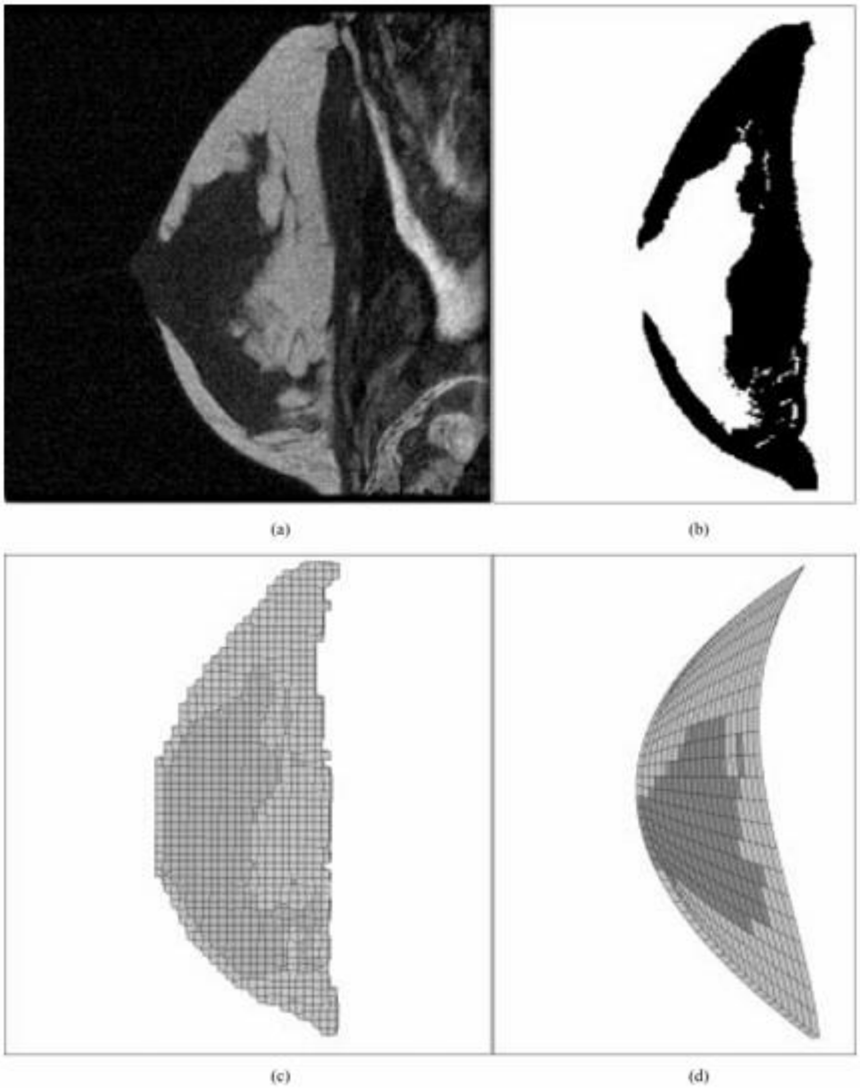

Figure 10:(a) Breast MRI Scan (b) breast tissue segmentation (c) Breast tissue assignment in Abaqus (d) Final Finite Element Mesh [55].

The meshing can be produced from this slice of MRI data, then segmented and processed into a FE mesh that can be loaded in an FEA solver software. This tool may be extended to other organs such as the prostate, where the geometry can be modeled, segmented and meshed to present an accurate model of the geometry.

To model the prostate a FE model was created in Abaqus such that the model contained a 2D slice of the prostate capsule within a homogeneous background. Once this part was created and meshed using a quadrilateral mesh, material properties were assigned for the prostate and background material. Element types of CPS4R were used for the prostate and the background elements. The prostate material and background material have values of 0.495 for the compressibility. The Young's modulus value for the Prostate capsule is 60 kPa, and 20 kPa for the background material. The edges of the model were fixed and were far enough away from the contact point such that all displacements would be 0 in the elements preceding the fixed nodes. This allowed for the model to remain in place during contact, while still maintaining the desired trend displacements throughout the tissue. Additionally, a 2D transducer was modeled such that the diameter was consistent with a TRUS probe. The probe was made rigid such that no deformation would occur during the contact. Once both parts were modeled, a job was created such that the rigid probe would contact the bottom of the prostate with a frictionless contact, and then move 1mm into the tissue, mimicking the compression phase of the scan. The full contact model can be seen in Figure 11.

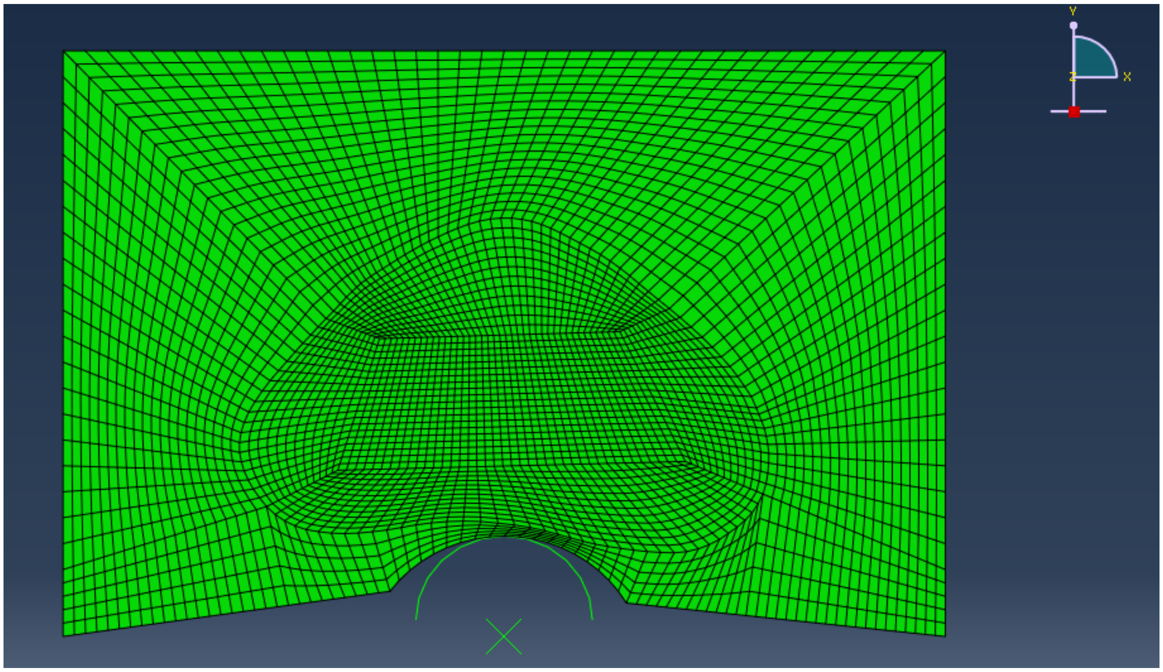

Figure 11: The prostate capsule and Transducer modeled in Abaqus. The model was prescribed boundary conditions for the outermost elements and the transducer was made to contact and displace upwards by 1 mm. The material properties for the Prostate and Background were applied based on known median values.

2.3 *In Silico* Data Generation Results

Leveraging the tools described previously, it is possible to generate accurate *in-situ* RF data using Field-ii that can be modified using solutions from an FEA solver such as Abaqus. This allows for a pre-and post-compression data set to be formed, facilitating algorithm changes to AM2D and STREAL for polar data to be validated against known solutions.

A bitmap image of a prostate phantom was used to generate the precompression data. This phantom was created using the methods outlined in [14] and imaged using an MRI to determine the geometry. From the generated Dicom data, bitmap images can be created, and values scaled such that the bitmap values are in 16 bits to comply with Field-ii and its scatterer function input requirements. This input image for the data set is illustrated in Figure 12.

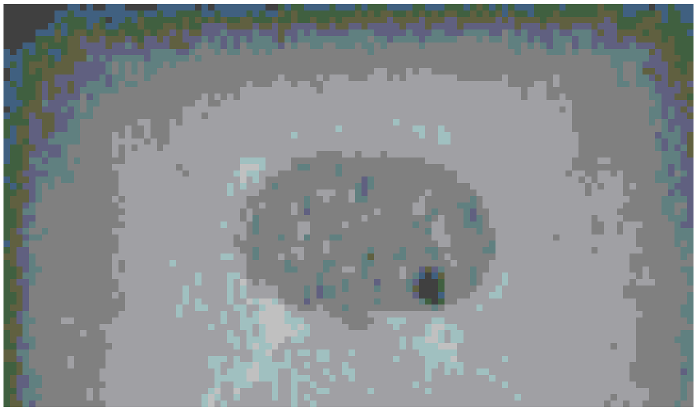

Figure 12: The input bitmap image showing a prostate tissue mimicking phantom for the scatterer dataset. The central dark inclusion in the background material is the prostate capsule. This 16-bit depth bitmap can be used to create a scatterer map for input into the Field-ii scanner.

The prostate scatterer data is created using the algorithm outlined in Appendix A4. This function takes in the desired bitmap image and the total number of scatterers to be generated. The function is an altered form of the one found in Appendix A1, where the size of the output image is consistent with the phantom section that was used. Figure 13 shows the input bitmap image and Figure 13 the resulting scatterer generation for a one million scatterer image.

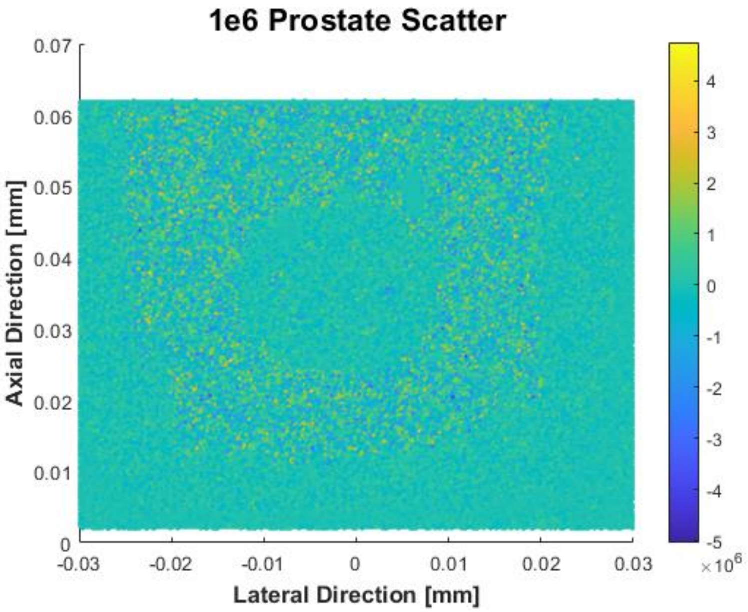

Figure 13: A One Million scatterer plot using the prostate phantom bitmap image as an input bitmap image. The central prostate inclusion can be seen. This scatterer map shows the different amplitudes that make up the background and prostate tissue.

After generating the scatterer location and amplitude, the transducer, and its parameters, must be generated. Several transducers were created to capture different performances. A 256-element transducer was created to mimic an Ultrasonix RP scanner. The result of generating this transducer can be seen in Figure 14. The algorithm to complete this can be found in Appendix A4.

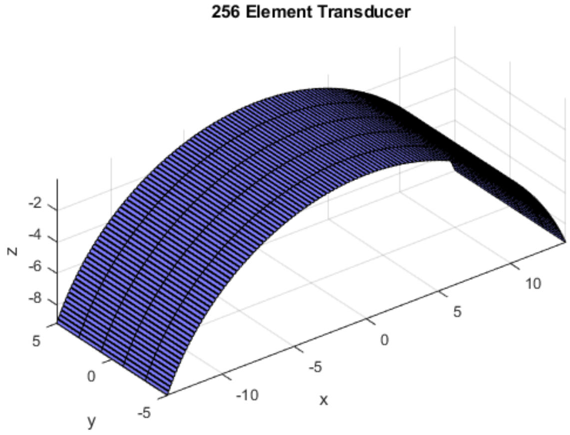

Figure 14: The 256-element transducer used to generate the In Silico Data sets. This scanner is utilized by Field-ii to generate the RF data from the scatterer field.

After generating the transducer, the excitation, signal apodization, and focus for each element is created. The focus shifts as each element are used in the single line acquisition method to generate the RF data. A generated RF data set visualized as a B-Mode image, seen in Figure 15.

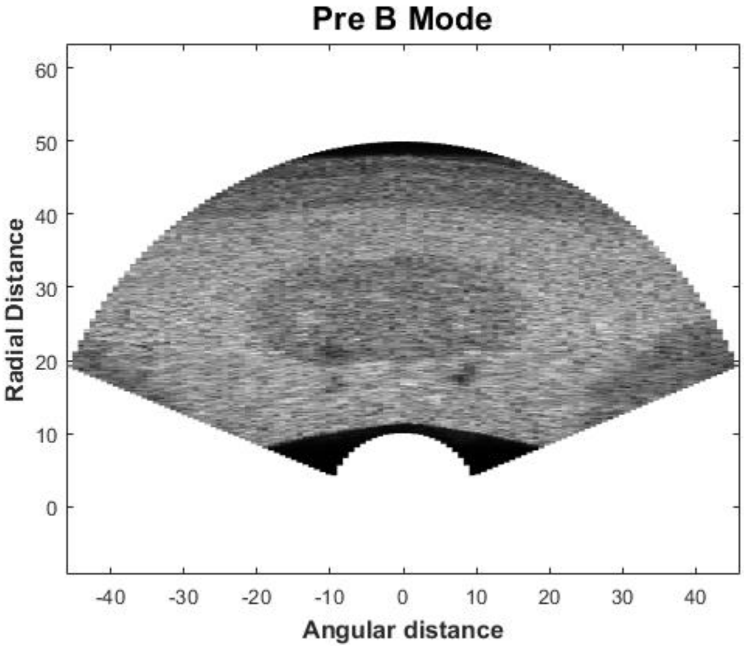

Figure 15: Using the 1-million scatterer data map and the 256-element transducer, RF is produced and visualized here as a B-Mode image.

Once complete it is now necessary to generate the post compression RF data. To realize this, the pre compression scatterer data, and a FEA model are utilized to displace the scatterers according to the solutions from the FEA model. These displacements can be visualized in Abaqus and can be seen in Figure 16.

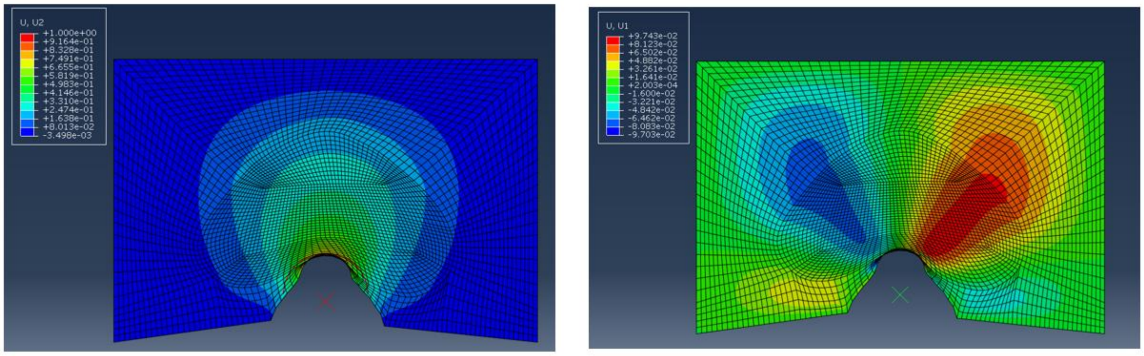

Figure 16: The measured tissue displacements from Abaqus in the x and y directions. These displacements are extracted from Abaqus and converted to the polar coordinate system using MATLAB.

The generated displacement data is then extracted and loaded into MATLAB, where scatterer points and the related displacement at the point is generated using the scattered interpolant method, and the displacement FEA data. The code for this can be seen in Appendix A5 and the output data can be visualized in Figure 17.

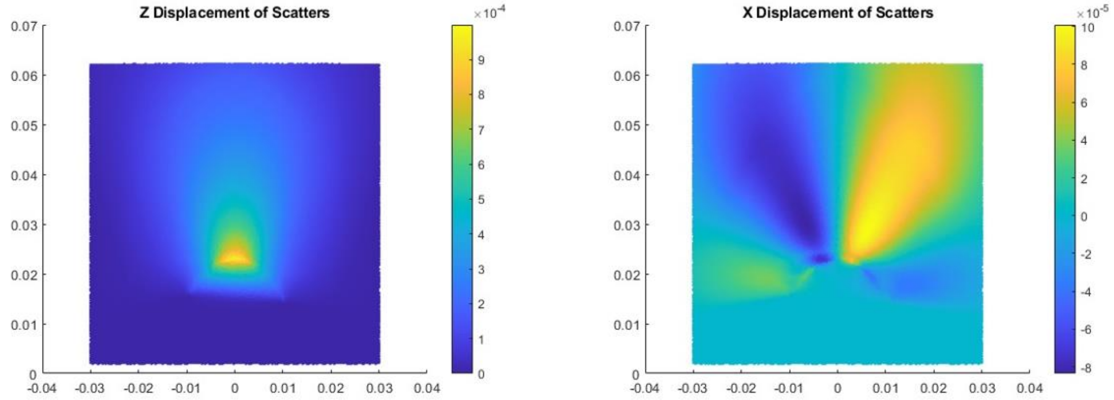

Figure 17: The R and Theta scatterer displacements extracted from Abaqus and applied to the original scatterer map. This process creates a displaced scatterer field that can be used as a post-compression scan.

Finally, the displaced data set generated through the code in appendix A5, is input into the scanning algorithm used in appendix A4 to ensure that the same transducer and settings are used to scan the post compression tissue. A final visual of both the pre and post compression B-Mode images can be seen in Figure 18, and the RF data for this pair will be used as the In-Silico data for AM2D and STREAL in the following chapters.

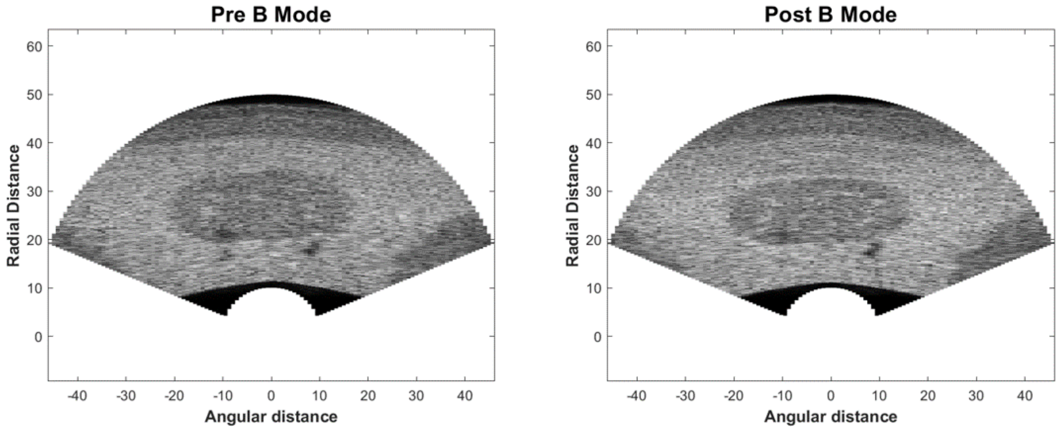

Figure 18: The Pre- and Post-compression B-Mode images generated from the RF data collected from Field-ii.

To compare the output data sets to the known truths, the displacement and strain data calculated in Abaqus was extracted using a Python script and visualized in MATLAB. The images produced from this method can be seen in Figure 19.

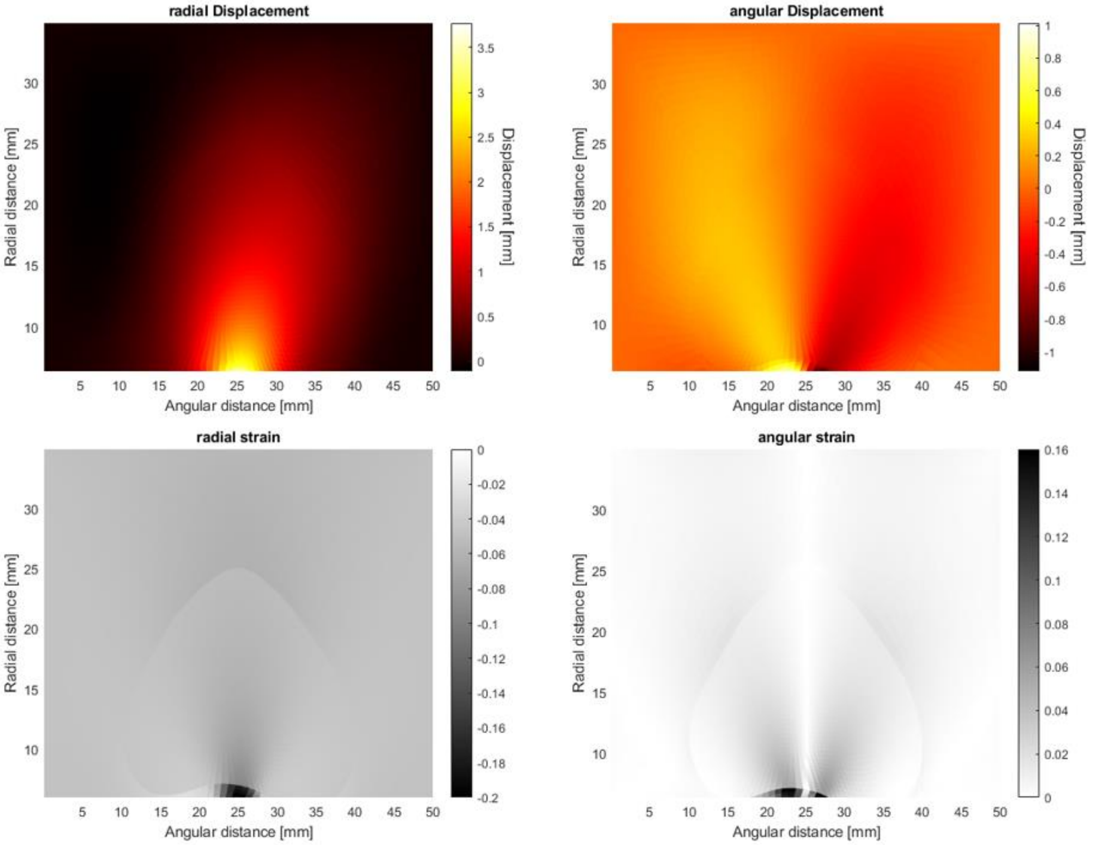

Figure 19: The output data from Abaqus for the Radial Displacement and Strains, as well as the Angular displacement and strains.

The visualizations from Figure 19 show that the radial displacement and strains are symmetric about the center vertical line, whereas the angular displacement and strains are anti-symmetric about the same axis. This is the expected result from the FEA as the displacements from the curved transducer would create a symmetric outward displacement in the radial direction and would deform in opposite directions along the angular direction. The exact displacements and deformations can be described using the Hertzian contact model as the surfaces in contact are continuous frictionless elastic half spaces, with small strains, and the surfaces are non-conforming [56]. This leads to the expected numerical solutions using FEA and which are visualized by Figure 19.

2.4 Tissue Mimicking Phantom Data

Following confirmation of the algorithm with established benchmarks, a broader study is necessary to evaluate the system's performance with data that better reflects real-world conditions. Data may be collected through a clinical trial, or by conducting a Tissue Mimicking Phantom (TMP) study. In clinical trials, patient data is collected and acts as the input data set. Clinical data exposes algorithm imperfections such as image artifacts or scans that show abnormal anatomical structures. The most considerable downside to conducting the study is the time it takes to both gain approval from regulatory bodies and collect the data once approved. TMP studies offer a quicker alternative to clinical trials. Researchers construct a volume of material with similar properties as the tissue where internal anatomy mimics the intended human anatomy. Through the introduction of different materials, TMP allows for quick construction and control over the types of artifacts or abnormalities in scans. Therefore, TMP study offers a rapid and controlled environment for algorithm testing, providing high confidence in the results.

Researchers must control conditions to ensure TMP properties resemble those of human tissue. For accuracy it is essential that the speed of sound, acoustic impedance, and attenuation within both the background and inclusion medium closely resemble those in human tissue, while the background material and inclusion's density should replicate human tissue's density. M. Culjat *et al.* [57] provide a comprehensive review of tissue substitutes for use in TMPs in their literature on material options. This research intends to measure sound speed, attenuation, backscatter coefficient, and material nonlinearity to facilitate better TMP design for various tissue types [57]. As the prostate and surrounding tissue do not contain hard tissues that interfere with the imaging process, only soft tissue replacements are considered. The measured properties of interest for the prostate and surrounding tissue are a sound velocity of 1561m/s, density of 1670 kg/m^3, attenuation of 0.8 dB/cm MHz, and an acoustic impedance of 1.65 MRayl.

The average soft tissue has a speed of sound of 1540m/s, a density of 1043 kg/m^3, an acoustic impedance of 1.63MRayl, and an attenuation of 0.54 dB/cm MHz [58]. Table 7 summarizes the acoustic properties of several tissue alternatives. From Table 7, the gelatin-based tissue phantom has the most similar acoustic properties to the average soft tissues. In their review, Culjat states that gelatin is a commonly used TMP material and, when combined with a preserving agent such as alcohol or formaldehyde, can last for several of weeks if stored under the right conditions [57].

Table 7: List of Acoustic properties of common TMP materials [57].

Material	Velocity (m/s)	Density (kg/m^3)	Attenuation (dB/cm MHz)	Impedance (MRayl)
Agarose - based	1498-1600	1016-1100	0.04-1.40	1.52-1.76+
Gelatin – based	1520-1650	1050	1.60-1.73	1.60-1.73
Magnesium Silicate – based	1458-1520	-	-	-
Oil Gel – based	1480-1580	1040-1060	1.54-1.67	1.54-1.67
Open Cell Foam – based	1540	-	-	-
Polyacrylamide Gel - based	1540	1103	1.7	1.70
Polyurethane	1468	1130	1.66	1.66
Polyvinyl Alcohol - based	1520-1610	-	1.60-1.77	1.60-1.77
Tofu	1520	1059	1.61	1.61
Water - based	1518-1574	1000+	1.48-1.60	1.48-1.60
Urethane Rubber	1460	900	1.31	1.31

To enhance the tissue model's realism, a scattering element is added as gelatin alone does not mimic the heterogeneous nature of human tissue under ultrasound. Scattering agents such as graphite or silica beads may act as a scattering agent [57]. The material properties for gelatin can be found in Table 8.

Table 8: Material properties of Gelatin [59].

PROPERTY	VALUE
POISSON’S RATIO	0.5
YOUNG’S MODULUS	67 - 73.4 kPa
SHEAR MODULUS	22.3 – 24.47 kPa

The prostate capsule is made of a material that allows it to be clearly distinguished from the background gelatin. This material can consist of any material with properties like the prostate. R. Lerski *et al.* propose reticulated foam as an alternative to human or animal tissue [60]. By using reticulated foam, lead times for sourcing human or animal tissue samples are avoided. Reticulated foam allows for increased phantom preservation time and does not require a preserving agent to maintain its material properties. The foam may be cut to any shape to mimic a desired organ. The Researchers then soak the foam in a saline solution prior to placing it in the gelatin solution to better match the speed of sound in human organs. Further studies conducted by the research group found that the attenuation coefficient of the foam to be like the attenuation coefficient of water [60].

A TMP was created to develop a more realistic dataset for evaluating the AM2D and STREAL polar algorithms for prostate cancer detection. A gelatin background with a foam prostate capsule was determined to be the optimal selection where the gelatin fulfills the acoustic property requirements for the background material, and the foam meets the necessary conditions for simulating the prostate while it enabled varying tissue incompressibility. The latter was necessary in the validation of the proposed Poisson's ratio reconstruction technique. The phantom was primarily constructed of gelatin, where the exact mixture is approximately 10g of gelatin set in 500ml of water, with 30g of #10 100-170 grit silica glass beads added to the gelatin. The mixture was stirred constantly until the gelatin began setting to ensure an even distribution of the scattering agent. The foam prostate was cut to the approximate dimensions of the prostate, about 3cm x 3cm x 5cm [61], and allowed to briefly soak in a saline solution to avoid total saturation, as the goal was to produce a large difference in incompressibility between the inclusion and background material. To avoid movement of the prostate capsule during the curing process and ensure it remained under the gelatin surface, the capsule was added to the gelatin mixture after it began to set without disturbing the material continuity of the phantom. A plastic tube was inserted into the mixture to create a cavity to simulate a rectal cavity where a TRUS procedure would occur, with the location of the cavity being alongside the prostate. After the mixture was fully set, the plastic tube was removed, leaving a small cavity for inserting the probe. The completed phantom is seen in Figure 20.

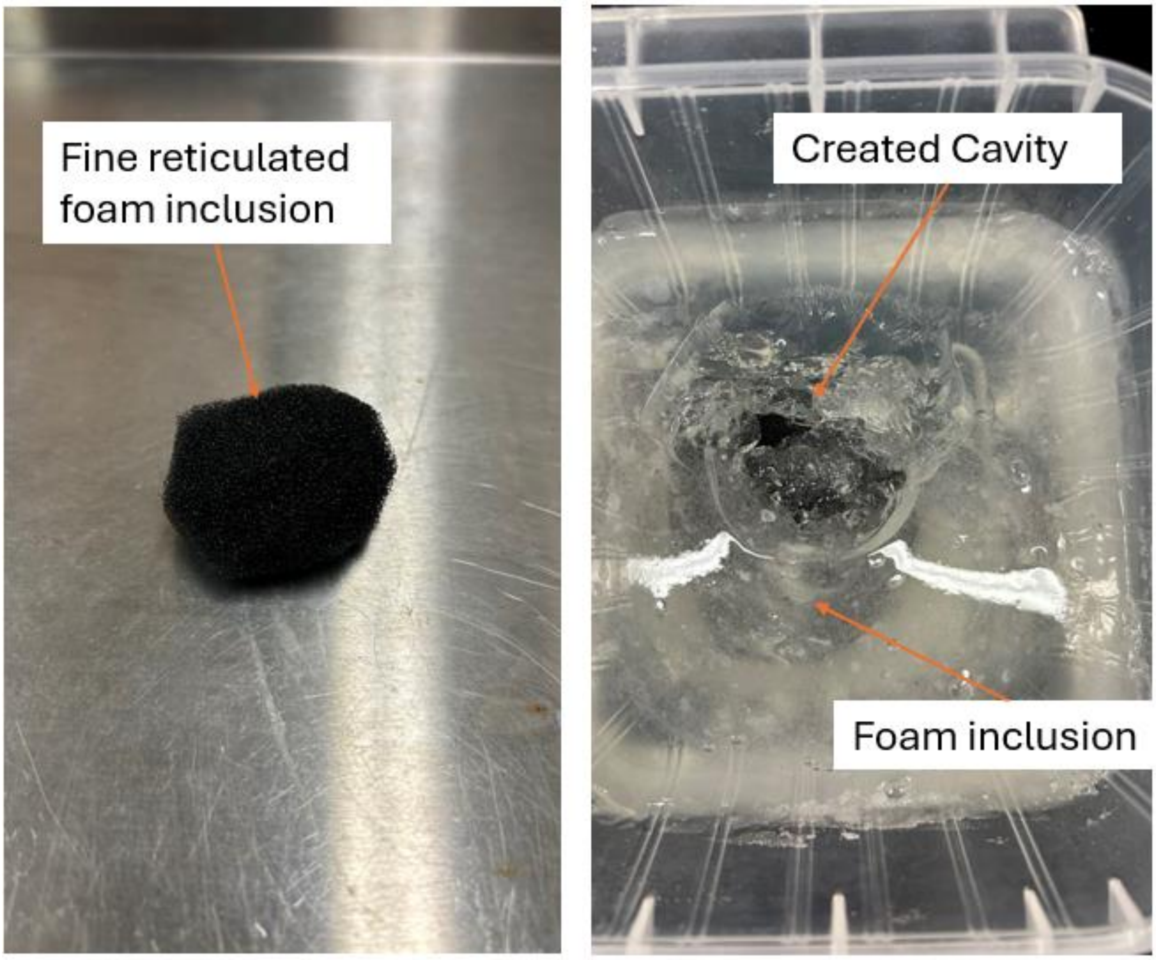

Figure 20: The TMP foam inclusion (left), and Gelatin background with cavity and inserted foam inclusion (Right).

2.5 Ultrasound Settings for the Imaging of TMP

To collect the RF data from the constructed phantoms, an Ultrasonix RP scanner was used with two ultrasound scanners, a Ultrasonix L9-4/38 linear transducer and a BPC8-4/10 side-fired TRUS probe. The transducer and system settings were set according to the depth of the prostate phantom and the desired region of focus. The exact settings used during the data collection process can be found in Table 9. Settings are consistent for all samples gathered for both pre- and post-compression acquisitions.

Table 9: Parameters used for data collection with Linear and TRUS Probes.

	LINEAR PROBE	**TRUS PROBE**
DEPTH (CM)	5	4
FOCUS DEPTH (CM)	2.5	3
FREQUENCY (MHZ)	7	5
FRAME RATE (FPS)	14	12
GAIN (%)	57	52

2.6 Collected Data and Quality Analysis

The ultrasound system collects the data in an RF file format. Files are processed using Reza Zahiri Azar's MATLAB function found in Appendix B1, initially created out of the University of British Columbia in 2008. This process yields MATLAB formatted files for each data frame from the scan. The MATLAB files can be quickly loaded and manipulated by displacement estimation or quality analysis algorithms. To validate displacement algorithm changes for polar transducer displacement estimation, researchers calculate the MSE, and correlation score obtained from a frame pair of pre- and post-compression data sets with its corresponding "ground truth" to ensure their quality. The correlation score is tabulated to determine the best, average, or worst set of pre- and post-compression data. Best-case data may be used for further validation against artifact-free data. Average data sets can be used to assess algorithm performance on realistic data that may include minor artifacts or decorrelation between the post-compression data. The worst-case pairs show how the algorithms perform on low quality images with respect to the SNR, CNR, decorrelation, or significant obtrusive artifacts in the image data. The algorithm outlined in Appendix B2 is used to analyze the collected data against all pre- and post-compression scan frames. This method utilizes AM2D to quickly determine the displacement field between a pre- and post-compression data set. This displacement field is used to create the reverse and forward functions to warp the first frame. The warped frame is then compared to the second compressed frame to determine the correlation and MSE, where lower combined scores are preferred. When testing the displacement algorithms, this method is repeated for each pre- and post-compression frame to classify each pair for usage. Table 10 contains some selected quality scores from the TRUS probe data collections, where the MSE summed with $(1 - CC)$ used to determine the overall score for the pair.

Table 10: Selected Data points from the data quality analysis done on Phantom scans.

Pre scan frame	**Post Scan frame**	**Combined MSE and CC Score**	**CC Score**	**MSE Score**
126	**26**	2.53	0.0035	1.54
80	**25**	2.54	-0.0042	1.54
17	**2**	3.35	0.039	2.39
26	**1**	3.35	0.043	2.40
64	**55**	4.62	0.0072	3.63
44	**126**	4.62	0.038	3.66

The first two rows of Table 10 show a low combined score between the data sets, corresponding to the best data quality; the second two rows show an average score for the data, and the last two rows show results from poor data quality pairs. Figure 21 shows a visualization of these data sets. In Figure 21 a), the B-Mode image shows the prostate capsule in the center of the image with minimal artifacts. The combined quality score of the original on the left and the displaced image on the right is high due to the similarity between the two images and the likeness when warped according to the displacement field. Figure 21 b) shows the average case, where some artifacts are present in the image and evident in the post-compression image to the right of the capsule. This will not significantly impact the displacement algorithms as the artifacting is outside the capsule. In Figure 21 c), a poor case can be seen; high image artifacts make distinguishing the prostate capsule difficult, especially in the pre-compression image on the left. Using this data to calculate the displacements may lead to erroneous prostate capsule displacement estimation and refinement results.

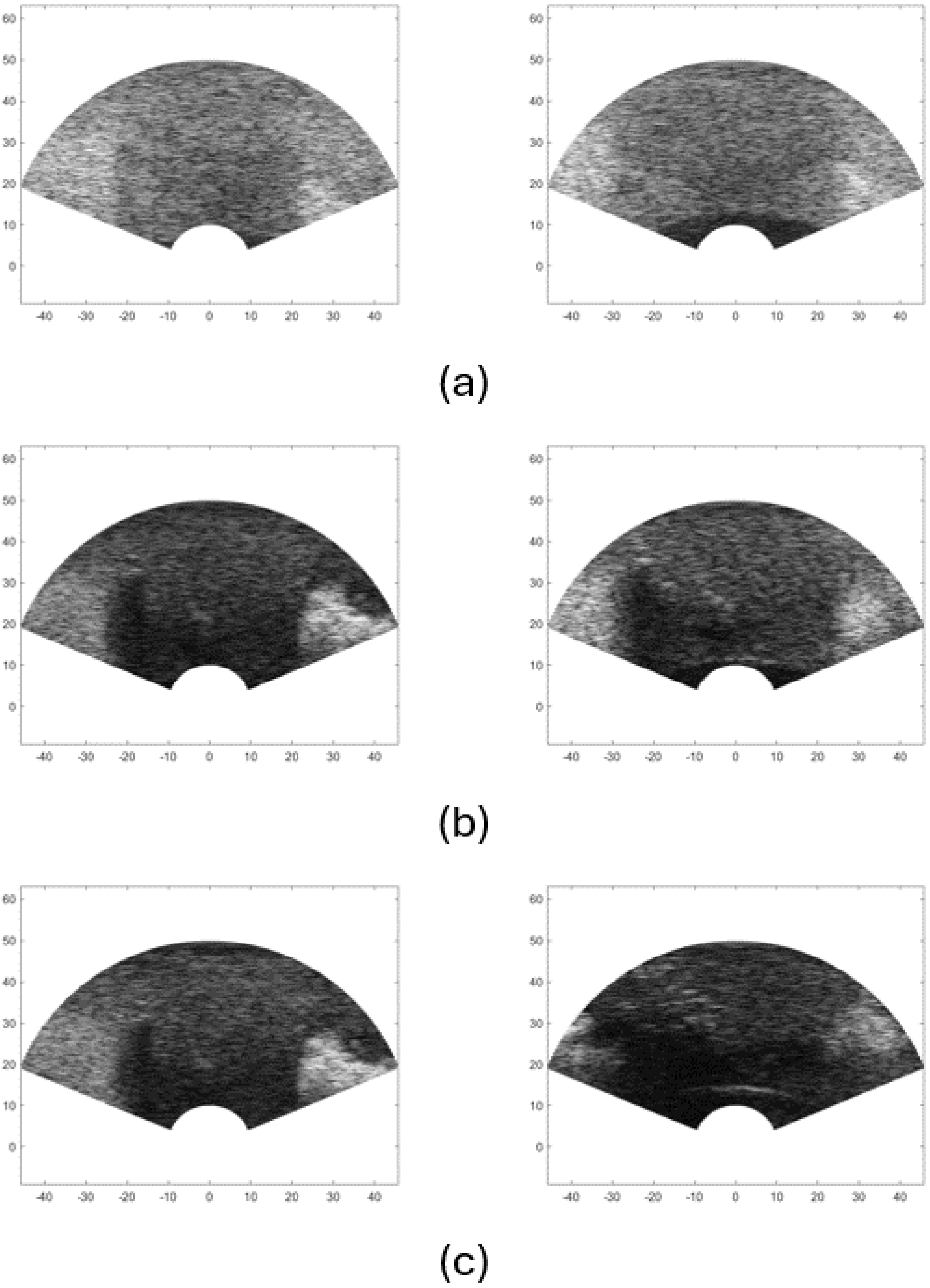

Figure 21: B-Mode images of the a) good quality pair b) average quality and c) worst quality compression correlation pair.

Using the data collected from the TMP, realistic data sets can be generated and used to analyze the accuracy and processing speed of tissue displacement tracking algorithms while utilizing a real US system where imaging artifacts, inconsistencies and poor data quality can be used to determine how the algorithm behaves in non-perfect data. The good quality pair will be used throughout the thesis as the basis for the TMP results.

Chapter 3

3 Polar Implementation of 2D Analytical Minimization

Following the completion of data set generation, the potential to modify existing algorithms for use with TRUS probes for the collected polar data was apparent. AM2D, developed by Hasan Rivaz [39] [40], employs a Dynamic Programming and 2-dimensional minimization approach to estimate the pixel displacements between two images, a pre-compression and post-compression pair. This method's rapid estimation capabilities enable the algorithm to be used in real-time, allowing US systems to maintain their competitive advantage over other imaging modalities in the field of prostate cancer diagnosis.

3.1 AM2D Displacement Estimation Algorithm

AM2D was selected for the initial estimate of the displacement for its ability to compute the displacement field between two input RF data sets while allowing the system to maintain its real time framerate [39]. When compared to other displacement methods it can be seen that the additional processing computed in GLUE or other algorithms such as OVERWIND [62] or SOUL [63] greatly diminishes the speed in which the displacement field can be generated. It was also found during a comparative study that the AM2D algorithm provides the best initial guess for STREAL to refine [64] as many of the lateral displacements become oversmoothed in OVERWIND and SOUL due to higher order image processing. Finally, AM2D has the fewest hyper parameters used in calculating the displacement field, making tuning the algorithm for each patient the most efficient.

To calculate the displacement field AM2D utilizes DP and Analytic Minimization. The dynamic programming method calculates the displacement for each scan line across the image by employing a regularized cost function that includes terms for both displacement continuity and amplitude similarity. The continuity term for a single scan line, *j,* with data at point *i,* down the scan line is seen in Equation 3.1 and the cost function is seen in Equation 3.2 [39],

$$R_j(a_i.l_i, a_{i-1}, l_{i-1}) = \alpha_a(a_i - a_{i-1})^2 + \alpha_l(l_i - l_{i-1})^2 \qquad (3.1)$$

$$C_j(a_i, l_i, i) = [I_1(i, j) - I_2(i + a_i, j + l_i)]^2 + \min_{d_a, d_l} \left\{ \frac{C_j(d_a, d_l, i - 1) + C_{j-1}(d_a, d_l, i)}{2} + R_j(a_i, l_i, d_a, d_l) \right\} \tag{3.2}$$

where R_j is the regularization term depending on regularization coefficients α_a and α_l, with displacements in the axial and lateral directions at the specific point *(i, j)*, a_i and l_i. The cost function C_j, depends on the data from Image 1 and Image 2, I_1 and I_2 along with the regularization term and previous cost function value. The process is repeated, line by line, until every scan line has been computed for all images. An integer pixel size displacement is provided for each direction. With displacements in elastography being very small, it is of interest to calculate sub-pixel estimations for each sample. Rivaz *et al.* propose using a method of 2D minimization from DP to obtain these sub sample results. To do this for both directions simultaneously an initial seed line is chosen, the center scan line in most cases, and the results calculated for this line are then propagated to the left and right of the image using the previous line to calculate the new sub sample values. Equation 3.2 is modified such that the cost equation now includes the subsample changes to the displacements, seen in Equation 3.3,

$$\begin{gathered} C_j(\Delta a_1, \dots, \Delta a_m, \Delta l_1, \dots, \Delta l_m) = \\ \sum_{i=1}^{m} \{[I_1(i, j) - I_2(i + a_i + \Delta a_i, j + l_i + \Delta l_i)]^2 + \\ \alpha(a_i + \Delta a_i - a_{i-1} - \Delta a_{i-1})^2 + \\ \beta_a(l_i + \Delta l_i - l_{i-1} - \Delta l_{i-1})^2 + \beta_l'(l_i + \Delta l_i - l_{i,j-1})^2\} \end{gathered} \tag{3.3}$$

where α, β_a, and β_l' are regularization coefficients set by the user. These coefficients affect how close the axial displacements are in relation to each other, the lateral displacements proximity in relation to the axial direction and the lateral direction respectively. Δa and Δl are the subpixel displacements calculated by the 2D minimization. A Taylor series expansion is written around the image data term, the first term in the summation. The Taylor series expansion is used to calculate the gradient at a given point, which is essential for verifying if the function is moving towards minimization appropriately. Since this expansion is done on non-grid points some interpolation of the values of Δa and Δl are required. Inverse gradient estimation may be employed to interpolate off-grid values in the second image, using initial grid positions from the first image without requiring interpolation of the image gradients. This allows for image gradients to be calculated on grid positions in Image 1 without the need for the gradient estimate. A visual representation of this can be seen in Figure 22.

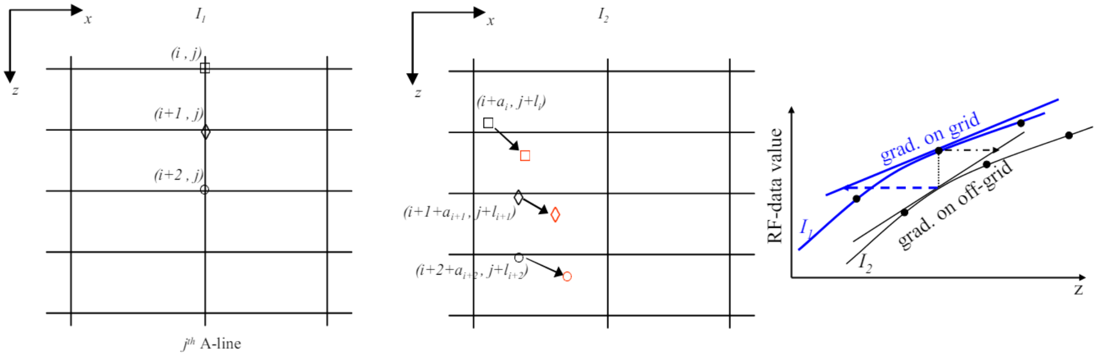

Figure 22: The inverse gradient estimation approach used by AM2D to calculate off grid points for the Cartesian system [39]. This approach eliminates the need for interpolation of the off-grid points.

AM2D accounts for the attenuation, biasing, time gain, error measurement, and weighted regularization based on residuals and image displacement gradient. AM2D applies the minimized displacements and these parameters to the image data to calculate the displacement field. This governing equation can be seen in Equation 3.4,

$$(WI_1'^2 + \boldsymbol{Z}D_1 + \boldsymbol{Z}D_2)\Delta d = WI_1'e - \boldsymbol{Z}D_1 d + s \qquad (3.4)$$

where W is the weight constant, I_1' is the pre compression image, **Z** is the attenuation compensation matrix, D_1 is the regularization coefficient matrix for the axial direction, D_2 the matrix for the lateral regularization coefficient, Δd are the unknown displacements, e is the error, d is the current displacement estimate, and S is the bias term [39].

This algorithm assumes a linear transducer such that all acquired images are found in a Cartesian system with the scan lines running perpendicular to one another. This is the case with most linear transducer acquisitions; however, this algorithm cannot accurately compute the displacements for a transducer of curvilinear nature such as those that are used for TRUS procedures.

3.2 Alterations to AM2D for Polar System Imaging

The grid calculation and Taylor series expansion must be altered to consider polar expansion. The altered Taylor series expansions are implemented in the same structure as the original AM2D to recover performance when computing the initial estimates for the displacement field. Equation 3.3 is altered such that the coordinate system is polar, and the coordinate derivatives are taken in the polar system resulting in Equation 3.5. Taking the Taylor series expansion around the data term of Equation 3.5 yields Equation 3.6 with the optimal displacement values appearing at the points where the partial derivatives of the cost equation are equal to 0. The final equation used to calculate pixel displacements is constructed in the same way as in Equation 3.4, except estimations occur on a polar grid,

$$\begin{gathered} C_j(\Delta r_1, \ldots, \Delta r_m, \Delta\theta_1, \ldots, \Delta\theta_m) = \\ \sum_{i=1}^{m} \{[I_1(i,j) - I_2(i + r_i + \Delta r_i, j + \theta_i + \Delta\theta_i)]^2 + \\ \alpha(r_i + \Delta r_i - r_{i-1} - \Delta r_{i-1})^2 + \\ \beta_r(\theta_i + \Delta\theta_i - \theta_{i-1} - \Delta\theta_{i-1})^2 + \beta'_\theta(\theta_i + \Delta\theta_i - \theta_{i,j-1})^2\} \end{gathered} \tag{3.5}$$

$$I_2(i + r_i + \Delta r_i, j + \theta_i + \Delta\theta_i) \approx I_2(i + r_i, j + \theta_i) + \Delta r_i I'_{2,r} + \Delta\theta_i I'_{2,\theta} \tag{3.6}$$

where r is the radial displacement, θ is the angular displacement, I is the image data matrices for the first and second images, and α, β_r, and β'_θ, are the user defined regularization parameters. The expansion around the data term allows for the inverse gradient estimation to be used in the polar system. A visualization of this is seen in Figure 23.

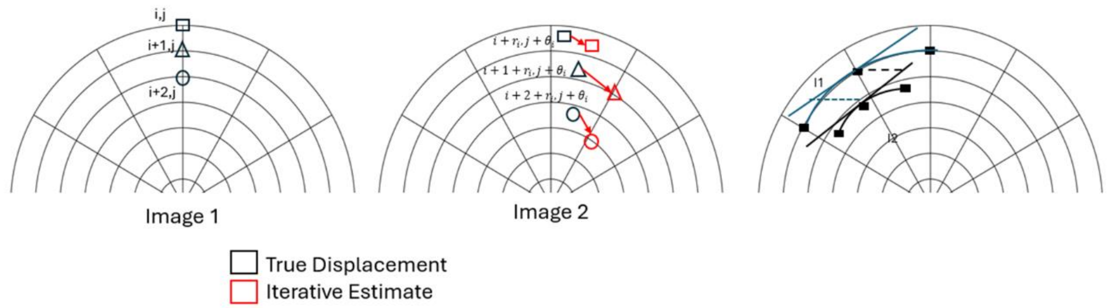

Figure 23: Grid displacement calculation through polar tangent gradient estimation. This also utilizes a gradient estimation method to avoid interpolation for the off-grid points.

The first image in Figure 23 shows the initial location of the pixels. The second image shows the true and estimated pixel displacements. The estimated values can be determined through the inverse gradient estimation and Equation 3.4. The estimation of the gradient off the grid for the pixel points is equivalent to the on-grid points, eliminating the need to interpolate the gradient values for the off-grid points in the polar system. Once the polar formulation of Equation 3.4 is determined, it is implemented in the existing C++ architecture to achieve the same speed in calculation and displacement accuracy as the original AM2D algorithm.

3.3 Results and Discussion

After implementing the changes to AM2D in the polar system, the *in-silico* data set can be used to measure the accuracy of the displacement estimations made by AM2D. For this purpose, the hyperparameters α, β_r, and β'_θ must be set for a usable output displacement estimation. A search algorithm was used to set these parameters, where an initial estimate of the parameters is used to compute the displacement field. From this the MSE and CC scores are computed against the FEA data and stored as the best if the MSE or CC scores are better than the current best score. The parameters are then increased, and the process repeats itself. This is the same method used to evaluate the output quality using the method seen in Appendix B2 and update the parameters as appropriate and the code for the algorithm is found in Appendix B3. The algorithm utilizes a patience count to limit the number of iterations that the algorithm will search and a learning rate to limit the change in parameter value such that a vanishing gradient or overshoot of the optimal value does not occur. It was found that during testing, the MSE score was the best indicator in determining if the angular regularization value was improving, and the combined score of MSE and correlation was best at determining radial regularization. The optimized values of α, β_r, and β'_θ used are 41.1448, 9.7017, and 0.097 for the *in-silico* data and for the tissue-mimicking phantom data 14.421, 9.7017, and 0.097. In addition, Table 11 shows the remaining AM2D parameters, such as the attenuation coefficient and dynamic programming coefficient.

Table 11: Parameters used in the AM2D algorithm to determine initial tissue displacements

Parameter	***In Silico***	**Phantom**
IRF (variation range of radial displacement)	[-100 0]	[-100 0]
IA (variation range of angular displacement)	[-4 4]	[-6 6]
Middle A-line number	108	108
$\boldsymbol{\alpha_{DP}}$ **(Dynamic programming regularization)**	0.15	0.15
T (Threshold for iterated reweighted least squares)	.2	.2
$\boldsymbol{A_T}$ **(Attenuation coefficient)**	0.63 dB/cm*MHz	1.6 dB/cm*MHz
$\boldsymbol{f_0}$ **(Center frequency)**	7 MHz	7 MHz
$\boldsymbol{f_s}$ **(Sampling Frequency)**	40 MHz	20 MHz

The IRF and IA values are used to constrain the range in which the displacements are expected to be found. For both the simulated and tissue-mimicking phantom data, a range of -100 to 0 was used to align with the expected pixel displacements range. The displacement is purely compressive; hence the minimum possible displacement value is a negative and the maximum is zero. The IA value varied from negative to positive due to the uncertainty of whether lateral displacements would happen in just one direction. The delta between the simulated and phantom datasets for the IA is attributed to the expectation that the tissue-mimicking phantom dataset will showcase greater displacement values, given that the 1mm probe movement in the simulated dataset is less than the probe movement executed during the phantom study. The middle line number is the center A-line that is used in the first line calculated during the AM2D algorithm. The DP regularization coefficient is the same for both the simulated and phantom data sets as the regularization between integer samples is similar. The T value for both data sets was 0.2 as the outlier data used in the iterative reweighted least squares method is expected to remain the same between data sets. The attenuation coefficient for the *in-silico* data is 0.63 dB/cm*MHz which is used for lipid tissue, and 1.6 dB/cm*MHz which is the attenuation coefficient for gelatin found in Table 7. Finally, the center and sampling frequencies are reflective of the frequencies used to acquire the RF data sets. From these parameters and the AM2D algorithm, results can be generated representing the *in silico* and tissue-mimicking phantom data sets. The *in silico* results are shown below in Figure 24.

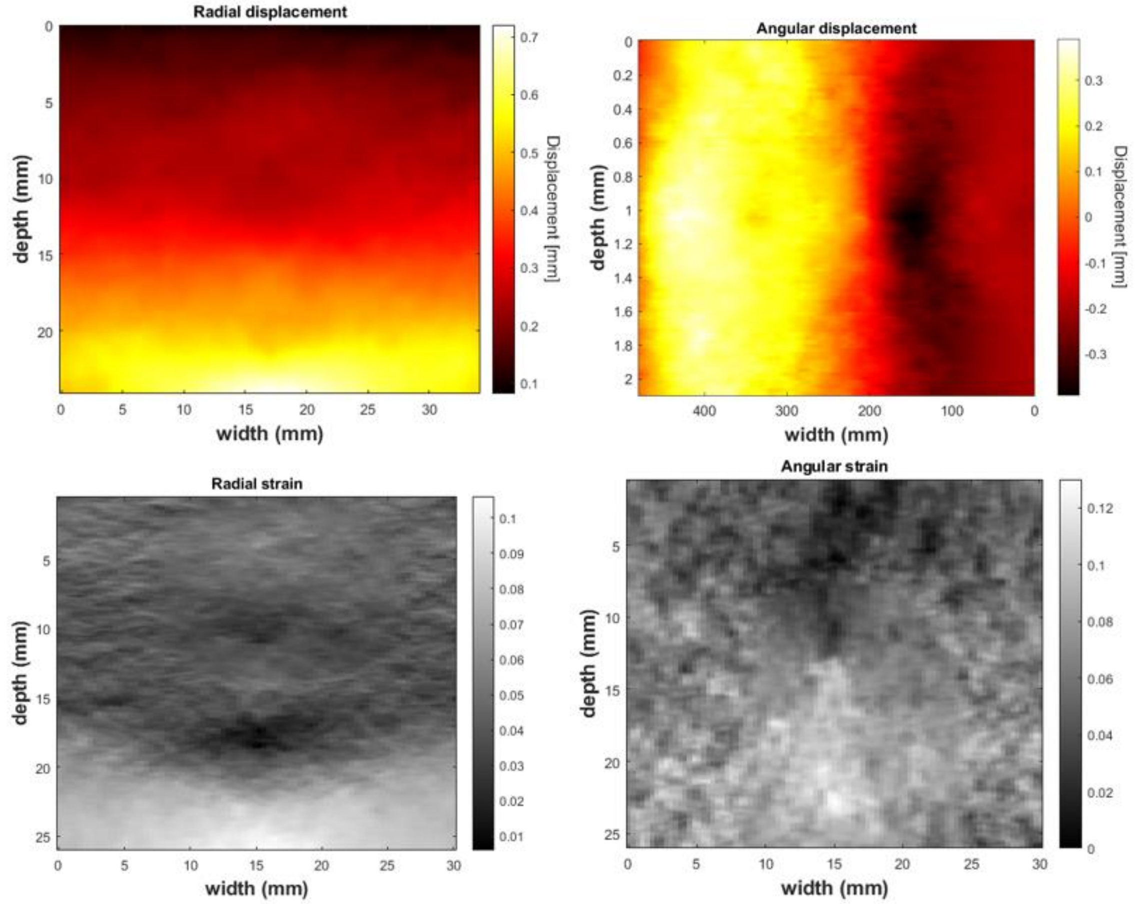

Figure 24: In silico Results from a 256-scan line transducer, with displacements generated from a FEA solver.

The *in silico* results indicate that the output can be generated in 0.072 seconds, allowing an output frequency of 13 frames per second. This speed result was calculated on a machine with an Intel Core i7 9th generation, 8 GB Ram and an NVIDIA GeForce RTX 2060 graphics card. Upon visual evaluation of the B-Mode scans, it is evident that both the pre- and post-compression images are highly correlated, with the prostate capsule and background material visible, and minimal out of plane imaging occurring. It is observed that the highest displacements occur around the peripheral zone of the prostate capsule for the radial displacements, and along the central scan line for the angular directions. This result is consistent with what is seen in the FEA outputs. The finite difference method for strain calculation reveals that the prostate capsule is reasonably well visualized for the radial direction, showing large amounts of compressive strain in the lower region. However, while the visualization of the of the angular strain still shows the prostate capsule geometry, it is hindered by substantial noise inside and surrounding the capsule. A comparison of the displacements and strains with the FEA output and the generation of the MSE value for the normalized images yields the results presented in Table 12.

Table 12:MSE Values for the In Silico data sets.

	MSE VALUE
RADIAL DISPLACEMENT	888.59
RADIAL STRAIN	918.42
ANGULAR DISPLACEMENT	1632.30
ANGULAR STRAIN	1690.42

From Table 12, the MSE values for both the radial displacement and strain are lower than the angular direction displacements and strains. This is expected from AM2D as only sub pixel displacements are calculated for the radial direction due to computation time constraints [40]. This limitation results in displacements that are only integer values from the angular direction, which is also carried over to the reconstruction of the strain image.

The cross-correlation values between the ground truth FEA data and the outputs of AM2D are calculated using Equation 1.20. These results are organized in Table 13. It is seen that the Cross Correlation scores for the radial directions displacement and strains are higher than those for the angular directions. The difference in cross correlation scores is due to the additional sub-pixel estimation in the radial direction that AM2D computes using Analytic Minimization. The magnitude of the values shows there is a positive correlation between the images being compared and that the produced images fit well with the ground truth data. The lower correlation scores for the Angular direction results are largely due to the noise in the system, lowering the overall SNR and CNR values. The removal of this noise and refining the images will improve the MSE and correlation scores for the radial, and angular directions.

Table 13:Cross Correlation scores for the In Silico data set.

	CROSS CORRELATION SCORE
RADIAL DISPLACEMENT	0.83
RADIAL STRAIN	0.84
ANGULAR DISPLACEMENT	0.68
ANGULAR STRAIN	0.65

A pair of compression frames identified using the data quality analysis algorithm outlined in Chapter 2.6 were used to apply the alterations made to AM2D to best tested on the TMP data. The visualized displacements and strains for the phantom data set are shown in Figure 25.

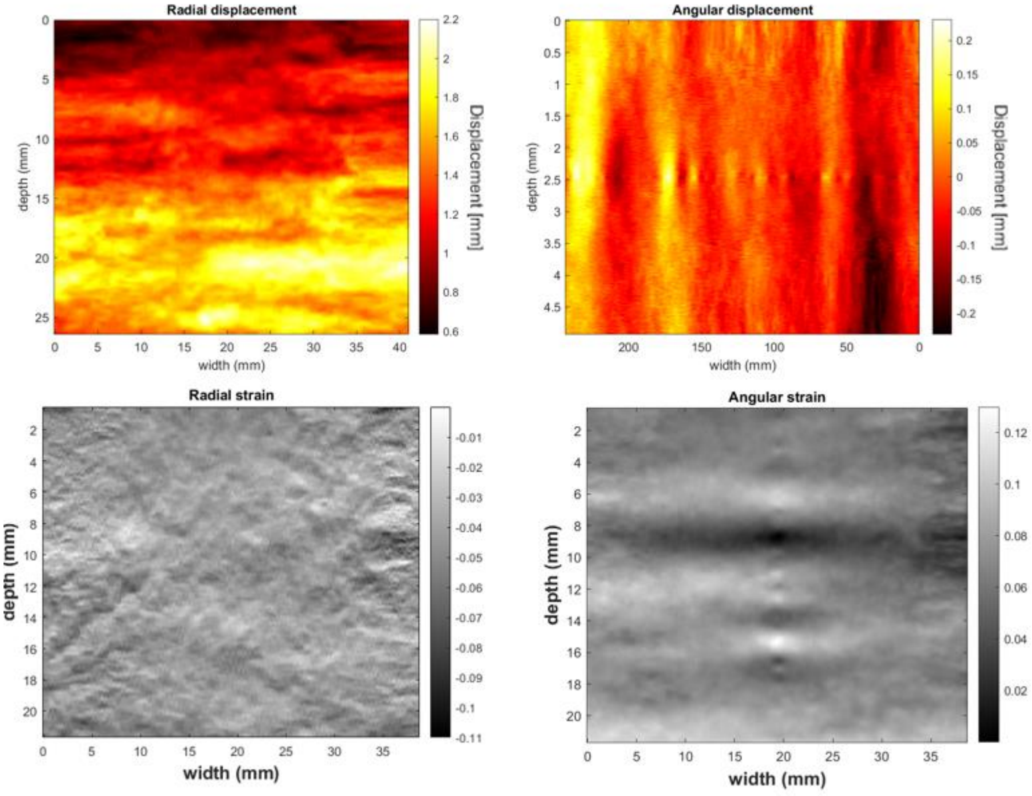

Figure 25:The Displacements and Strains calculated from the phantom data set processed by the AM2D algorithm.

The strains are calculated using a finite difference method, where the difference in displacement is taken for each point and divided by the depth of the image to get a strain measurement in mm/mm. The finite difference algorithm used can be seen in Appendix B4 where the strain is calculated for each row for the angular direction and each column in the radial direction. As the phantom data does not have a known ground truth, a visual determination of the quality of the displacements and strains is required. The data visualization of the displacements shows that the radial displacement is high close to the transducer at the bottom of the image and trend towards 0, which is consistent with the known behaviour of the displaced tissue. There are some high spots in the upper regions of the image, which can be a result from out of plane movement of the tissue creating some discontinuities in the AM2D calculations. The angular displacement displaces away from the central point of the image as expected with the direction of the movement of the tissue being consistent with what is expected and seen with both the FEA and In Silico data, lending further support for the quality of the displacements calculated. The radial strain somewhat shows the prostate capsule in the center of the image, with a slight change in the amount of noise present towards the center of the image, however the strain image quality can be much improved. The angular strain, as expected with AM2D is not as accurate, and the prostate capsule is hard to distinguish. The strain refinement algorithm of STREAL can be used in strain imaging to further refine the input displacement data into better images.

3.4 Tissue Mechanics enforcement of STREAL

After processing the initial displacement calculations using AM2D, it is possible to further refine these results by enforcing tissue mechanics onto the initial displacements. Originally developed by Kheirkhah *et al.* [43], the mechanics of incompressibility, compatibility, and known boundary conditions allow for improvements in the direction perpendicular to the scan line. In the Cartesian case this is the lateral direction, or when referring to the polar system, the angular direction. These enforcements onto the initial displacements and strain calculations can be computed rapidly, and just like AM2D allow for the algorithm to be computed in real time.

Once the initial displacement estimations have been estimated by AM2D, it is possible to refine these results by enforcing tissue mechanics onto the results. The first step in this enforcement is to apply a second order derivative-based smoothing to the displacement fields using a convolutional Laplacian filter. This filter, when convolved with the displacement data, suppresses sudden intensity transitions. Points can then be smoothed with Equation 3.7.

$$U_{new} = (I + \lambda^2 L^T L)^{-1} U_m \tag{3.7}$$

Where U_{new}, and U_m are the new and initial displacements, I is the identity matrix, L is a matrix with finite difference coefficients of the Laplacian operator and, λ is the regularization weight coefficient, which can be found through an L-curve method such that the bend in the graph of $||U_{new} - U_m||$ and $||LU||$ is at a knee point in the curve [43].

Following regularization tissue incompressibility is enforced on the displacement field. To enforce this mathematically, the divergence of the displacement field is set to zero, and since US data does not normally provide out of plane data, plane strain is assumed, leading to Equation 3.8.

$$\frac{\partial U_x}{\partial x} + \frac{\partial U_y}{\partial y} = 0 \tag{3.8}$$

Where U is the displacement at the point of measure. However, plane strain cannot be assumed for non-homogenous tissue regions, such as the breast or prostate [43]. To remove this assumption and provide more accurate results, the Boussinesq model is applied to generate three equations that will describe the stress in the x, y, and z directions respectively. These calculated stress values can then be used to calculate the strains in the x and y directions, and are seen in Equations 3.9, 3.10 and 3.11. Once these strains are determined the ratio of the out plane to axial strains, k, can be calculated, creating the modified compressibility Equation 3.12,

$$\begin{aligned}\sigma_x = \frac{P}{2\pi}\Bigg\{&\frac{3(y_0 - y)(x_0 - x)^2}{r^5} \\ &- (1 - 2v)\left[\frac{(x_0 - x)^2 - (z_0 - z)^2}{r[r^2 - (y_0 - y)^2](r + (y_0 - y)} \right. \\ &\left. - \frac{(z_0 - z)^2 (y_0 - y)}{r^3 (r^2 - (y_0 - y)^2)}\right]\Bigg\}\end{aligned} \tag{3.9}$$

$$\sigma_y = \frac{3P}{2\pi}\frac{(y_0 - y)^3}{r^5} \tag{3.10}$$

$$\sigma_x = \frac{P}{2\pi}\left\{\frac{3(y_0 - y)(z_0 - z)^2}{r^5} - (1 - 2v)\left[\frac{(z_0 - z)^2 - (x_0 - x)^2}{r[r^2 - (y_0 - y)^2](r + (y_0 - y)} - \frac{(x_0 - x)^2(y_0 - y)}{r^3(r^2 - (y_0 - y)^2)}\right]\right\} \tag{3.11}$$

$$k = \frac{\partial U_z}{\partial Z} + (k + 1)\frac{\partial U_y}{\partial Y} \tag{3.12}$$

where σ is the stress, P is the pressure, r is the distance from the point of pressure to the measurement point, v is the Poisson's ratio, x, y, and z are the Cartesian directions. Finally, U is the displacement measure, and k is the incompressibility ratio. This process is repeated for each point in the field of view, such that a k value is found for every possible pixel position from the displacement data to form a K-matrix [43].

The final step implemented in STREAL is to enforce the strain compatibility. Equation 3.13 shows the compatibility equation in terms of its tensor components.

$$\frac{\partial^2 \varepsilon_{xx}}{\partial y^2} + \frac{\partial^2 \varepsilon_{yy}}{\partial x^2} - 2\frac{\partial^2 \varepsilon_{xy}}{\partial x \partial y} = 0 \tag{3.13}$$

Equation 3.13 was utilized to create a numerical solution for each 4-node element in the computational grid [43]. The complete outline of this process can be visualized in Figure 26.

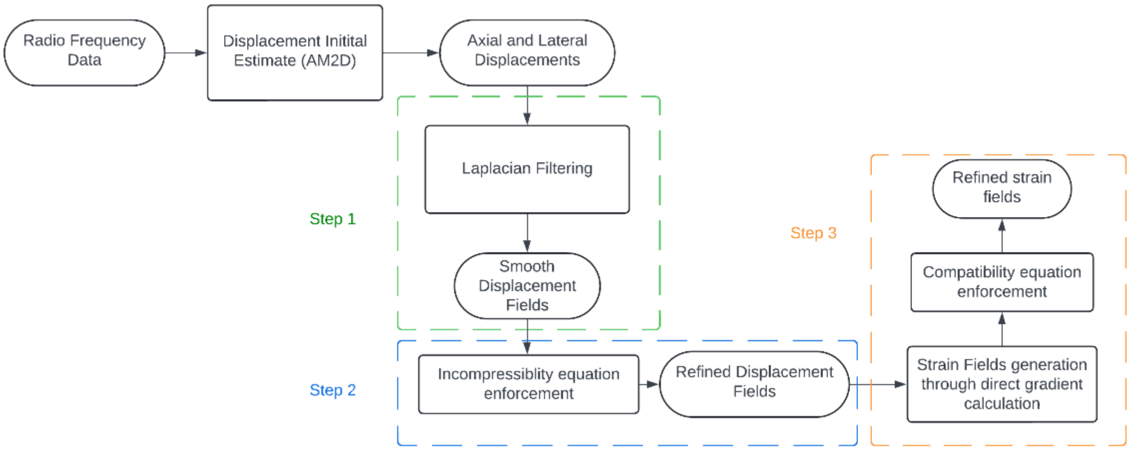

Figure 26: Process flow of the Strain Refinement Algorithm (STREAL). The initial estimates from the RF data are filtered by a Laplacian operation, before incompressibility and compatibility are enforced on the results.

This method, while accurate, can suffer from longer computational times. By using convolution and the above approach, a faster implementation can be achieved. Applying Laplacian and finite difference kernels to acquire the strains, incompatibility, and smoothing, STREAL can be quickened to allow real time processing. Additionally, the *K*-matrix and Lamé parameters can be pre-computed for the image processing network, so that the weights do not have to be regenerated for each new patient. Instead, the system has been tuned using the input displacement data to determine the optimal values for the weighting parameters.

To implement this algorithm for polar data, alterations must be made to the system, including the *K*-matrix formulation, gradient calculations computed in the convolutional method, and the image formatting. As the discovery that these alterations would be required occurred late in the development timeline, it was determined that the Cartesian system displacements would be used by transforming the polar coordinate displacement data, into Cartesian form using Equation 3.14 and 3.15,

$$U_x = U_r \cos\theta - U_\theta \sin\theta \tag{3.14}$$

$$U_y = U_r \sin\theta + U_\theta \cos\theta \tag{3.15}$$

Where U is the displacement in the specified direction, and θ is the angle between the vertical axis and the point of measure. While maintaining the use of STREAL is important in providing results for further reconstruction algorithm accuracy, this approach increases system processing due to the additional calculations.

3.5 Potential STREAL polar alterations

If given more time to develop STREAL in an entirely polar system, the *K*-matrix formulation from Equation 3.8 and the stress calculations derived from the Boussinesq model must be altered to the polar coordinate system. The x and y coordinates from the Cartesian derived stress equations become θ and r directions respectively. Y remains the out of plane direction in a cylindrical coordinate system. Seen in Equations 3.16 and 3.17 are the polar forms of the stress calculations which utilize a change of variable to alter the existing Cartesian system equations [65],

$$\sigma_r = \sigma_x \cos^2\theta + \sigma_y \sin^2\theta + \tau_{xy} \sin\theta \cos\theta \tag{3.16}$$

$$\sigma_\theta = \sigma_x \sin^2\theta + \sigma_y \cos^2\theta + \tau_{xy} \sin\theta \cos\theta \tag{3.17}$$

where σ is the stress in a specified direction, τ_{xy} is the shear stress, and θ is the angle between the central axis and the stress measurement point. It is possible to develop a *K*-matrix in the polar system that describes the out of plane behaviors of the material at every point in the matrices. A visualization of the generated polar image is seen in Figure 27. Where the image shows a TRUS probe at the bottom of the image, and the ratio between the out of plane and axial stresses.

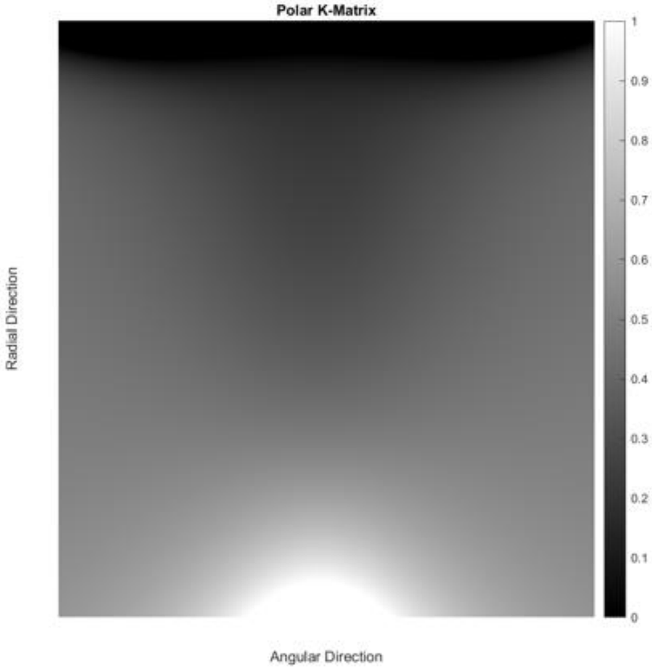

Figure 27: K-Matrix visualization in the polar form generated using hertzian contact mechanics and integration of the pressure equations in the polar form.

In addition to the alterations to the *K*-matrix, there is evidence behind the convolutional kernels used in STREAL contributing to erroneous operation within the algorithm. According to Kim *et al*., there exist differences in the outputs when convolving images in the polar system and in the Cartesian system, and the use of polar images with kernels developed for use with Cartesian images may produce unexpected or erroneous results [66]. This is due to inconsistencies in kernel weights in the polar system, as the divergence in spacing between the radial rows of data is unequally spaced as the kernel travels along the image. An example of this is seen in Figure 28.

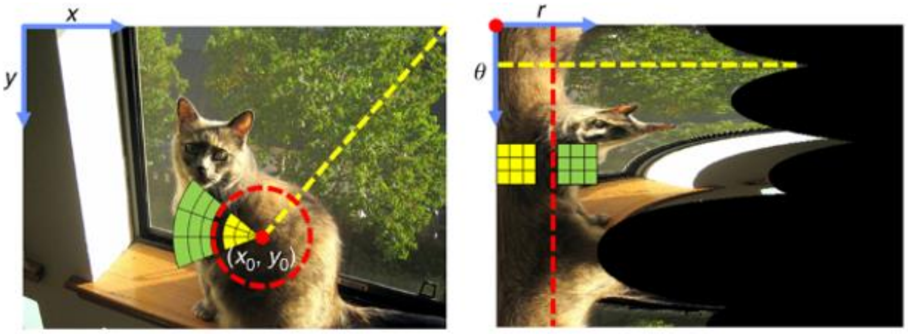

Figure 28: Image convolution of a miss matched polar kernel with Cartesian image [66]. This shows that the weighting of the kernel must change due to the change in the coordinate system.

Where the image on the left shows that the polar kernel is being utilized on a Cartesian image with inconsistency in kernel weight as it progresses through the image. The right image shows the opposite scenario, where the kernel is unfit to capture the polar data effectively through its equal weighing, even as the image becomes inconsistently spaced in the radial direction. This same principle can be applied to the polar data captured by the TRUS probe, where convolution of this data in the polar form with a Cartesian image kernel will result in incorrect weighting and processing of the input data.

To remedy this a polar version of the Laplacian and finite difference kernels utilized in the STREAL functionality would have to be re-worked into appropriate polar versions of the kernels. This would involve computing the numerical solution to the Laplacian of Gaussian and determining the appropriate size of filter to use in STREAL with the input data. Additionally, the finite difference kernel needs to be altered to consider the changing angle of the radial lines for each successive RF row when computing the finite difference along lateral scan lines.

3.6 Results and Comparison to AM2D Polar

To show the improvements of STREAL the polar estimates from AM2D were converted to Cartesian data displacements, and the output results were compared to those of AM2D, for both the *in silico* and TMP data sets. The STREAL output from the simulated data set can be seen in Figure 29, and the output results from the TMP data set are seen in Figure 30.

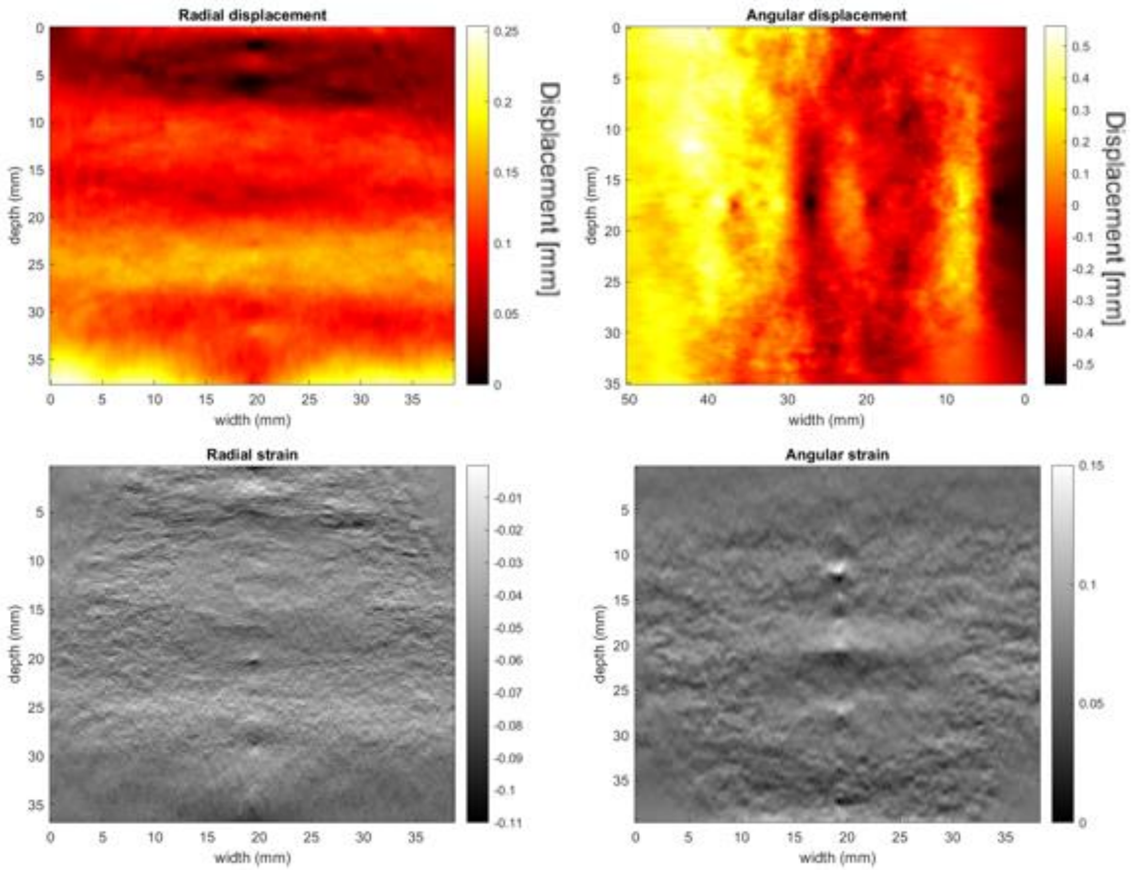

Figure 29: In silico results from the refinement algorithm STREAL. Showing the radial and angular direction displacements and strains.

From the initial B-Mode images, the prostate capsule is at the center of the image, with the background material present on both the pre- and post-compression images. Looking at the results in the radial direction, the improvement in clarity for the displacements experience by the prostate capsule and background material is minimally improved over AM2D. Improvements in AM2D are largely attributed to AM2D providing good sub-pixel estimates for the radial direction. However, the strain image is greatly improved, especially for the tissue outside of the prostate capsule where much of the noise is removed and the image is smoothed from the Laplacian filtering and strain compatibility enforcement. The angular direction displacements and strain are both improved in comparison to the outputs from AM2D. The strain image from AM2D showed mostly noise in the image, whereas the refined image is smoothed, and the prostate capsule can begin to be seen at the center of the image.

With the visual results displayed, it is also possible to determine the MSE value between the computed values and the ground truth values from the FEA model. The computed MSE, as well as the % change in error between the AM2D MSE results is seen in Table 14.

Table 14: The MSE values from AM2D and STREAL, produced from the output displacements and strains.

AM2D MSE		STREAL MSE		% Improvement
Radial Displacement	888.59	Radial Displacement	843.55	5.07
Radial Strain	918.42	Radial Strain	543.33	40.84
Angular Displacement	1632.30	Angular Displacement	756.02	53.68
Angular Strain	1690.55	Angular Strain	691.27	59.11

From Table 14 both the displacement in the radial and angular direction has small differences, with the radial direction being slightly better than the AM2D results, and the angular displacement improving by about 40%. The small change in radial displacement is expected, as AM2D focuses primarily on estimating and improving the radial direction through its DP and minimization process as outlined in Chapter 3.2. Enhancements in displacements along the lateral direction achieved with STREAL can be attributed to the application of tissue mechanics that permit finer estimation of sub-pixel displacement and promote smoother results. This creates a smoother image for the displacement, and the strain. The largest improvement is the angular strain, where the improvement gained is just over 59%. This improvement in both the radial and angular directions is important for using the resulting strain calculation in other algorithms, such as iterative reconstructive algorithms which require a strain map for stiffness reconstruction. Overall STREAL can maintain, or greatly improve the results provided by AM2D, and can provide high quality strain images for use as a diagnostic tool or in reconstructive algorithms which provide further insight about prostate tissue health. Additionally, the Cross Correlation scores are calculated between the STREAL outputs and the ground truth FEA model to determine the improvement over the AM2D outputs and are shown in Table 15.

Table 15: Cross Correlation scores from the in silico Data for AM2D and STREAL.

AM2D		STREAL		% improvement
Radial Displacement	0.83	**Radial Displacement**	0.87	4.82
Radial Strain	0.84	**Radial Strain**	0.89	5.95
Angular Displacement	0.68	**Angular Displacement**	0.78	14.71
Angular Strain	0.65	**Angular Strain**	0.80	23.08

The improvement for each of the radial and angular components is seen in the right most column of Table 15. Angular displacements and strain have the most improvement with STREAL while the radial direction has only minor improvement over the AM2D results. This is expected as STREAL aims to impose the mechanical properties of the tissue to better smooth and calculate the strains. AM2D does this well for the radial direction, applying the subsample analytic minimization method, but is weaker in the angular direction as AM2D does not compute the angular directions subsample displacements to reduce computational time. The improvement in the cross correlation shows that the outputs from STREAL are highly correlated to the ground truth found in the FEA model and provide a good indication of the tissue displacements and strains within the prostate.

In Figure 30, which illustrates results of the TMP case, the radial and angular displacements have been greatly smoothed when compared to the AM2D outputs due to the incompressibility and Laplacian smoothing. The displacement fields are also used in tissue strain measure calculation, as the strain is a finite difference of the displacements calculated through convolution with a difference kernel. Looking at the strain images, some of the information around the edges of the image is lost during the calculation of the initial estimate displacement in AM2D when the outer lines on either side of the image are skipped to down sample the data. In addition, data is lost for each RF data row as calculating the edge values using convolution without padding will result in a smaller output matrix. This loss of information is acceptable for this case as the area of interest is usually centered during data collection. The B-Mode image is displayed during data acquisition to enable the correct placement of the transducer. With this loss of information, the prostate capsule

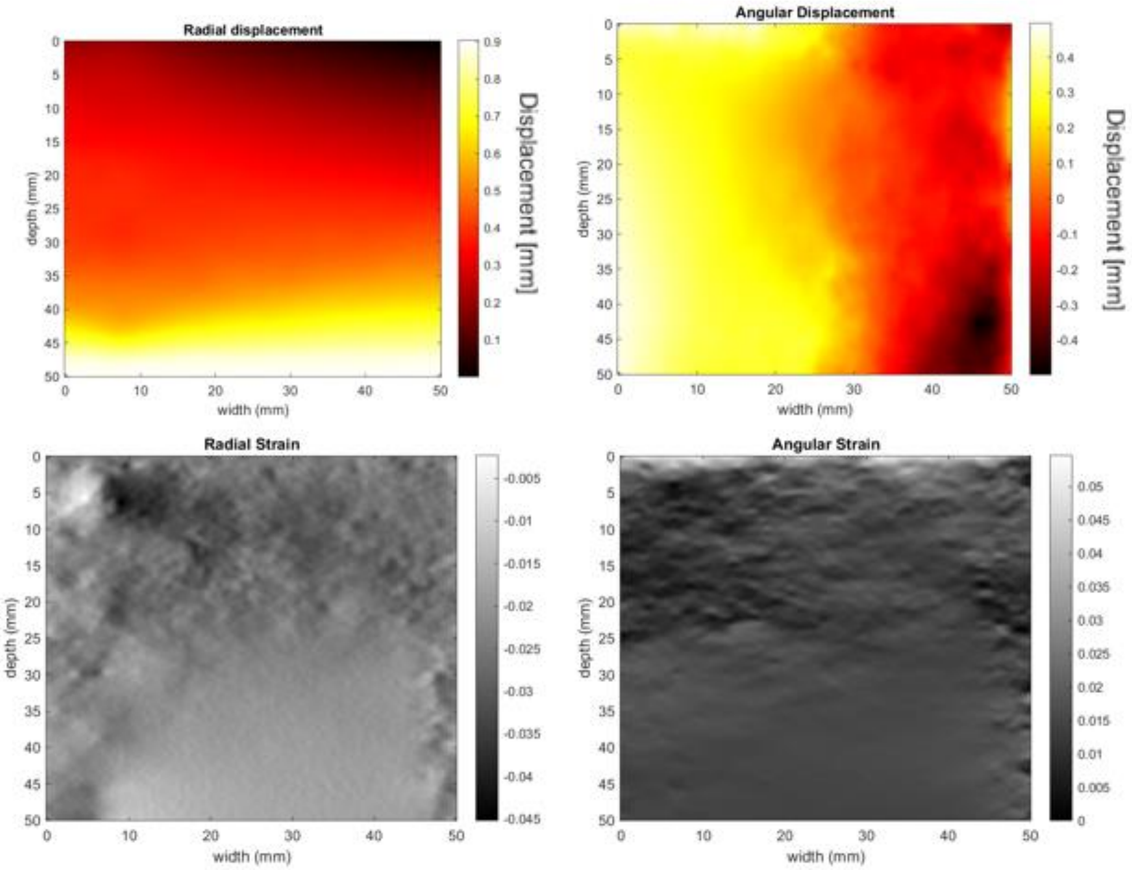

Figure 30: TMP outputs from STREAL refinement showing the radial displacement and strain, and angular direction displacement and strain.

moves closer to the top of the image, as seen in the radial strain reconstruction, where the dark patch can be seen as the lower strain foam inclusion, compressed less than the gelatin background. Looking at the angular strain the image is smooth and is no longer noisy as seen in the AM2D output in Chapter 3.3. This increased smoothness is desired, as this output strain image is used to iteratively reconstruct other material parameters, that are outlined in the following chapter, where any errors within the strain image can lead to erroneous results being propagated throughout the reconstructed images.

To further test the capabilities of AM2D and STREAL a clinical study should be performed, where data is obtained from patients with known carcinoma. Clinical studies will allow the system to be tested on cancer tissue specific material properties and additional artifacting resulting from clinician or patient movement during the procedure. Testing the robustness of the system on the real, imperfect data will allow for a greater understanding of the capabilities of AM2D’s estimations, and STREAL’s ability to refine these results in usable images and data sets.

Chapter 4

4 Poisson’s Ratio Image Reconstruction

Upon obtaining the displacement and strain measurements from the USE pairing, it is possible to reconstruct the tissue's properties, including strain and stiffness. An iterative approach using FEA is used to compute the tissue properties allowing for the stiffness to be estimated for each pixel in the output image. This method is universally accepted and used in a variety of USE methods; however, it can be improved by calculating additional material properties such as Poisson’s ratio. This reconstruction method utilizes the same iterative process in a FEA solver to converge to a solution for the Poisson’s ratio. The Poisson’s ratio calculation allows the Shear Modulus to be determined which provides imaging of the tissue with a complete view of the stiffness and incompressibility. Shifts in Poisson’s ratio and Shear Modulus are two indicators of abnormal tissue within the prostate.

4.1 Stiffness, Poisson’s Ratio and Shear Modulus Imaging

To further enhance the image output, both the Poisson’s ratio and the shear modulus are determined from the stiffness calculation. The Poisson’s ratio is described as the ratio between the transverse strain and the lateral strain, as seen in Equation 4.1.

$$\nu = -\frac{\varepsilon_{trans}}{\varepsilon_{axial}} \tag{4.1}$$

Using the 2-dimenesional Hooke’s law, the directional components can be calculated using the stresses, strains and Young’s modulus of the material as shown in Equations 4.2 and 4.3.

$$\nu_x = \frac{\sigma_z - \varepsilon_z * E}{\sigma_x} \tag{4.2}$$

$$\nu_z = \frac{\sigma_x - \varepsilon_x * E}{\sigma_z} \tag{4.3}$$

Since the tissue is assumed to be isotropic and linear elastic, the above two υ values can be leveraged to obtain a reliable Poisson’s ratio estimate. In Equations 4.2 and 4.3, the stresses, σ_z and σ_x, and Young’s Modulus, E, are iteratively calculated and confirmed against the known strains as an error measurement. Iterative stiffness reconstructions are common in elastography and have been developed with different algorithms in place [45] [46] [55]. Once Equation 4.2 and 4.3 converge to an acceptable result, the Poisson's ratio image reconstruction can be plotted and additional parameters such as the shear modulus calculated. The equation to calculate shear modulus is included as Equation 4.4,

$$G = \frac{E}{2(1+\nu)} \tag{4.4}$$

where G is the shear modulus, E is the Young's Modulus, and ν is Poisson's ratio. The shear modulus is used to describe a material's ability to resist motion in the shear plane, and for tissue mechanics of organs this can provide additional information pertaining to the tissue that may be used as extra pathological signature. In other words, Poisson's ratio and shear modulus provide additional information on the tissue mechanics present in the image data and provides another option in diagnosing malignant tissue within the prostate, or other tissues that are imaged using ultrasound.

An iterative FEA process can be used to calculate more tissue mechanic properties. Using the strains and displacements as a ground truth for the iterative process, the stress and Poisson's ratio are calculated in the tissue. If the estimated strain is close to the ground truth strain from STREAL, then the system has converged, and the process is terminated. A flow chart of this exact process can be seen in Figure 31.

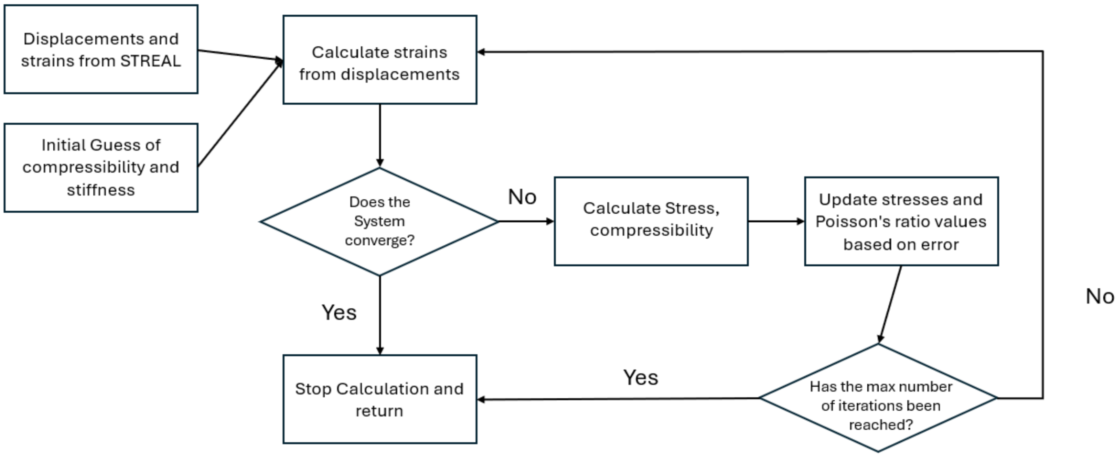

Figure 31: Flow chart of the FEA Poisson's ratio and Stiffness reconstruction algorithm. This shows the iterative nature of the algorithm where the convergence of the system is dependent on the input strains and reconstructed values.

4.2 *In Silico* Poisson's Ratio Reconstruction

To conduct the initial investigation into the Poisson's ratio reconstruction, three *in silico* phantoms were used to ensure that the displacements were known prior to calculating material properties such as the strains or stresses. The first phantom is a background material with a single large central inclusion, which is referred to as the benign data set. The second phantom is a bifocal data set with three inclusions inside a background material. The displacements for both phantoms are defined for each point within the phantom to ensure that the displacement field is continuous and realistic. These two data sets are visualized in in Figure 32. The final data set is the Rivaz Phantom, which is visualized in Figure 35.

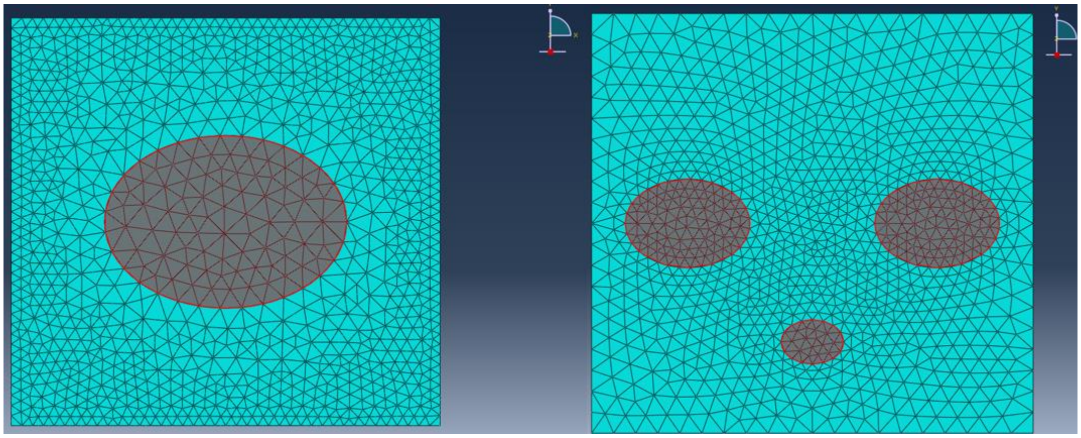

Figure 32: Visualizations of the meshed FE models used for the Poisson's ratio reconstruction algorithm. The Benign inclusion data set(left) has a single large benign tumor that is highlighted in the image. The Trifocal Data set has three inclusions, the two larger inclusions are benign and the smaller central is malignant.

Where each white point is a coordinate for which a corresponding displacement has been determined for both the lateral and axial direction. From the benign data set the strains in the axial, lateral, and shear directions are calculated, and used to iteratively calculate the Poisson's ratio and stresses within the phantom. The results from the benign data set are seen in Figure 33.

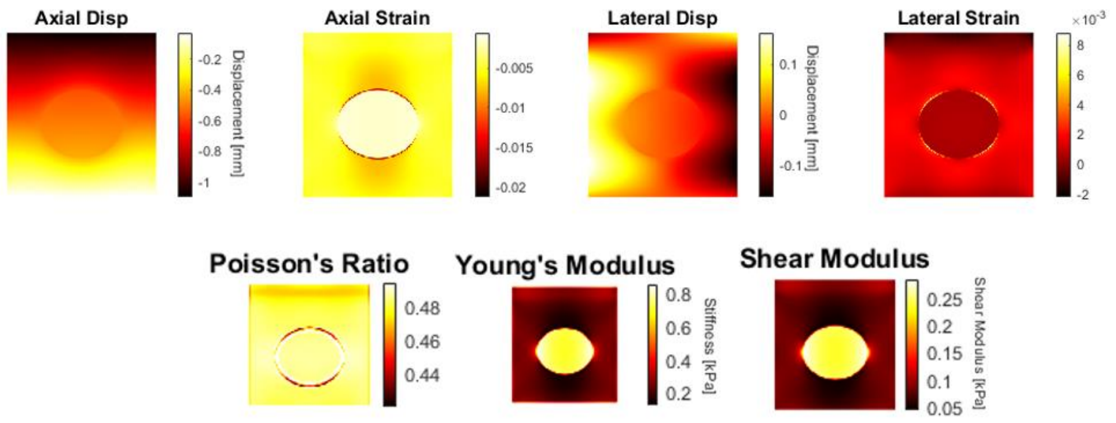

Figure 33: Benign Data results, showing the Displacement and strains from AM2D and STREAL, as well as the reconstructed Poisson's ratio, Stiffness and Shear modulus values for the phantom. The central inclusion is easily seen in the reconstructed images.

The Axial and Lateral displacements of the phantom are known prior to the algorithm in this phantom case and are seen in Figure 33. The strain in both the axial and lateral direction are calculated using a finite difference of the displacements in the relevant direction. These strains are then used as confirmation for the iterative FEA solution of the calculated stiffness and Poisson's ratio. The Young's modulus value ranges from 0.2MPa in the background to 0.8MPa inside the singular inclusion. The Poisson's ratio from the reconstructed values, shows a ring of lower compressibility around the central inclusion. This ring occurs in the same region as the larger compressive strain seen in the Axial strain image. This correlation is described by the relationship between strain and Poisson's ratio where the higher the axial strain in a region of the material, the lower the value of Poisson's ratio. By combining the Young's modulus and Poisson's ratio in Equation 4.4, the shear modulus is computed. This data's shear modulus graph trends similarly to that of the Young's modulus, with values for tissue shear modulus spanning from 0.05 MPa to 0.25 MPa and peaking within the inclusion. This response to the applied displacement is a dilatational and deviatoric response. As the material is deformed the tissue, acting as a dense granular material, tends to expand in its volume as the interlocking and compact state of the cells and tissue restricts the ability to move around one another. This leads to the increase in volume, often leading to expansion in the out of plane direction of the system. Additionally, the deviatoric response of the system shows that the stress induced on the system from the transducer displacement will contribute to the change in shape of the tissue and its tendency to try and resist the change in its shape. These two mechanics are seen at work in Figure 33 as the benign tumor’s shape remains largely unchanged, as its deviatoric response is to resist the change in shape, while the dilatational response is to increase the volume as the shear increases, leading to a higher stress value within the tissue and the occurrence of out of plane strain that may occur. This can help explain why the displaced tissue is able to generate these results during the reconstruction and are evident throughout the phantom data sets. The advantage to calculating the Poisson’s ratio and shear modulus is not immediately evident in the benign data set as the inclusion is readily seen in all result images with the images appearing like one another. The advantages of calculating the Poisson’s ratio and Shear modulus of the material can be seen when analyzing the results from the bifocal data set, which are illustrated in Figure 34.

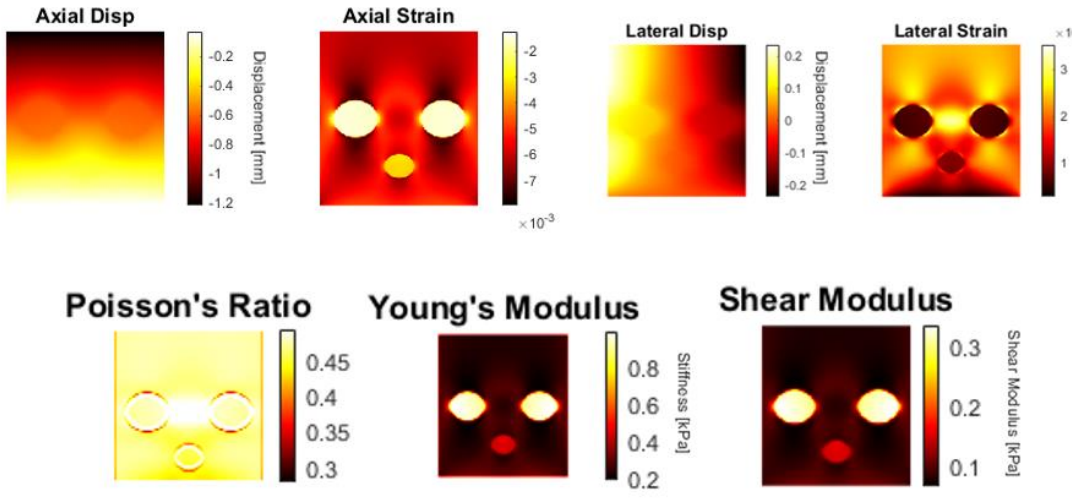

Figure 34: The results from the Trifocal phantom data set. showing the Displacement and strains from AM2D and STREAL, as well as the reconstructed Poisson’s ratio, Stiffness and Shear modulus values for the phantom. The small benign inclusion is easily seen in the reconstructed images along with the two larger malignant tumors.

In Figure 34 the displacements in both the axial and lateral displacements show the two larger inclusions but fail to show the small inclusion located in the central bottom portion of the image at all. Calculating the axial and lateral strains, the small inclusion becomes visible, but at the cost of producing high and low strain artifacts around the inclusions, which may be mistaken for malignant tissue due to its deviation from the background material’s properties. Iterative reconstruction of Poisson’s ratio and Young’s modulus provide additional information about the inclusions. The Poisson’s ratio again shows the ring around the inclusions, and as discussed with the benign data set, can demonstrate that there is high axial strain present at the boundaries of the inclusions and background material, which may be causing out of plane strain to occur, resulting in less calculated incompressibility around the edges of the inclusions. Additionally, the Young's modulus shows that the areas of strain that deviate from the average tissue strain in the axial and lateral directions are not caused by an increase in stiffness typically associated with malignant tissue. Finally, the Shear modulus is the fusion of the Poisson's ratio and the Young's modulus and combines the increased smoothness of the Young's modulus and the easily identifiable outlining of the inclusions within the background material. Noting that benign lesions tend to have small degree of bonding with background tissue compared to malignant tumors, the shear modulus of the ring area can be essentially used as valuable diagnostic information to distinguish benign lesions from malignant tumors.

To show the potential of Poisson's ratio reconstruction a FE model created by Rivaz *et al.* [39] was used as an initial data set to show the outputs of the reconstruction that can be compared against values calculated from the Abaqus FEA. The Rivaz Phantom consists of isotropic and homogeneous background and central circular inclusion. The model is meshed using triangular plane stress elements for both the inclusion and background. The inclusion in the background material is assigned material properties to that of blood. While not following a cancer model, the phantom allows for differing incompressibility to be modeled and will utilize a compressibility value of 0.49 for the central inclusion, 0.48 for the background, and sets the stiffness to be 40 kPa for the inclusion and 20 kPa for the background [39]. The meshed phantom can be seen in Figure 35. A contact is simulated between a transducer and the model such that the material is deformed under the contact load.

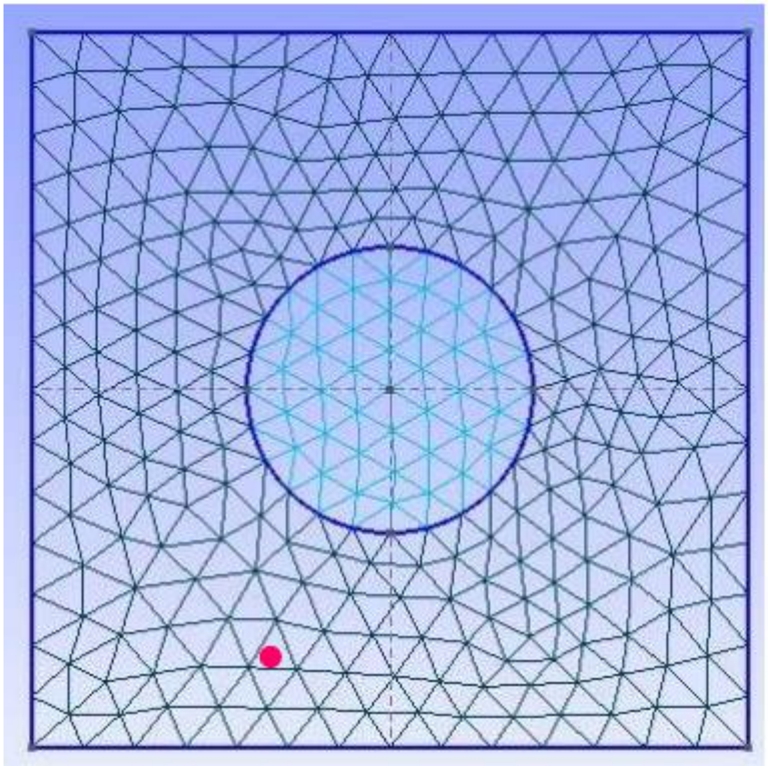

Figure 35: The FE mode used to generate the displacement and strain data for use in the Poisson's ratio reconstruction algorithm. The model consists of a background material and the inner inclusion mimicking a blood vessel where the incompressibility is high.

Processing the displacement initially with AM2D and STREAL allow for the generation of the refined strain field, which is visualized in Figure 36.

From the strains the reconstruction algorithm is initiated, and the Poisson's ratio and stiffness are iterative calculated using Abaqus FEA. The Shear modulus is then directly calculated from these values using Equation 4.4 as done previously. The results of the reconstruction are seen in Figure 37.

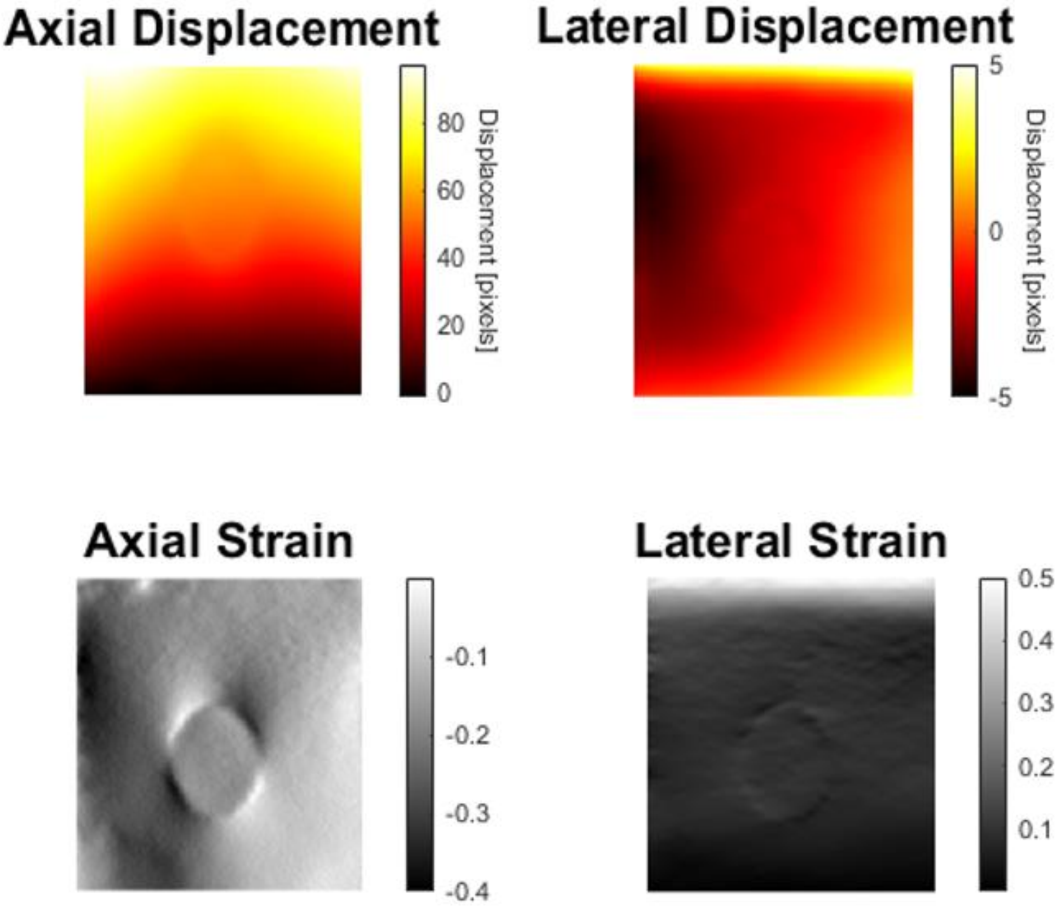

Figure 36: The displacements and strains of the Rivaz phantom. The original estimates were calculated using AM2D and then refined using STREAL. The strains will be used as a convergence check for the reconstruction algorithm.

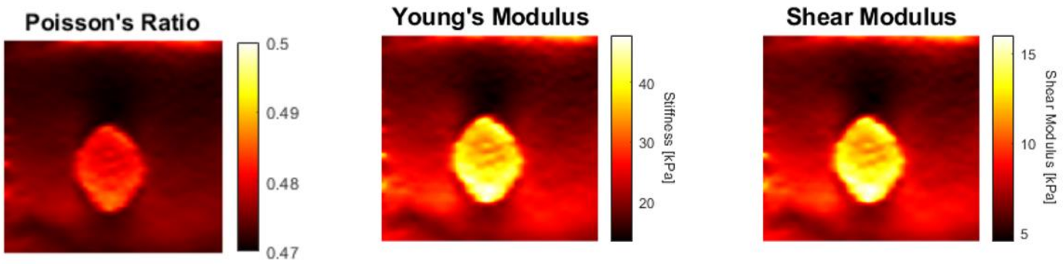

Figure 37: The Reconstruction results showing the Poisson's ratio (Left), Stiffness (center) and Shear modulus (Right)

The results show that the Poisson’s ratio shows that the central inclusion has a Poisson’s ratio of approximately 0.48, while the background has a Poisson’s ratio closer to 0.47. The Young’s modulus and Shear modulus both show similar patterns, with the inclusion having a higher value for the stiffness and shear modulus in comparison to the background material. This is also consistent with the FEA model as the background materials stiffness is set to 20 kPa and the inclusion to 50 kPa in the FEM. The reconstruction shows that it can generate results within the expected range of values for the stiffness consistently. The

4.3 Tissue Mimicking Phantom Results and Discussion

Moving beyond the *in silico* data sets and utilizing the TMP outlined in Chapter 3, this iterative reconstruction can be tested on more realistic data. The data collection required scanning the TMP with a TRUS probe from the Ultrasonix RP scanner, which utilized the Ultrasonix BPC8-4/10 side-fired TRUS probe. This transducer is designed to image internal organs, such as the prostate, and therefore has a small, curved array that allows for internal imaging and data collection during a quasi-static TRUS procedure.

Data collected from the TMP and US probe seen in Chapter 3 is used as the basis for the reconstruction algorithm, with the initial displacements calculated by AM2D Polar, and refined using the STREAL algorithm. The B-mode images of the pre- and post-compression images, the radial displacement and strain, and the angular displacement and strain, are seen in Figure 38. As in Chapter 3, the displacements and strains display some information about the inclusion, which can be seen in the lower center of the strain images. While the strain images provide information proving that the strain is lower throughout the foam inclusion, they do not provide information about the overall stiffening of the tissue, an indication of cancer, especially in the prostate.

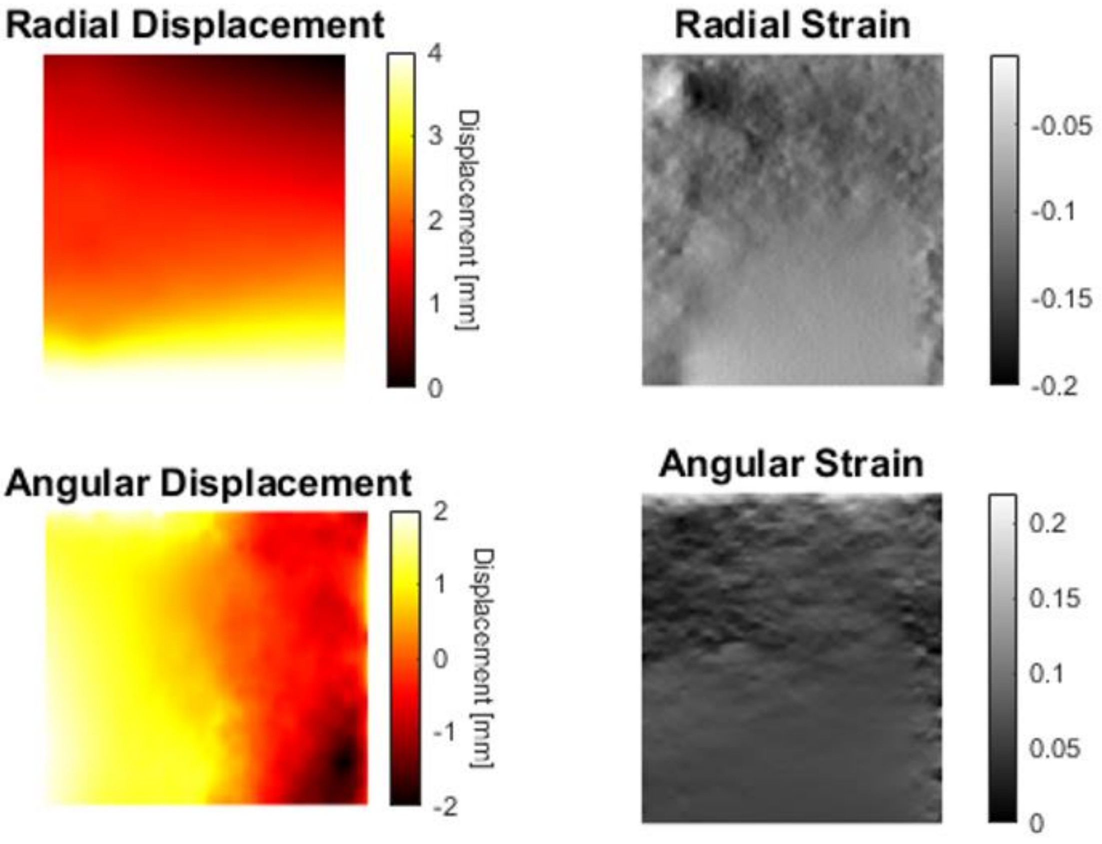

Figure 38: Radial displacement and strain, and angular displacement and strain found with AM2D and refined by STREAL that will be used to calculate the Poisson's ratio and Material Stiffness.

Using the FEA iterative process to calculate the stiffness and Poisson's ratio, will yield the results seen in Figure 39. Using the information from this process, the shear modulus is also calculated.

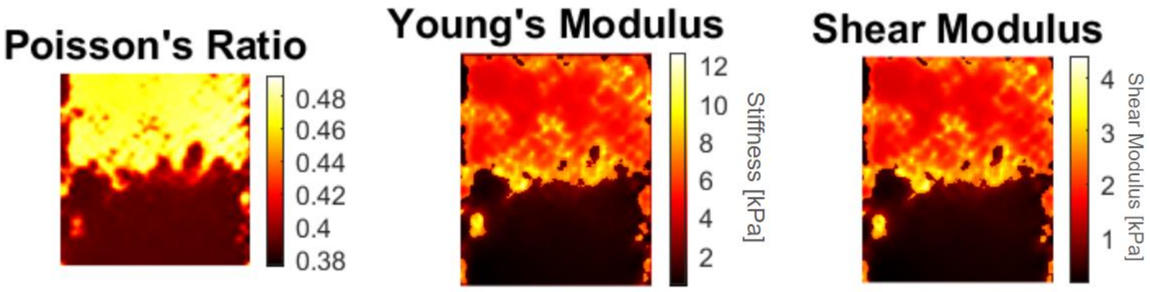

Figure 39: The Poisson's ratio, Young's modulus and shear modulus of the TMP.

From the Poisson's ratio reconstruction, the foam inclusion has a higher compressibility than that of the background material. There are some areas of lower Poisson's ratio seen at the edges of the image, which can be attributed to slippage in the gelatin used for the TMP. Gelatin slippage induces the appearance of a greater strain as the material is displacing much more than under non-slipping conditions. Looking at the Young’s modulus reconstruction of the TMP the foam inclusion is seen in the large section of low stiffness, in the lower center of the image. The minimum value for this section is 17.29 kPa with the highest value occurring in a small section shown as a yellow dot in the lower left corner of the image, with a value of 66.82 kPa. This value for the gelatin lies just under the expected stiffness of the gelatin and may be caused by noise that was propagated through AM2D and STREAL’s calculation of the strains and displacement field. To eliminate this noise from the system, additional smoothing or constraints can be placed on the outputs of STREAL to ensure that points that lie outside the expected tissue range are normalized. Using the Young’s modulus values, and Poisson’s ratio with Equation 4.4, the shear modulus is calculated for each point in the image. The shear modulus uses the Poisson’s ratio along with the Young’s modulus to show a detailed view of the stiffness and compressibility of the tissue in one image. The Shear modulus shows the high spot in a much larger area and shows a gradient of stiffness around the bounding edge of the inclusion, that is not seen in the Young’s modulus reconstruction. Shear modulus shows additional high spots towards the center of the image, that are not present in either the Poisson’s reconstruction or the Young’s modulus reconstruction. The fusion of the data sources can highlight previously hidden changes in stiffness which aid in the diagnosis of stiffened cancerous prostate tissue.

The reconstruction algorithms proposed iteratively refine the stresses and incompressibility of the imaged tissue. The additional tissue mechanic information calculated with this method improves the visibility in the resultant images of areas with material properties that indicate malignant tissue. This process, while slightly more time consuming in comparison to the displacement and strain calculations computed in AM2D and STREAL, provides data that can be fused to calculate the shear modulus of the tissue, which allows for another source of information available in diagnosis of problematic tissue.

Chapter 5

5 Conclusion and Future Work

The implementation of USE achieves enhanced prostate cancer diagnostics, offers high precision, specificity, and reduced time expenditure. The growing application of displacement tracking algorithms like AM2D and STREAL represents a significant advancement within the field of USE. These algorithms, building upon the basic foundations of tissue tracking with DP and analytic minimization, enforce realistic tissue properties and regularization to improve results. Incorporating additional post-processing to calculate tissue properties such as stiffness, incompressibility, and shear modulus enhances the visibility of cancerous tissue within the prostate.

Employing *in silico* data to evaluate displacement data algorithms offers a powerful and accurate method of determining the error between an estimated output and a known ground truth. Field-ii uses a mathematically derived solution for the spatial impulse response of a field to generate accurate and realistic RF data from a bitmap image. Researchers can use this data generation to construct RF data with any inclusion or anatomy that may be observed during US imaging. By utilizing an FEA model to calculate tissue displacements on realistic geometry, it is possible to quantify and store this data for use in the Field-ii software, generating a compressed data set. Post-compression data combines pre-compression data and the known displacement field. The *in silico* validation data sets consistently depict the prostate capsule within a background environment, with an equivalent quantity of scattering agents present in both the input and output images.

By using Field-ii to develop *in silico* data sets, it is possible to create realistic data sets using images or matrices containing image information. This system can produce and process several realistic scans for use in developing new displacement tracking algorithms without the need for a real US machine, thus lowering the entry cost into USE. Field-ii allows for any number of inclusions, image artifacts, or material types depending on the image data created and supplied to the algorithm. This again allows for the creation of low-cost realistic data. As Field-ii employs single line acquisition for the simulated data sets, it takes a considerable amount of time to complete the simulation. Further adaptations can be made to the parallel computer implementations, or the number of scatterers supplied to the calculation algorithm reduced to decreased computation time. In parallel computing, the entire set of scatters is dispatched to each algorithm call for calculation, with several threads simultaneously processing the lines in parallel instead of one after the other. This provides the opportunity to increase the speed of data acquisition and can provide researchers with larger quantities of datasets. An alternative to parallel computing is the reduction in the number of scatters sent to the calculation algorithm. The reduction in scatters means that a smaller number of matrix calculations will need to be done for each line in the acquisition, leading to an increase in calculation speed. The number of scatters can be reduced based on the size of the beam focus and the overall field of view of the transducer. An analysis would be required to determine the minimal percentage of scatters to send, while still maintaining high quality data acquisition. It may also prove useful to conduct a study on the quality of the data when both the parallel computing and minimal scatter calculation speed improvements are applied for the purpose of generating curved transducer data sets.

In addition to the data generated by Field-ii, a real TRUS probe was utilized to generate RF data. Researchers created a TMP using gelatin and foam to form a background material with an accurately sized prostate capsule to accomplish this. This phantom utilizes silica beads as a scattering agent. The Ultrasonix RP US system can be utilized with a TRUS probe to gather precise RF data by using material that will respond to the produced pressure wave. While not having a ground truth as seen in the Field-ii generated data, the TMP is valuable as the imaging quality is that of an actual clinical use case, where artifacts and lower-quality images are generated. Several different scans of the TMP were taken, with both pre-and post-compression datasets being generated. The Phantom study also enables the use of materials that have different material properties to that of human tissue. For instance, foam can be used as an alternative to animal tissue when completely soaked in a saline solution but deviates from human tissue properties as the foam becomes unsaturated. This foam with reduced saturation differs from the properties of human tissue as it has more compressibility and stiffness. This distinction is valuable for assessing the extent to which an algorithm is applicable or able to identify values that are subject to testing. By altering the material present in the phantom’s inclusion, different aspects of the algorithm’s capability can be studied. The steps outlined for constructing the TMP can be altered such that algorithms, such as the Poisson’s ratio reconstruction, are tested for various attributes. Future research may examine the reconstruction algorithm’s usefulness when tissue properties are similar, such as when the inclusion and background material are close in compressibility or stiffness. The study may explore shortcomings of the algorithm or consider limitations that can be addressed with future iterations.

Following data acquisition with both a ground truth data set and the TMP data, the alterations required for AM2D to work with a polar dataset were developed. This process involved creating a new cost function that utilized the Taylor series expansion of the data term for a polar grid, consistent with the TRUS probes used in clinical prostate examinations. The creation of AM2D polar allows for rapid processing of sub-pixel displacements for the radial direction and integer values for the angular direction. Results for both the *in silico* and phantom showed a frame rate consistent with real-time scanning, allowing for real-time processing of the displacements and strains seen in the tissue. Additionally, the quality of the radial direction is consistent with the Cartesian version, showing quality radial direction displacement data. However, the angular direction displacement and strain data for both the simulated and TMP datasets are low and require additional processing to rectify the noisy appearance.

To address the quality issues in the angular directions and increase the accuracy of the radial direction, tissue mechanics are utilized. STREAL, for instance, enforces Laplacian filtering, strain compatibility enforcement, and incompressibility in real-time using convolutional filtering and matrix operations. This process significantly refines the angular direction displacement and strains, reducing the error seen in the simulated data sets and increasing the visibility of the prostate capsule in the TMP output images. This practical application of STREAL as a powerful tool increases the amount of information available to clinicians when diagnosing malignant tumors within the prostate.

For further information about the tissue health within the prostate, reconstructions of the prostate’s stiffness, incompressibility, and shear modulus can be made. Using the FEA tool Abaqus, Young’s modulus and Poisson’s ratio can be estimated using the strain images generated by STREAL and an inverse relationship between the stiffness and stress in the system. Once the iterative process is complete, estimates for Young’s modulus and

Poisson's ratio are imaged. Poisson's ratio combined with the Young's modulus is used to reconstruct the tissue's shear modulus, with the potential of showing the amount of shear deformation in the tissue around the inclusion due to compressive loading. Assessment of this deformation may provide further clues about the abnormal tissue malignancy.

Continued development of the STREAL and Poisson's ratio reconstruction algorithms is imperative as it holds the potential to improve the accuracy of US scans for prostate cancer detection. Clinical trials are needed to ensure that the AM2D polar, STREAL, and Poisson's ratio reconstruction algorithms are suitable to use on clinical data and provide meaningful results both for clinicians and for future studies. Validating the results on clinical trials requires a lengthy ethical approval process which will ensure that several participants and research groups are found and informed of the procedures extent to ensure that a statistically significant value is obtained within an ethical study.

Overall, the development of USE in diagnosing carcinoma and other tissue stiffening related malignancies shows the power in creating and improving upon the existing algorithms. AM2D provides a useful and fast approximate view of the tissue's overall displacement and strain, while STREAL can refine the results into accurate representations of the strain within the tissue. Utilizing the information gathered from AM2D and STREAL allows for additional post-processing of the information into new material properties, such as the stiffness and incompressibility of the tissue. Fusing these results into the shear modulus allows for additional parameters to be gleaned from the tissue displacement acquired during the Quasi-static USE procedure. Studying the overall effectiveness of these algorithms and expanding on their accuracy and speed will allow for the continued and rapid diagnosis of prostate cancer without the need for lengthy acquisition time, such as with MRI, or with possible false outcomes, possible in DRE and PSA tests.

References

[1] Canadian Cancer Society, "Prostate Cancer Statistics," November 2023. [Online]. Available: https://cancer.ca/en/cancer-information/cancer-types/prostate/statistics.

[2] A. Ali, "Prostate zones and cancer: lost in transition?," *Nature Reviews Urology,* vol. 1, no. 19, pp. 101-115, 2022.

[3] Mayo Clinic, "Prostate Cancer," Mayo Clinic, Dec 2022. [Online]. Available: https://www.mayoclinic.org/diseases-conditions/prostate-cancer/symptoms-causes/syc-20353087. [Accessed 2024].

[4] American Society of Clinical Oncology, "Digital Rectal Exam (DRE)," American Society of Clinical Oncology, 09 2020. [Online]. Available: https://www.cancer.net/navigating-cancer-care/diagnosing-cancer/tests-and-procedures/digital-rectal-exam-dre. [Accessed 2024].

[5] L. Naji, H. Randhawa, Z. Sohani, B. Dennis, D. Lautenbach, O. Kavanagh, M. Bawor, L. Banfield and J. Profetto, "Digital Rectal Examination for Prostate Cancer Screening in Primary Care: A Systematic Review and Meta-Analysis," *Annals of Family Medicine,* vol. 16, no. 2, pp. 149-154, 2018.

[6] National Institute of Health, "Prostate Specific Antigen Test," National Cancer Institute, 11 03 2022. [Online]. Available: https://www.cancer.gov/types/prostate/psa-fact-sheet. [Accessed 2024].

[7] Mayo Clinic, "Prostate Biopsy," Mayo Clinic, 27 April 2023. [Online]. Available: https://www.mayoclinic.org/tests-procedures/prostate-biopsy/about/pac-20384734. [Accessed 2024].

[8] M. S. Leapman, "Prostate Magnetic Resonance Imaging (MRI)," UCSF Department of Urology, 12 2015. [Online]. [Accessed 2024].

[9] National Institutes of Health, "Magnetic Resonance Imaging (MRI)," U.S. Department of Health and Human Sciences, [Online]. Available: https://www.nibib.nih.gov/science-education/science-topics/magnetic-resonance-imaging-mri. [Accessed 2024].

[10] Johns Hopkins, "Prostate/ Rectal Ultrasound," Johns Hopkins Medicine, [Online]. Available: https://www.hopkinsmedicine.org/health/treatment-tests-and-therapies/prostate-rectal-sonogram#:~:text=What%20is%20a%20prostate%2Frectal,the%20size%20of%20a%20finger.. [Accessed 2024].

[11] RadiologyInfo, "Elastography," Radiology Info, 01 04 2024. [Online]. Available: https://www.radiologyinfo.org/en/info/elastography. [Accessed 2024].

[12] J.-L. Gennisson, T. Deffieux, M. Fink and M. Tanter, "Ultrasound elastography: Principles and techniques," *Diagnostic and Interventional Imaging,* vol. 94, no. 5, pp. 487-495, 2013.

[13] M. Doyley, P. Meaney and J. Bamber, "Evaluation of an iterative reconstruction method for quantitative elastography," *Physics in Medical Biology,* no. 45, pp. 1521-1540, 2000.

[14] S. R. Mousavi, A. Sadeghi-Naini, G. J. Czarnota and A. Samani, "Towards clinical prostate ultrasound elastography using full inversion approach," *Medical Physics,* vol. 41, no. 3, 2014.

[15] M. S. Taljanovic, "Shear-Wave Elastography: Basic Physics and Musculoskeletal Applications," *Radiographics,* vol. 37, no. 3, pp. 855-570, 2017.

[16] V. Murthy, Principles and Practices of Soil Mechanics and Foundation Engineering, CRC Press, 2003.

[17] R. Barr and G. Ferraioli, Multiparametric Ultrasound for the Assessment of Diffuse Liver Disease, Elsevier, 2023.

[18] T. Varghese, "Quasi-Static Ultrasound Elastography," *Ultrasound Clinics,* vol. 4, no. 3, pp. 323-338, 2009.

[19] X. Gao, F. Hao, D. Fang and Z. Huang, "Boussinesq problem with the surface effect and its application to contact mechanics at the nanoscale," *International Journal of Solids and Structures,* vol. 50, no. 16-17, pp. 2620-2630, 2013.

[20] P. Kelly, Solid Mechanics Part II: Engineering Solid Mechanics, Auckland, 2013.

[21] T. A. Krouskop, T. M. Wheeler, F. Kallel, B. S. Garra and T. Hall, "Elastic Moduli of Breast and Prostate Tissues under Compression," *Ultrasonic Imaging,* vol. 20, no. 4, pp. 260-274, 1998.

[22] National Institute of Biomedical Imaging and Bioengineering, "Ultrasound," National Institute of Health, Dec 2023. [Online]. Available: https://www.nibib.nih.gov/science-education/science-topics/ultrasound#:~:text=How%20does%20it%20work%3F,-Source%3A%20Terese%20Winslow&text=Ultrasound%20waves%20are%20produced%20by,ceramic%20crystal%20materials%20called%20piezoelectrics.. [Accessed 2024].

[23] J. Lacefield, *BME9513 Introduction to Medical Ultrasound,* London: University of Western Ontario, 2022.

[24] L. Demi, "Practical Guide to Ultrasound Beam Forming: Beam Pattern and Image Reconstruction Analysis," *MDPI: Applied Sciences,* vol. 8, no. 9, p. 1544, 2018.

[25] P. Y. Barthez, R. Léveillé and P. V. Scrivani, "Side lobes and grating lobes artifacts in ultrasound imaging," *PubMed,* vol. 38, no. 5, pp. 387-393, 1997.

[26] G. Montaldo, M. Tanter, J. Bercoff, N. Benech and M. Fink, " Coherent Plane-Wave Compounding for Very High Frame Rate Ultrasonography and Transient Elastography," *IEEE Transactions Ultrasonic Ferroelectric Frequency Control,* no. 56, pp. 489-506, 2009.

[27] M. Karaman and M. O'Donnel, "Subaperture processing for ultrasonic imaging," *IEEE Transactions Ultrasonic Ferroelectric Frequency Control,* no. 45, pp. 126-135, 1998.

[28] T. Comen, H. Leiserson, C. E. Rivest and R. L. Stein, "Dynamic Programming," in *Introduction to Algorithms*, MIT Press and McGraw Hill, 2001, pp. 344-350.

[29] C. Lemarechal, "Cauchy and the Gradient Method," in *Optimization Stories*, Berlin, 2012.

[30] S. Smith, "13. Convolution," in *The Scientist and Engineer's guide to Digital Signal Processing*, California Technical Publishing, 1997.

[31] H. Rivaz, E. Boctor, M. Choti and G. Hager, "Ultrasound elastography using multiple images," *Medical Image Analysis,* vol. 18, no. 2, pp. 314-329, 2014.

[32] U. Sara, M. Akter and M. Shorif, "Image Quality Assessment through FSIM, SSIM, MSE and PSNR—A Comparative Study," *Journal of Computer Communications,* vol. 7, no. 3, 2019.

[33] M. A. Sutton, J.-J. Orteu and H. W. Schreier, "Digital Image Correlation (DIC)," in *Image Correlation for Shape, Motion and Deformation Measurements*, Springer, 2009, pp. 96-133.

[34] P. Anuta, "Spatial registration of multispectral and multitemporal digital imagery using fast Fourier transform techniques," *IEEE Transactions on Geoscience Electronics,* vol. 8, pp. 353-368, 1970.

[35] A. A. Goshtasby, 2-D and 3-D Image Registration: for Medical, Remote Sensing, and Industrial Applications, Wiley, 2005, pp. 4-62.

[36] D. J. Schroeder, Astronomical Optics, Academic Press, 1999.

[37] J. Hou, L. Ning and L. Yao, "A High-Fidelity Haze Removal Method Based on HOT for Visible Remote Sensing Images," *MDPI: Remote Sensing,* vol. 8, no. 10, 2016.

[38] G. Salomon, J. Köllerman, I. Thederan, F. K. Chun, L. Budäus, T. Schlomm, H. Isbarn, H. Heinzer, H. Huland and M. Graefen, "Evaluation of Prostate Cancer Detection with Ultrasound Real-Time Elastography: A Comparison with Step Section Pathological Analysis after Radical Prostatectomy," *European Urology,* vol. 54, no. 6, pp. 1354-1362, 2008.

[39] H. Rivaz, E. Boctor, M. Choti and G. Hager, "Real-Time Regularized Ultrasound Elastography," *IEEE Trans. Medical Imaging,* vol. 30, pp. 928-945, 2011.

[40] H. Rivaz, E. Boctor, P. Foroughi, R. Zellars, G. Fichtinger and G. Hager, "Ultrasound Elastography: a Dynamic Programming Approach," *IEEE Trans. Medical Imaging,* vol. 27, pp. 1373-1377, 2008.

[41] H. Hashemi and H. Rivaz, "Global Time-Delay Estimation in Ultrasound Elastography," *IEEE Trans. Ultrasonics Ferroelectrics Frequency Control,* vol. 64, pp. 1625-1636, 2017.

[42] M. S. Hoogeman, M. v. Herk, J. d. Bois and J. V. Lebesque, "Strategies to reduce the systematic error due to tumor and rectum," *Radiotherapy and oncology,* vol. 27, no. 2, pp. 177-185, 2005.

[43] N. Kheirkhah, S. Dempsey, A. Sadeghi-Naini and A. Samani, "A novel tissue mechanics-based method for improved," *Medical Physics,* vol. 50, no. 4, pp. 2176-2194, 2023.

[44] Ashikuzzaman, A. Sadeghi-Naini, A. Samani and H. Rivaz, "Combining First- and Second-Order Continuity Constraints in Ultrasound Elastography," *IEEE Transactions on Ultrasonics, Ferroelectrics, and Frequency Control,* vol. 68, no. 7, pp. 2407-2418, 2021.

[45] A. Samani, J. Bishop and D. B. Plewes, "A Constrained Modulus Reconstruction Technique," *IEEE TRANSACTIONS ON MEDICAL IMAGING,,* vol. 20, no. 9, pp. 877-885, 2001.

[46] J. Ophir, F. Kallel, T. Varghese, M. Bertrand, I. Cespedes and H. Ponnekanti, "Elastography: A systems approach," *International Journal of Imaging Systems and Technology,* pp. 89-103, 1997.

[47] S. R. Mousavi, H. Rivaz, G. J. Czarnota, A. Samani and A. Sadeghi-Naini, "Ultrasound Elastography of the Prostate Using an Unconstrained Modulus Reconstruction Technique: A Pilot Clinical Study," *Translational Oncology,* vol. 10, no. 5, pp. 744-751, 2017.

[48] T. Islam, S. Tang, C. Liverani, S. Saha, E. Tasciotti and R. Righetti, "Non-invasive imaging of Young's modulus and Poisson's ratio in cancers in vivo," *Scientific Reports,* vol. 10, 2020.

[49] E. Brusseau, L. Petrusca, E. Bretin, P. Millien and L. Seppecher, "Reconstructing the shear modulus contrast of linear elastic and isotropic media in quasi-static ultrasound elastography," in *Annu Int Conf IEEE Eng Med Biol Soc.*, 2021.

[50] J. Jensen and N. B. Svendsen, "Calculation of pressure fields from arbitrarily shaped, apodized, and excited ultrasound transducers," *IEEE Trans. Ultrason., Ferroelec., Freq. Contr.,* vol. 39, pp. 262-267, 1992.

[51] G. Tupholme, "Generation of acoustic pulses by baffled plane pistons," *Mathematika,* vol. 16, pp. 209-224, 1969.

[52] P. Stepanishen, "The time-dependent force and radiation impedance on a piston in a rigid infinite planar baffle," *J.Acoust.Soc.Am.,* vol. 49, no. 3, pp. 841-849, 1971.

[53] J. Jensen, "Field: A Program for Simulating Ultrasound Systems," in *10th Nordic-Baltic Conference on Biomedical Imaging Published in Medical & Biological Engineering & Computing*, 1996.

[54] J. A. Jensen and P. Munk, "Calculation of B-mode image of synthetic kidney," Field-ii: The software Scanner, 29 March 2000. [Online]. [Accessed 2024].

[55] A. Samani, J. Bishop, M. J. Yaffe and D. B. Plewes, "Biomechanical 3-D finite element modeling of the human breast using MRI data," *IEEE Transactions on Medical Imaging,* vol. 20, no. 4, pp. 271-279, 2001.

[56] T. A. Laursen, Computational Contact and Impact Mechanics: Fundamentals of Modeling Interfacial Phenomena in Nonlinear Finite Element Analysis, Berlin: Springer, 2003.

[57] M. O. Culjat, D. Goldenberg, P. Tewari and R. S. Singh, "A Review of Tissue Substitutes for Ultrasound Imaging," *Ultrasound in Med. & Biol.,* vol. 36, no. 6, pp. 861-873, 2010.

[58] T. D. Mast, "Empirical relationships between acoustic parameters in human soft tissues," *ARLO,* vol. 1, no. 2, 2000.

[59] M. Czerner, L. S. Fellay, M. P. Suárez, P. M. Frontini and L. A. Fasce, "Determination of Elastic Modulus of Gelatin Gels by Indentation Experiments," *International Congress of Science and Technology of Metallurgy and Materials,* no. 8, pp. 287-296, 2013.

[60] R. A. Lerski, T. C. Duggan and J. Christie, "A simple tissue-like ultrasound phantom material," *British Journal of Radiology,* vol. 55, pp. 156-157, 1982.

[61] M. Mitterberger, W. Horninger, F. Aigner, G. M. Pinggera, I. Steppan, P. Rehder and F. Frauscher, "Ultrasound of the prostate," *Cancer Imaging,* vol. 10, no. 1, pp. 40-48, 2010.

[62] M. Mirzaei, A. Asif and H. Rivaz, "Combining Total Variation Regularization with Window-based Time Delay Estimation in Ultrasound Elastography," *IEEE Trans. Medical Imaging,* vol. 38, no. 12, 2019.

[63] Ashikuzzaman and H. Rivaz, "Second-Order Ultrasound Elastography With L1-Norm Spatial Regularization," *IEEE Trans Ultrason Ferroelectr Freq Control,* vol. 69, no. 3, pp. 1008-1019, 2022.

[64] M. Caius and A. Samani, "Comparative Study of Ultrasound Tissue Motion Tracking Techniques for Effective Breast Ultrasound Elastography.," *Applied Sciences,* vol. 13, no. 21, 2023.

[65] Brown University School of Engineering, "Vectors and Tensor Operations in Polar Coordinates," Brown University, [Online]. Available: https://www.brown.edu/Departments/Engineering/Courses/En221/Notes/Polar_Coords/Polar_Coords.htm. [Accessed 2024].

[66] B. Kim, J. Sun, S. Kim, M. Kang and S. Ko, "CNN-based UGS method using Cartesian-to-polar coordinate transformation," *Image and vision processing and display technology,* vol. 54, no. 23, pp. 1321-1322, 2018.

Appendix A – Field-ii RF Data Generation for Kidney Phantom

Appendix A1 – Kidney Scatterer Generation

```
function [positions, amp] = human_kidney_phantom (N)

    % Load the bitmap image

    [liv_kid, ~]=bmpread('kidney_cut.bmp');

    % Define image coordinates

    liv_kid=liv_kid';
    [Nl, Ml]=size(liv_kid);

    x_size = 100/1000 ;    %  Size in x-direction [m]
    dx=x_size/Nl;          %  Sampling interval in x direction [m]
    z_size = 100/1000 ;    %  Size in z-direction [m]
    dz=z_size/Ml;          %  Sampling interval in z direction [m]
    y_size = 15/1000;      %  Size in y-direction [m]
    theta = 0;
    z_start = 2/1000;

    % Calculate position data

    x0 = rand(N,1);
    x = (x0-0.5)* x_size;
    z0 = rand(N,1);
    z = z0*z_size+z_start;
    y0 = rand(N,1);
    y = (y0-0.5)* y_size;

    %  Find the index for the amplitude value

    xindex = round((x + 0.5*x_size)/dx + 1);
    zindex = round((z - z_start)/dz + 1);
    inside = (0 < xindex)  & (xindex <= Nl) & (0 < zindex)  & (zindex <= Ml);
    index = (xindex + (zindex-1)*Nl).*inside + 1*(1-inside);

    % Amplitudes with different variance must be generated according to the the
    % input map.
    % The amplitude of the liver-kidney image is used to scale the variance

    amp=exp(liv_kid(index)/100);
    amp=amp-min(min(amp));
    amp=1e6*amp/max(max(amp));
    amp=amp.*randn(N,1).*inside;

    %  Generate the rotated and offset block of sample

    xnew=x*cos(theta)+z*sin(theta);
    znew=z*cos(theta)-x*sin(theta);
    znew=znew-min(min(znew)) + z_start;

    positions=[xnew y znew];
end
```

Appendix A2 – Kidney Ultrasound Data Generation

```
%  Generate the transducer apertures for send and receive
f0=7e6;                  %  Transducer center frequency [Hz]
fs=100e6;                %  Sampling frequency [Hz]
c=1540;                  %  Speed of sound [m/s]
lambda=c/f0;             %  Wavelength [m]
width=lambda/2;          %  Width of element
element_height=5/1000;   %  Height of element [m]
kerf=lambda/10;          %  Kerf [m]
focus=[0 0 90]/1000;     %  Fixed focal point [m]
N_elements=128;          %  Number of physical elements

%  Set the sampling frequency
set_sampling(fs);
set_field ('show_times', 5)

%  Generate aperture for emission
xmit_aperture = xdc_linear_array (N_elements, width, element_height, kerf, 1, 5,
focus);

%  Set the impulse response and excitation of the xmit aperture
impulse_response=sin(2*pi*f0*(0:1/fs:2/f0));
impulse_response=impulse_response.*hanning(max(size(impulse_response)))';
xdc_impulse (xmit_aperture, impulse_response);

excitation=sin(2*pi*f0*(0:1/fs:2/f0));
xdc_excitation (xmit_aperture, excitation);

%  Generate aperture for reception
receive_aperture = xdc_linear_array (N_elements, width, element_height, kerf, 1, 5,
focus);

%  Set the impulse response for the receive aperture

xdc_impulse (receive_aperture, impulse_response);

%   Load the computer phantom
load pht_data

%  Set the different focal zones for reception
focal_zones=[5:1:150]'/1000;
Nf=max(size(focal_zones));
focus_times=(focal_zones-10/1000)/1540;
z_focus=60/1000;          %  Transmit focus

%  Set the apodization
apo=hanning(N_elements)';
xdc_apodization (xmit_aperture, 0, apo);
xdc_apodization (receive_aperture, 0, apo);
```

Appendix A3 – Phased Array Imaging of the Kidney

```
%   Do phased array imaging
no_lines=128;                  %  Number of lines in image
image_width=90/180*pi;         %  Size of image sector [rad]
dtheta=image_width/no_lines;   %  Increment for image

% Do imaging line by line
for i=1:128

    if ~exist(['rf_data/rf_ln',num2str(i),'.mat'])
        cmd = ['save rf_data/rf_ln',num2str(i),'.mat i'];
        eval(cmd)

        %   Set the focus for this direction
        theta= (i-1-no_lines/2)*dtheta;
        focalZones = [focal_zones*sin(theta), zeros(max(size(focal_zones)),1),...
            focal_zones*cos(theta)];
        xdc_focus (xmit_aperture, 0, [z_focus*sin(theta) 0 z_focus*cos(theta)]);
        xdc_focus (receive_aperture, focus_times, focalZones);

        %   Calculate the received response
        [rf_data, tstart]=calc_scat(xmit_aperture, receive_aperture, ...
            phantom_positions, phantom_amplitudes);

        %  Store the result
        cmd = ['save rf_data/rf_ln',num2str(i),'.mat rf_data tstart'];
        eval(cmd)
    end

end
```

Appendix A4 – Prostate Ultrasound Data Generation

```
function [positions, amp] = human_prostate_phantom (N,BMP_Name)

    % Load the bitmap image preDeformed_crop
    %[bmpData, ~,~] = bmpread(BMP_Name);
    [bmpData, ~] = bmpread(BMP_Name);

    % Define image coordinates
    bmpData = bmpData';
    [Nl, Ml] = size(bmpData);

    x_size = 60/1000;     %  Size in x-direction [m] 100/1000
    dx = x_size/Nl;        %  Sampling interval in x direction [m]
    z_size = 60/1000;     %  Size in z-direction [m] 100/1000
    dz = z_size/Ml;        %  Sampling interval in z direction [m]
    y_size = 5/1000;      %  Size in y-direction [m]
    theta = 35/180*pi;     %  Rotation of the scatterers [rad] 0
    theta = 0;
    z_start = 2/1000;      %  Starting z position [m]


    %Calculate position data
    x0 = rand(N,1);
    x = (x0-0.5) * x_size;
    z0 = rand(N,1);
    z = z0 * z_size+z_start;
    y0 = rand(N,1);
    y = (y0) * y_size;

    %Find the index for the amplitude value
    xindex = round((x + 0.5*x_size)/dx + 1);
    zindex = round((z - z_start)/dz + 1);
    inside = (0 < xindex)  & (xindex <= Nl) & (0 < zindex)  & (zindex <= Ml);
    index = (xindex + (zindex-1)*Nl).*inside + 1*(1-inside);

    %Amplitudes with different variance must be generated according to the input map.
    %The amplitude of the image is used to scale the variance.
    amp = exp(bmpData(index)/100);
    amp = amp - min(min(amp));
    amp = 1e6*amp/max(max(amp));
    amp = amp.*randn(N,1).*inside;

    %Generate the rotated and offset block of sample.
    xnew = x*cos(theta) + z*sin(theta);
    znew = z*cos(theta) - x*sin(theta);
    znew = znew - min(min(znew)) + z_start;

    positions = [xnew y znew];

    figure();
    scatter(positions(:,1), positions(:,3), 3, amp,"filled");

end
```

```
f0 = 7e6;                     %  Transducer center frequency [Hz]
fs = 40e6;                    %  Sampling frequency [Hz]
c = 1540;                     %  Speed of sound [m/s]
lambda = c/f0;                %  Wavelength [m]
width = lambda;               %  Width of element
element_height = 10/1000;     %  Height of element [m]
kerf = width/2;               %  Kerf [m]
Radius_convex = 25/1000;      %  Convex radius [m]
focus = [0 0 30]/1000;        %  Fixed focal point [m]
N_elements = 216;             %  Number of physical elements

%   Set the sampling frequency
set_sampling(fs);
set_field ('show_times', 5);

%   Generate aperture for emission
emit_aperture = xdc_convex_array(N_elements, width, ...
    element_height, kerf, Radius_convex, 1, 5, focus);

%   Set the impulse response and excitation of the xmit aperture
impulse_response = sin(2*pi*f0*(0:1/fs:2/f0));
impulse_response = impulse_response.*hanning(max(size(impulse_response)))';
xdc_impulse(emit_aperture, impulse_response);

excitation = sin(2*pi*f0*(0:1/fs:2/f0));
xdc_excitation(emit_aperture, excitation);

%   Generate aperture for reception
receive_aperture = xdc_convex_array(N_elements, width, ...
    element_height, kerf, Radius_convex, 1, 5, focus);

%   Set the impulse response for the receive aperture
xdc_impulse(receive_aperture, impulse_response);

%   Load the computer phantom
load pht_data

%   Set the different focal zones for reception
focal_zones = [0:1:60]'/1000;
Nf = max(size(focal_zones));
focus_times = (focal_zones-10/1000)/1540;
z_focus = 40/1000;          %  Transmit focus

%   Set the apodization
apo = hanning(N_elements)';
xdc_apodization(emit_aperture, 0, apo);
xdc_apodization(receive_aperture, 0, apo);

%   Do phased array imaging
no_lines = N_elements;
image_width = (90/180)*pi;                %  Size of image sector [rad]
dtheta = image_width/no_lines;            %  Increment for image
startLine = 1;
```

```
for i = startLine:no_lines
        file_name = ['rf_ln',num2str(i),'.mat'];

        %   Set the focus for this direction
        theta = (i-1-no_lines/2)*dtheta;
        focal_zones_x = focal_zones*sin(theta);
        xdc_focus(emit_aperture, 0, [z_focus*sin(theta) 0 z_focus*cos(theta)]);
         xdc_focus(receive_aperture, focus_times, ...

           [focal_zones*sin(theta) zeros(max(size(focal_zones)),1)...
                focal_zones*cos(theta)]);


        % calculate the received rf signals
        [rf_data, tstart] = calc_scat(emit_aperture, ...
            receive_aperture, truncated_positions, truncated_amplitudes);

        %  Store the result
        save(path + file_name, 'rf_data', 'tstart', '-mat');

end
```

Appendix B – TMP Data processing and Quality Analysis

Appendix B1 – Open and Process RF Data Frames

```
[header, ~] = readRFframe(path, filename, upSample, frameN);

% process all frames into matlab data files
for i=1:header.frames
    [~, RFframe] = readRFframe(path, filename, upSample, i);

    Im = RFframe(:,:);
    Name = "TRUS_Pre_" + i + ".mat";
    save(path + '\' + Name,"Im",'-mat');

end

function [header, RFframe] = readRFframe(path, filename, upSample, frameN)
% Author: Reza Zahiri Azar, March 2008, University of British Columbia

fid = fopen(path + '\' + filename, 'r');
% pars the file name for info
hdr = fread(fid, 19, 'int32');
header = struct(  'type', {hdr(1)}, ...
                   'frames', {hdr(2)}, ...
                   'width', {hdr(3)}, ...
                   'height', {hdr(4)}, ...
                   'samplesize', {hdr(5)}, ...
                   'upperleftx', {hdr(6)}, ...
                   'upperlefty', {hdr(7)}, ...
                   'upperrightx', {hdr(8)}, ...
                   'upperrighty', {hdr(9)}, ...
                   'bottomrightx', {hdr(10)}, ...
                   'bottomrighty', {hdr(11)}, ...
                   'bottomleftx', {hdr(12)}, ...
                   'bottomlefty', {hdr(13)}, ...
                   'probe', {hdr(14)}, ...
                   'txfrequency', {hdr(15)}, ...
                   'samplefrequency', {hdr(16)*upSample}, ...
                   'framerate', {hdr(17)}, ...
                   'linedensity', {hdr(18)}, ...
                   'extra1',{hdr(19)},...
                   'upSamp', upSample);

nLines   = header.width;       % number of lines
lLength  = header.height;      % length of each line in samples
% jump to the frame
frameTagSize = 4;               % There is a 4 byte frame index for each frame
fseek( fid, (frameN-1) * ( frameTagSize + nLines *  lLength * header.samplesize/8),
'cof');

% read the frame
disp( fread(fid, 1, 'int32') );   % read the frame index
% up sample as well if requested
RFframe       = resample( fread(fid, [lLength, nLines], 'int16' ) ,
header.upSamp,1,4);   % the actual frame
fclose(fid);
```

Appendix B2 – Data Analysis Algorithm

```
for k = 1:numPreFolders
    for l = 1:numPostFolders
        preFolder = k;
        postFolder = l;
        bestCorrScore = -1.01; % just below lowest correlation score
        bestMSEScore = 100000; % arbitrary high number
        bestCombinedScore = 100000;
        bestCorrScoreIms = [0, 0]; % index markers for best scores
        bestMSEScoreIms = [0, 0];
        bestCombinedScoreIms = [0, 0];

        % automatically gets number of files from path
        a = dir(fullfile(pathPre, '*.mat'));
        endingValPre = numel(a);

        b = dir(fullfile(pathPost, '*.mat'));
        endingValPost = numel(b);

        for i = 1:endingValPre
            for j = 1:endingValPost
                preFrame = i;
                postFrame = j;
                Im1 = load(pathPre + '\' + filenamePre + i + ".mat");
                Im1 = Im1.Im;
                Im2 = load(pathPost + '\' + filenamePost + j + ".mat");
                Im2 = Im2.Im;

                if size(Im2,1) ~= size(Im1,1) | size(Im2,2) ~= size(Im1,1)
                    Im2 = resize(Im2, size(Im1));
                end

                [radial, angular, ~, ~] = AM2D_func(Im1, Im2, B_mode, AM2D_params);
                [corr_score, MSE_score, combined_score] = AssessDataQuality(Im1, ...
                    Im2, radial, angular);
                if corr_score > bestCorrScore
                    bestCorrScore = corr_score;
                    bestCorrScoreIms = [i j];
                end

                if MSE_score < bestMSEScore
                    bestMSEScore = MSE_score;
                    bestMSEScoreIms = [i j];
                end

                if combined_score < bestCombinedScore
                    bestCombinedScore = combined_score;
                    bestCombinedScoreIms = [i j];
                end
                allScores(count, :) =  [preFolder postFolder preFrame postFrame
                    combined_score corr_score MSE_score];
                count = count + 1;
            end
        end
    end
end
```

```
function [corr_score, MSE_score, combined_score] = AssessDataQuality(frame1, frame2,
...axial_displacement, lateral_displacement)

    inverse_func = @(xy) reverse_displacement([xy], axial_displacement,
        lateral_displacement);
    forward_func = @(xy) apply_displacement([xy], axial_displacement,
       lateral_displacement);

    tform = geometricTransform2d(inverse_func, forward_func);
    regenerated = imwarp(frame1, tform);
    regenerated = resize(regenerated,size(frame2),"Side","trailing");

    corr_score = dot(frame2(:)/norm(frame2(:)), regenerated(:)/norm(regenerated(:)));
    MSE_score = sqrt(mean((frame2 - regenerated).^2,"all"))/mean(abs(frame2),"all");
    combined_score = (1 - corr_score) + MSE_score;

end

function out = reverse_displacement(xy, axial_displacement, lateral_displacement)

    out = zeros(size(xy));
    axRes = size(axial_displacement,1);
    latRes = size(axial_displacement,2);
    [X,Y] = meshgrid(linspace(0.5,latRes+0.5,latRes),linspace(0.5, axRes+0.5,
axRes));

    axial_displacements = interp2(X,Y,axial_displacement, xy(:,1), xy(:,2), "cubic");
    axial_displacements(isnan(axial_displacements)) = 0;

    lateral_displacements = interp2(X,Y,lateral_displacement, xy(:,1), xy(:,2),
        "cubic");
    lateral_displacements(isnan(lateral_displacements)) = 0;

    out(:,2) = xy(:,2) - axial_displacements;
    out(:,1) = xy(:,1) - lateral_displacements;

end

function out = apply_displacement(xy, axial_displacement, lateral_displacement)

    out = zeros(size(xy));
    axRes = size(axial_displacement,1);
    latRes = size(axial_displacement,2);
    [X,Y] = meshgrid(linspace(0.5,latRes+0.5,latRes),linspace(0.5, axRes+0.5,
        axRes));

    axial_displacements = interp2(X,Y,axial_displacement, xy(:,1), xy(:,2), "cubic");
    axial_displacements(isnan(axial_displacements)) = 0;

    lateral_displacements = interp2(X,Y,lateral_displacement, xy(:,1), xy(:,2),
        "cubic");
    lateral_displacements(isnan(lateral_displacements)) = 0;
    out(:,2) = xy(:,2) + axial_displacements;
    out(:,1) = xy(:,1) + lateral_displacements;
end
```

Appendix B3 – User-defined Optimization Algorithm

```
function [best_alfa, best_beta, best_gamma] = AM2D_Param_finder(Im1, Im2, params)
    lr_radial = 1/10; % learning rates for paramter growth
    lr_angular = 1/10;
    iter = 1;
    max_iter = 50;
    patience_count = 5;
    patience = true;
    best_score_radial = 100000; % arbitrary large numbers
    best_score_angular = 100000;
    B_mode = 0;
    IRF = [params(1,1) params(1,2)];
    IA = [params(1,3) params(1,4)];
    alfa_DP = params(1,5);
    midA = (size(Im1,2)/2);
    curr_alfa = params(1,6);
    curr_beta = params(1,7);
    curr_gamma = params(1,8);
    T = params(1,9);
    a_t = params(1,10);
    f_0 = params(1,11);
    f_s = params(1,12);
    max_depth = params(1,13);
    FoV_angle = params(1,14);
    num_a_line = params(1,15);

    while (iter < max_iter) && (patience == true)
        AM2D_params = [IRF, IA, alfa_DP, curr_alfa, curr_beta, curr_gamma, T, a_t,
             f_0, f_s, max_depth, FoV_angle, num_a_line];
        [radial, angular, strain1, strain2] = AM2D_func(Im1, Im2, B_mode,
              AM2D_params);
        [corr_score, MSE_score, combined_score] = AssessDataQuality(Im1, Im2, radial,
              angular);
        if combined_score < best_score_radial
            best_score_radial = combined_score;
            best_alfa = curr_alfa;
            patience_count = 5;
        end
        if MSE_score < best_score_angular
            best_score_angular = combined_score;
            best_beta = curr_beta;
            best_gamma = curr_gamma;
            patience_count = 5;
        end
        curr_alfa = curr_alfa + ((lr_radial)*curr_alfa);
        curr_beta = curr_beta + ((lr_angular)*curr_beta);
        curr_gamma = curr_gamma + ((lr_angular)*curr_gamma);
        iter = iter + 1;
        patience_count = patience_count - 1;
        if patience_count <= 0
            patience = false;
        end
    end
end
```

Appendix B4 – Strain Calculation from AM2D displacements

```
function [rad_strain, ang_strain] = finite_diff_strain(Radial_displacement,
Angular_displacement, max_depth, FoV_Angle, num_a_line)
    %Finite_diff_strain Uses the finite difference between two points in the
    %displacement estimations. Difference is between either rows for radial
    %strain, or columns for angular strain

    rad_strain = zeros(size(Radial_displacement));
    ang_strain = zeros(size(Angular_displacement));

    num_Rows = size(Radial_displacement,1);
    num_Columns = size(Radial_displacement,2);

    dTheta = FoV_Angle/(num_a_line-1);
    dRadius = max_depth/size(Radial_displacement, 1);

    for i = 1:num_Rows - 1
        for j = 1:num_Columns
            %if Radial_displacement(i+1, j) ~= 0
                diff = (Radial_displacement(i, j) - Radial_displacement(i+1, j));
                rad_strain(i, j) = diff;
            %end
        end
    end
    rad_strain = rad_strain * (1/dRadius);

    for i = 1:num_Rows
        for j = 1:num_Columns - 1
            if Angular_displacement(i, j+1) ~= 0
                diff = Angular_displacement(i, j + 1) - Angular_displacement(i, j);
                ang_strain(i, j) = diff;
            end
        end
        dArc = (57 + i) * dTheta;
        ang_strain(i,:) = ang_strain(i,:) * (1/dArc);
    end

end
```

Tristan Curry

Education

University of Waterloo

2017-2022

B.A.Sc. in Mechatronics, Option in Management Sciences

University of Western Ontario 2022-2024

Candidate for M.E.Sc. in Electrical and Computer Engineering – Biomedical Focus

| Relevant Courses

University of Waterloo
MTE-481/482 – Mechatronics Capstone Design
BME-550 - Sports Engineering
BME-588 – Computational Biomechanics
ECE-457B – Fundamentals of Computer Intelligence

University of Western Ontario
BME 9513 – Medical Imaging
BME 9529 – Human and Animal Biomechanics
ECE 9202 – Advanced Image Processing
ECE 9603 – Data Analytics

| Technical skills

1000+ hours working in Java, C++, C#, SOLIDWORKS and MATLAB

~100 hours with Python, VBA programming, JIRA, Git

Professional Experience

TribalScale

Quality Assurance Engineering Co-op · May 2021 - Aug. 2021

- Led software testing initiatives for mobile applications in development.

- Developed and executed test plans for bi-weekly builds.

- Reported on test reports to developers and clients in weekly meetings.

ClearPath Robotics

Project/ Product Management Co-op · May 2019 - Aug. 2019

- Developed project timelines for a development team using Jira management plugins.

- Managed projects involving hardware, software, and test assets.

- Conducted cost analysis of various solutions.

- Presented bi-weekly updates on product progress.

Borrum Energy Solutions

Engineering Associate Co-op · Jan 2018 to April 2018

- Independently designed, prototyped, and tested critical testing apparatuses for wind turbine components using SolidWorks and ANSYS simulations.

- Designed mechanical components for wind turbines.

- Conducted simulations and physical testing on all designed solutions.

The Co-operators

Robotic Process Dev. - Project Lead Co-op · Sep. 2018 - Dec. 2018

- Led a team of 4 in developing a process to automate insurance claim payments using Robotic Process Automation software.

- Reduced manual payment processing time from 2.5 weeks to 1 day through automation.

- Used Microsoft Excel and PowerPoint to create and present bi-weekly release and demo presentations.

Manulife Financial

Backend Dev. Co-op · Jan 2020 to April 2020

- Worked in a self-driven team to upgrade outdated systems to meet new industry standards.

- Successfully upgraded two backend data logging systems for industry compliance using C#.

- Used Jira and Confluence for documentation and task tracking.